Technische Universität München
Fakultät für Chemie

Working Interfaces in Solid-State Electrolytes: A Theoretical Approach towards Realistic Models

Sina Stegmaier

Dissertation

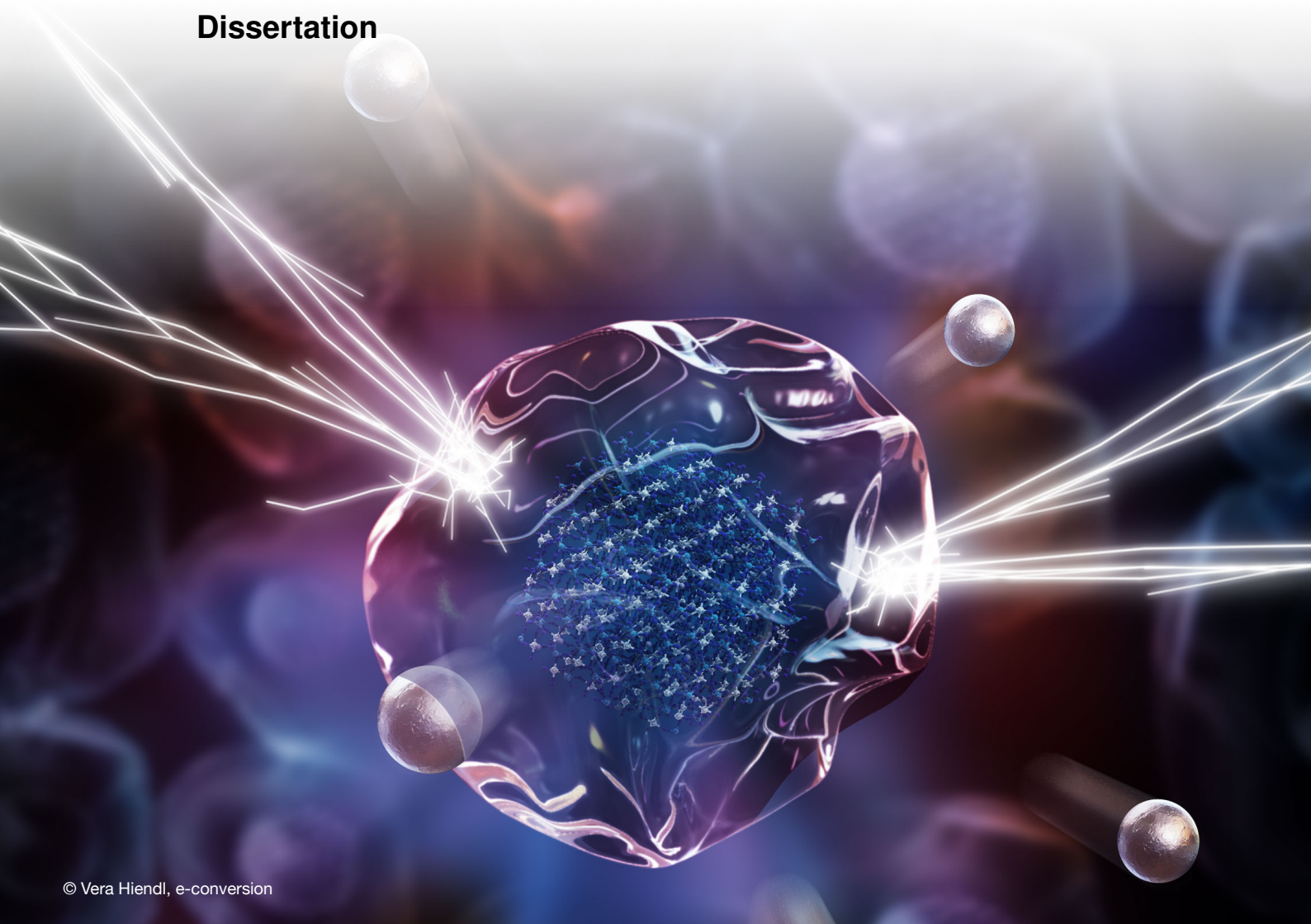

Technische Universität München
Fakultät für Chemie

Working Interfaces in Solid-State Electrolytes: A Theoretical Approach towards Realistic Models

Sina Stegmaier

Vollständiger Abdruck der von der Fakultät für Chemie der Technischen Universität München zur Erlangung des akademischen Grades einer

Doktorin der Naturwissenschaften (Dr. rer. nat.)

genehmigten Dissertation.

Vorsitzender: Prof. Dr. Tom Nilges

Prüfer der Dissertation:

1. Prof. Dr. Karsten Reuter
2. Prof. Dr. Jennifer Rupp

Die Dissertation wurde am 01.07.2022 bei der Technischen Universität München eingereicht und durch die Fakultät für Chemie am 26.07.2022 angenommen.

Für Dominic

Preface

All work presented in this doctoral thesis was performed between February 2019 and July 2022 at the Chair of Theoretical Chemistry of the Technical University of Munich (TUM), under the supervision of Prof. Dr. Karsten Reuter. Parts of this dissertation have been published before in Ref. [1] and Ref. [2]. A research stay hosted by Prof. Dr. Boris Kozinsky of the Materials Intelligence Research Group at the School of Applied Science and Engineering, Harvard University complemented the work performed locally at TUM.

Munich, July 2022 Sina Stegmaier

Abstract

Major obstacles in the realization of next-generation All Solid-State Batteries (ASSBs) are degradation and deterioration processes at solid-solid interfaces in the Solid-State Electrolyte (SSE). Dendrite nucleation and penetration along the mechanically softer grain boundary network results in performance loss and ultimately cell failure. The buried nature of these interfaces and their inherently finite width obstruct experimental characterization and *in operando* analyses. Therefore, a combined theory-experiment approach is crucial to resolve the length and time scales of interfacial processes and gain a deeper mechanistic understanding.

As a promising SSE candidate, the ceramic $Li_{1+x}Al_xTi_{2-x}(PO_4)_3$ (LATP) exhibits a high dendrite suppression capability despite a bulk electronic conductivity which exceeds a postulated critical threshold by orders of magnitude. A novel computational approach yields realistic atomistic structural models of glass-amorphous LATP grain boundaries, based on experimental insights from Transmission Electron Microscopy (TEM) and Atom Probe Tomography (APT). These models reveal a nanometer-sized complexion, effectively protecting the grains by constituting a sizable electronic barrier. A local separation of mobile Li^+ and excess electrons at the nanoscale thus adds to a more nuanced assessment of SSE performance than macroscopic material properties alone.

The established atomistic model of a realistic grain boundary serves as a basis for active interfacial engineering. Encouraged by APT findings, Mg^{2+} is doped locally into the amorphous grain boundary phase. An adopted Monte-Carlo (MC) based protocol suggests a local confinement of Mg^{2+} in the bulk interphase. The resulting minimal dopant bleeding does not significantly compromise adjacent crystalline LATP performance and inherent 3D interconnected pathways for charge carrier migration stay intact. Aliovalent doping allows for the deliberate reduction of Ti^{4+} Transition Metal (TM) centers while increasing the Li ion content. As a result, the residual electronic conduction via polaron hopping is reduced and the local Li^+ conductivity is increased. Local doping with Mg^{2+} therefore presents a promising route towards active engineering of buried solid-solid interfaces from a computational perspective. Due to non-trivial effects upon doping, a confident assignment of target stoichiometries requires experimental input.

Combining insights at different length and time resolutions from theory and experiment is a powerful ansatz to progress in the functional design of high-performing battery materials.

Zusammenfassung

Eine große Hürde auf dem Weg zu Festkörperbatterien (ASSB) der nächsten Generation stellen Degradations- und Alterungsprozesse an Fest-Fest-Grenzflächen im Festkörperelektrolyt (SSE) dar. Die Bildung und Durchdringung von Dendriten entlang des mechanisch weicheren Korngrenzennetzwerks führt zu Leistungsverlust und schließlich zu Zellversagen. Die verborgene Natur dieser Grenzflächen und ihre inhärent geringe Ausdehnung erschweren die experimentelle Charakterisierung und Operando-Analysen. Ein kombinierter Ansatz von Theorie und Experiment ist notwendig, um die Längen- und Zeitskalen von Grenzflächenprozessen aufzulösen und ein tieferes mechanistisches Verständnis zu erlangen.
Als vielversprechender SSE-Kandidat besitzt die Keramik $Li_{1+x}Al_xTi_{2-x}(PO_4)_3$ (LATP) trotz einer elektronischen Volumenleitfähigkeit, die eine postulierte kritische Schwelle um Größenordnungen übersteigt, die Fähigkeit zur Dendritenunterdrückung. Ein neuartiger Simulationsansatz, der auf experimentellen Erkenntnissen aus Transmissionselektronenmikroskopie (TEM) und Atomsondentomographie (APT) basiert, liefert realistische, atomistische Strukturmodelle von glasamorphen LATP-Korngrenzen. Diese Modelle zeigen eine nanometergroße Komplexion, die die Körner effektiv schützt, indem sie eine erhebliche elektronische Barriere darstellt. Eine räumliche Trennung im Nanometerbereich von beweglichem Li^+ und überschüssigen Elektronen führt somit zu einer differenzierteren Bewertung der Elektrolytleistung als die makroskopischen Materialeigenschaften allein.
Das etablierte atomistische Modell einer realistischen Korngrenze dient als Grundlage für aktives Grenzflächen-Engineering. Motiviert durch APT-Befunde wird Mg^{2+} in die amorphe Korngrenzenphase dotiert; ein auf Monte-Carlo basierendes Protokoll bestätigt diesen lokalen Einschluss. Das daraus resultierende minimale Entweichen von dotierten Ionen beeinträchtigt die Leistung von benachbartem, kristallinem LATP nicht signifikant und die inhärenten 3D-Verbindungen für die Ladungsträgerdiffusion bleiben intakt. Die aliovalente Dotierung ermöglicht die gezielte Reduktion von Ti^{4+}-Übergangsmetallzentren bei gleichzeitiger Erhöhung des Li-Ionengehalts. Dadurch wird die elektronische Restleitfähigkeit durch Polaronsprünge verringert und die Li^+-Grenzflächenleitfähigkeit erhöht. Die räumlich begrenzte Dotierung mit Mg^{2+} zeigt daher aus simulativer Sicht einen vielversprechenden Weg zur aktiven Gestaltung verborgener Festkörpergrenzflächen auf. Aufgrund nicht-trivialer Effekte durch Dotierung erfordert die Vorhersage von Zielstöchiometrien experimentellen Input.
Die Kombination von Erkenntnissen aus Theorie und Experiment mit verschiedenen Längen- und Zeitskalen ist ein effektiver Ansatz, um Fortschritte bei der funktionalen Entwicklung von leistungsfähigen Batteriematerialien zu erzielen.

Contents

List of Abbreviations

AFM	Atomic Force Microscopy
ALD	Atomic Layer Deposition
APT	Atom Probe Tomography
ASSB	All Solid-State Battery
CEI	Cathode Electrolyte Interface
COM	Center Of Mass
CSL	Coincidence Site Lattice
CSSE	Composite Solid-State Electrolyte
DC	Direct Current Polarization
DFT	Density Functional Theory
DM-EDFT	Density Mixing Ensemble-DFT
DOE	Design Of Experiment
EDS	Energy Dispersive X-ray Spectroscopy
EIS	Electrochemical Impedance Spectroscopy
FIB	Focused Ion Beam
GA	Genetic Algorithm
HAADF	High-Angle Annular Dark Field
LATP	$Li_{1+x}Al_xTi_{2-x}(PO_4)_3$
LIB	Lithium Ion Battery
LMA	Lithium Metal Anode
MC	Monte-Carlo
MD	Molecular Dynamics
MIEC	Mixed Ionic-Electronic Conducting Interphase
MSD	Mean Square Displacement
NASICON	NA Super Ionic CONductor
NMR	Nuclear Magnetic Resonance
PBC	Periodic Boundary Conditions
PES	Potential Energy Surface
PPPM	Particle-Particle-Particle-Mesh
PSO	Particle Swarm Optimizer
RDF	Radial Distribution Function
RMSD	Root Mean Square Displacement
RT	Room Temperature
SEI	Solid Electrolyte Interface
SEM	Scanning Electron Microscope

SIE	Solid Inorganic Electrolyte	**TEM**	Transmission Electron Microscopy
SPE	Solid Polymer Electrolyte		
SSE	Solid-State Electrolyte	**TM**	Transition Metal

1 Introduction

In light of the ongoing transformation away from fossil energy resources towards sustainable alternatives, storage devices are crucial for on-demand energy utilization. For such intermittent storage, energy conversion processes, i.e. conversion from chemical to electrical form and vice versa, need to be reversible with a high degree of efficiency. Secondary batteries have proven to be an indispensable building block for the storage of renewable energies and due to their portable setup are a key component in the current mobility transition to electrically powered vehicles.

State-of-the-art commercial batteries are typically based on Li-ion chemistry, with Li^+ charge carriers moving through a liquid electrolyte. Especially problematic for these batteries is the highly flammable nature of most organic liquids employed as the electrolyte. A potential next-generation in battery technology are All Solid-State Batteries (ASSBs) featuring only solid state components [3]. Here, the liquid electrolyte and separator in a conventional cell are replaced by a Solid-State Electrolyte (SSE) as shown in Figure 1.1.

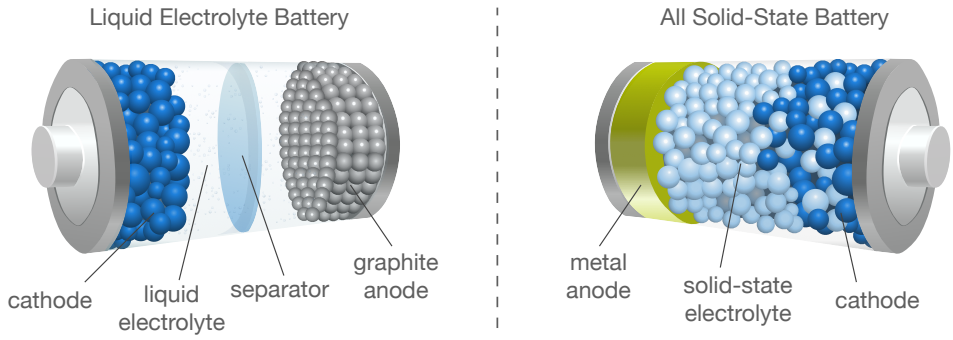

Figure 1.1: Schematic built-up of a conventional battery with liquid electrolyte versus the built-up of an ASSB with solid-state electrolyte. Image adapted and extended from Xu et al. [4].

By exchanging the liquid component with a solid material, these devices not only promise improved operational safety in a wider temperature window, but furthermore exhibit a considerably longer cycling lifetime, as aging and degradation processes occur at larger time scales [5, 6]. Additionally, the utilization of SSEs promises a higher battery performance, as they enable the application of Lithium Metal Anodes (LMAs) [7–9]. Due to its high ca-

pacity and energy density, Li metal is considered the ultimate anode material [10]. Paying into the above promises, ASSBs assert themselves as high-performance materials and are expected to gradually replace todays technology in the upcoming years [11–13].

Though several classes of SSEs with competitive ion conductivities have been developed over the last two decades [14, 15], overall ASSB performance to date often falls short of conventional liquid-electrolyte batteries. Key performance issues can be ascribed mainly to mechano-chemical, chemical, and electrochemical instabilities [16] and interfacial processes, respectively, which severely compromise the cell lifetime [17–21]. Modern engineering routes present a remedy to many SSE material inherent (mechano-)chemical processing issues [22–26]. In contrast, the alignment of (electro-)chemical stabilities in such multi-component devices and the control of interfacial ionic and electronic transport quantities still pose challenges. With solid-solid interfaces being ubiquitous in ASSBs, extensive research effort has been focused on gaining a better understanding and consequently actively engineering these subsystems [27, 28].

Among the most detrimental interfacial processes are contact instabilities arising from redox reactions, as well as metallic dendrite nucleation and growth [29–31]. Nucleation of metallic Li^0 is typically studied at the anode/electrolyte interface. Successive penetration of dendrites into the SSE bulk phase is often facilitated by the mechanical softness of microstructural defects, such as cracks, voids, or grain boundaries [32–34]. These are inevitably introduced during SSE synthesis and cell assembly. Recent studies have shown, however, that dendrites may also nucleate within the bulk SSE itself [35–37]. Possible reasons being a chemical potential overshoot of Li^+ [38, 39] and high residual local electronic conductivity [40]. Controlling buried solid-solid interfaces within the bulk SSE phase is thus essential to suppress dendrite growth via residual electron transport through the grain boundary network.

Compatibility of electrochemically reactive phases in contact is typically based on the respective bulk thermodynamic properties [41, 42]. A lack of sufficiently stable bulk SSE materials, however, has led to cell designs with synthetically introduced surface coatings or the targeted formation of a passivizing phase. Due to the dynamic nature of working interfaces, i.e. structural and chemical transition under synthesis and operating conditions, such protective interphases may also form naturally. Thermodynamically self-limited interphases with a distinct stoichiometry and structure differing from the adjacent bulk phases, so-called complexions [43–46], may serve such a protective purpose in ceramic SSEs.

To overcome the performance limiting interfacial challenges, a deeper understanding of the structural, chemical, and physical characteristics of buried solid-solid interfaces is required. Resolution at an atomistic level is needed to capture the processes occurring at such interfaces with typical finite widths in the nanometer regime [47]. Experimentally, these interfaces are not only difficult to access due to their buried nature, but furthermore analyses at an atomistic resolution require intricate measurements. As a result, experimental studies are mostly conducted on isolated cells from the operational test setting, i.e. post synthesis or *post mortem* [48, 49]. Complementary theoretical investigations are therefore essential to bridge the complexity gap and gain mechanistic insights. The premise for confident

predictions obtained from theory, however, is an accurate representation of the underlying system. To maintain manageable computational cost, higher level theory simulations are limited to rather small length and time scales. Many theoretical studies, especially high throughput material screening [42, 50], have thus focused on bulk phases with short and medium-ranged structural order, which can be mapped into smaller idealized cells [41]. For a satisfactory description of multiphase buried interfaces, which often exhibit a low degree of crystallinity, much larger system sizes are required.

In this thesis, the crucial role of structural and chemical characteristics of grain boundaries in the $Li_{1+x}Al_xTi_{2-x}(PO_4)_3$ (LATP) SSE material are investigated. A multi-phase atomistic model is established, which renders a realistic representation of an extended grain boundary. To arrive at such solid-solid interface structures, a combined theory-experiment approach is pursued bridging the aforementioned complexity gap. Molecular simulations, which are guided by experimental findings, confirm the formation of nanometer-sized complexions encapsulating the LATP grains. The distinct structural and chemical nature of these thin coatings are found to serve as a protective layer to suppress dendrite nucleation, i.e. presenting a sizable barrier for electronic conduction while being permeable for Li ions. These novel insights gained from a nanoscale perspective add to a more nuanced understanding of the ambiguous role of buried solid-solid interfaces in SSEs on overall cell performance.

In a subsequent step, the established atomistic grain boundary model serves as basis for active interfacial engineering. Aliovalent doping of Mg^{2+} in the grain boundary phase allows for the deliberate compositional design to locally reduce Transition Metal (TM) centers and a concomitant increase of the charge carrier concentration. As a result, the protective nature of LATP inherent complexions can further be exploited and interfacial conductivity is improved. While conceptually verifying the benefit of interfacial doping on overall LATP performance, the predictive power of target stoichiometries from theory alone is limited due to non-trivial effects with higher doping concentration. Instead, an adaptive optimization ansatz from both, experiment and theory, is needed to reduce the vast design space and focus on meaningful doping compositions. On a broader note, this work highlights the powerful synergy of a closely interlinked theory-experiment approach to advance in ASSB technology.

The subsequent five chapters are organized as follows:

Chapter 2 provides a comprehensive overview of general SSE material classes with a detailed description of the LATP material used herein. The concepts of various solid-solid interfaces occurring in ASSBs and their effect on cell performance is shown.

Chapter 3 outlines the involved basic theory and respective implementation for the applied computational methods. Analysis tools for structural and dynamic comparison to experimental references are introduced.

Chapter 4 describes a combined theory-experiment approach to identify a nanoscale complexion at the interface between grain and grain boundary in LATP. It is shown that the distinct structural and chemical nature of the complexion serves as a protective thin coating encapsulating the grains.

Chapter 5 builds on the findings of the previous chapter, where the established LATP grain boundary interphase is actively engineered via aliovalent doping. Mg^{2+} is found to be a promising doping candidate exploiting the complexion protective nature and improving local interphase properties.

Chapter 6 summarizes the main results and the conclusions which can be drawn from the findings in this work. An outlook provides potential future perspectives.

2 Solid-State Electrolytes

In this chapter, the established material classes of SSEs are introduced, fundamental differences are highlighted and performance is compared across the vast chemical space. While the material classes are generally covered on a higher-level, the specific LATP SSE material underlying the studies conducted in this work is characterized in greater detail. Due to the solid nature of SSEs, solid-solid interfaces are pervasive in ASSB battery setups. This chapter covers conceptually different solid-solid interfaces occurring in ASSBs and schematically showcases their crucial effect on overall cell performance.

2.1 Material Classes

Owing to the anticipated advantages as compared to conventional liquid electrolytes, scientific and commercial interest in SSEs as high-performance battery materials has re-emerged in recent years [51]. Though today there is a great diversity of different materials realized, basic material design concepts of contemporary SSEs have been established from the late 1960s onward [52, 53].

Two distinct classes of SSEs can be differentiated, namely the Solid Inorganic Electrolytes (SIEs) and the Solid Polymer Electrolytes (SPEs). The contrasting chemical nature of inorganic ceramics in SIEs versus the organic polymers in SPEs leads to challenges specific to each of these two material families. To leverage their advantages and overcome shortcomings of single-phase SSEs, a new design concept has recently been introduced, combining SIE and SPE components to form Composite Solid-State Electrolytes (CSSEs) [54–56]. While these new materials show promising results in terms of performance, their synthesis is driven rather by empiric insights and a satisfying fundamental understanding of nano-scale processes is hitherto missing even for the underlying SIE and SPE components. The focus is thus drawn on single-phase SSEs herein. A schematic decomposition of SSE material classes is shown in Figure 2.1.

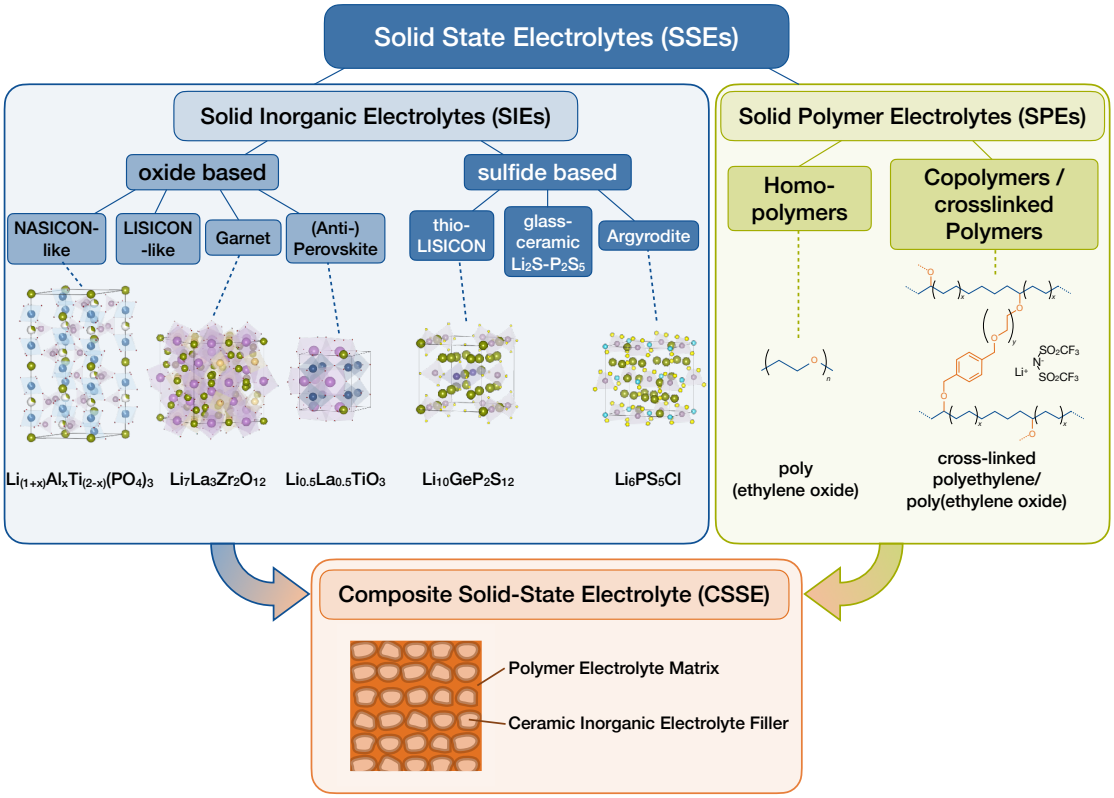

Figure 2.1: Material classes of Solid State Electrolytes: Solid Inorganic Electrolytes (SIEs) with oxide based NASICON-like, LISICON-like, Garnet, (Anti-)Perovskite type electrolytes and sulfide based thio-LISICON, glass-ceramic Li_2S-P_2S_5 and Argyrodites. Exemplary atomistic structures are shown for $Li_{1+x}Al_xTi_{2-x}(PO_4)_3$[(2.1)], $Li_7La_3Zr_2O_{12}$[(2.2)], $Li_{0.5}La_{0.5}TiO_3$[(2.3)], $Li_{10}GeP_2S_{12}$[(2.4)] and Li_6PS_5Cl[(2.5)]. Solid Polymer Electrolytes (SPEs) with homopolymers and copolymers and crosslinked polymers. Exemplary chemical structures are shown for poly(ethylene oxide) (PEO) and crosslinked polyethylene/poly(ethylene oxide).

2.1.1 Solid Inorganic Electrolytes

The SIE material family can further be divided into oxide-based and sulfur-based materials, i.e. the ceramic anionic framework is composed of oxygen anions (O^{2-}) or sulfur anions (S^{2-}), respectively.

(2.1) ICSD 253240
(2.2) mp-942733, DOI:10.17188/1313215
(2.3) mp-557492, DOI:10.17188/1269865
(2.4) mp-696128, DOI:10.17188/1284955
(2.5) mp-985592, DOI:10.17188/1316731

LISICON: Oxide based LIthium Super Ionic CONductors (LISICON) electrolytes and its derivatives are structurally based on the $Li_{14}Zn(GeO_4)_4$ framework. Though this system hosts three mobile Li^+ ions in the $[Li_{11}Zn(GeO_4)_4]^{3-}$ unit cell, the restricted diffusion in two dimensions yields low ionic conductivities of $\approx 10^{-6}$ S cm^{-1} at Room Temperature (RT) [57]. Cationic substitution in $Li_{3+x}Ge_xV_{1-x}O_4$ and $Li_{4-x}Si_{1-x}P_xO_4$ ($0 < x < 1$) based LISICON-like materials leads to improved peak RT conductivities of $\approx 10^{-5}$ S cm^{-1} [58, 59]. Accordingly, partially anionic doping of O^{2-} with Cl^- LISICON-like materials exhibit peak RT conductivities of up to $3.7 \cdot 10^{-5}$ S cm^{-1} [60]. With ionic conductivities below 10^{-4} S cm^{-1} the LISICON-like electrolytes until today fail to meet the performance requirements for most commercial applications [51, 53].

NASICON: Similar to the LISICON, the NA Super Ionic CONductor (NASICON) based on the chemical formula $Na_{1+x}Zr_2Si_xP_{3-x}O_{12}$ ($0 < x < 1$) is an oxide based sodium electrolyte. Li derivatives which maintain the NASICON characteristic phosphate framework of the form $LiM_2(PO_4)_3$ are considered NASICON-like electrolytes. The most prominent candidates are $LiZr_2(PO_4)_3$ (LZP), $LiTi_2(PO_4)_3$ (LTP) and $LiGe_2(PO_4)_3$ (LGP). While showing an improved ionic conductivity of $2.0 \cdot 10^{-6}$ S cm^{-1} for LTP [61], $7.2 \cdot 10^{-5}$ S cm^{-1} for LZP [62] and $3.3 \cdot 10^{-5}$ S cm^{-1} for LGP [61] as compared to the LISICON SSEs, the performance of single metal NASICON-like electrolytes is not competitive. The conductivity can be increased via iso- or aliovalent doping of the metal sites, e.g. aliovalent doping of trivalent M' onto M sites as $LiM_{2-x}M'_x(PO_4)_3$ ($0 < x < 1$). The most common such derivative is doped with Al^{3+}, leading to peak conductivities of $7 \cdot 10^{-4}$ S cm^{-1} for $Li_{1.3}Al_{0.3}Ti_{1.7}(PO_4)_3$ (LATP) and $4 \cdot 10^{-4}$ S cm^{-1} for $Li_{1.5}Al_{0.5}Ge_{1.5}(PO_4)_3$ (LAGP). Especially LATP has drawn attention in recent years and has been employed in commercial devices [63]. Recently Illbeigi et al. have presented a Al^{3+} and Cr^{3+} co-doped NASICON-like electrolyte $Li_{1.5}Al_{0.4}Cr_{0.1}Ge_{1.5}(PO_4)_3$ with an ionic conductivity of $6.65 \cdot 10^{-3}$ S cm^{-1} at room temperature. [64]

(Anti-)Perovskite: Another oxide based SIE subclass is the Perovskite-type SSE with the characteristic Perovskite crystal structure $A^{2+}B^{4+}X_3^{2-}$. The best known Perovskite-type SSE is $Li_{3x}La_{2/3-x}TiO_3$ (LLTO) with a pristine bulk conductivity of $1 \cdot 10^{-3}$ S cm^{-1}. Despite this high bulk conductivity though, the grain boundary conductivity is orders of magnitude lower, leading to a low total ionic conductivity of $2 \cdot 10^{-5}$ S cm^{-1} [65]. The A as well as the B crystal site can be occupied by a range of cations with different oxidation states, e.g. Sr, Hf, Nb, Zr, Ge, Ta etc. While the ionic conductivity can be improved upon cationic substitution, the Perovskite-type SSEs show poor electrochemical stability against lithium metal as well as intercalated electrodes [66]. By inverting the crystalline structure to $A^-B^{2-}X_3^+$ with (A=F^-, Cl^-, Br^-, I^-; B=O^{2-} and X=Li^+) Anti-perovskite type SSEs can be realized. The A site is typically occupied by single halogens or a mixture of halogens, leading to an ionic conductivity of $1.94 \cdot 10^{-3}$ S cm^{-1} for $Li_3OCl_{0.5}Br_{0.5}$ [67].

Garnets: The last oxide based SIE covered in this overview is the Garnet type SSE. Garnets generally follow the structural formula of $A_3B_2(CO_4)_3$ with (A=Ca, Mg, Y, rare earth elements; B=Al, Fe, Ga, Ge, Mn, Ni, V; and C=Al, As, Fe, Ge, Si) [68, 69]. $Li_7La_3Zr_2O_{12}$ (LLZO) is the most commonly known Garnet type SSE with an ionic conductivity of $3 \cdot 10^{-4}$ S cm^{-1} at RT [70]. Besides the promising ionic conductivity, garnet type SSEs are especially appealing

due to their electrochemical stability [66]. A drawback, however, is the reported instability of garnet type SSEs in ambient atmosphere due to moisture and CO_2 [71, 72].

Sulfide based SSEs generally show high ionic conductivities which can be attributed to lower interaction between Li^+ and S^{2-} as compared to O^{2-}.

thio-LISICON: The first subclass of sulfide based inorganic electrolytes is structurally closely related to LISICON and thus also referred to as thio-LISICON. The ceramic thio-LISICON $Li_{10}GeP_2S_{12}$ (LGPS) is the most promising candidate with an extremely high ionic conductivity of $1.2{\cdot}10^{-2}$ S cm^{-1} [73], which is competitive even to organic liquid electrolytes [52]. First principles studies suggest a three dimensional diffusion network to be responsible for the observed conductivity [74].

glass-ceramic Li_2S-P_2S_5: Similarly high conductivities can be obtained by glass and glass-ceramic Li_2S-P_2S_5. Depending on the chosen synthesis route, these materials cover a wide range of conductivities. Former, rather intricate melt-quench protocols are being replaced by mechanical milling and subsequent annealing of the resulting powder. Following this synthesis route, SSEs with formal x Li_2S – (100-x) P_2S_5 (with x=70–80) stoichiometry can be prepared [75]. The hypothesis of Li_2S-P_2S_5 glasses generally showing higher ionic conductivities than crystals due to larger free volume does not hold and it is not straightforward to predict such trends. The reason for this is the complex thio-phosphate chemistry which depends on the underlying synthesis and operating conditions [52].

Generally, while the sulfide based SSEs exhibit great ionic conductivities, they suffer from chemical instabilities and are sensitive towards moisture and oxygen. Especially problematic is the possible generation of H_2S gas upon exposure to air. As a result, the production and manufacturing is restricted to inert environmental conditions and operation is limited requiring appropriate chemical composition and separation from ambient atmosphere.

Argyrodites: Li-ion solid electrolytes based on the Li_6PS_5X structure with (X=Cl, Br, I) are considered Argyrodite type SSEs. This sulfide based subclass exhibits a wide range of ionic conductivities from 10^{-7}–10^{-3} for halogens I^- and Cl^-, respectively. A possible explanation, why the observed iodide conductivity is much lower than the other halogens, is the larger ionic radius which does not allow for the same extent of disorder between halogen and S^{-2} as compared to Cl^- [76]. Analogous to the other sulfide based SSEs, Argyrodites are promising electrolytes from a conductive perspective but show instabilities when exposed to air, which restricts their application.

Another emerging class of SSEs are Li conductors based on halides [77]. Due to low reported ionic conductivities $\approx 10^{-5}$ S cm^{-1} and low oxidation voltages, their development has been delayed. Recent progress in the material design however, has highlighted their potential in terms of possible RT ionic conductivities (10^{-3}–10^{-2} S cm^{-1}), and high (electro-) chemical stability [77].

2.1.2 Solid Polymer Electrolytes

Organic polymer based SSEs usually consist of a polymer serving as the host matrix and dissolved Li salts, e.g. $LiClO_4$, Lithium bis(Tri-Fluoromethane-Sulfonyl)-Imide (LiTFSI), $LiPF_6$, etc. [78]. In light of the transition to commercialize high-performance batteries, SPEs have the advantage of easier synthesis and compatibility with large-scale manufacturing processes as compared to most SIEs [55]. Besides mechanical strength issues and limited thermal stability, the major drawback of SPEs is their low ionic conductivities ranging from 10^{-8} to 10^{-5} S cm^{-1} at RT [79]. The observed low conductivity can be partially attributed to SPE characteristic low dielectric constants of typically $\epsilon < 5$ [52] which impairs ion-pair dissociation required for cationic transport. Polymers with electron-withdrawing groups dispersed along the carbon-carbon backbone, i.e. ionomers, may facilitate such dissociation through specific, non-classical effects such as chelating complexation of oxygen entities [80]. The most studied SPE falling into this category is polyethylene oxide (PEO) coupled with a Li salt. A possible mitigation strategy to improve ionic conductivity in PEO-based SPEs is to plasticize PEO via passive ceramic fillers such as Al_2O_3 or TiO_2 [66]. More complex polymer architectures have been synthesized such as AB and ABA copolymers with different chemistries of the polymer block units, e.g. B=Poly(Styrene-Tri-Fluoromethane-Sulphonyl-Imide of Lithium) P(STFSILi), A=PEO with an ionic conductivity of $1.3 \cdot 10^{-5}$ S cm^{-1} [81] at 60°C, or crosslinked polymers with a porous network, e.g. polyethylene/poly(ethylene oxide) with RT ionic conductivity $>10^{-4}$ S cm^{-1} [82].

Each of the introduced subclasses in both material families of SIEs and SPEs show characteristic advantages and disadvantages. The choice of material class is thus dependent on the ASSB application. However, high-performance ASSBs which are able to compete with organic liquid electrolytes need to exceed an ionic conductivity of 10^{-4} S cm^{-1} [51–53], generally making SIEs the more suitable choice for single-phase SSEs as compared to SPEs. The focus will thus be on inorganic solid electrolytes in the following.

2.1.3 Electrolyte Performance

As high-performance SSEs become increasingly interesting for a multitude of new applications, the material requirements consequentially become more nuanced. Generally though, for a successful ASSB, three key criteria must be met:

1. Sufficiently high ionic conductivity for fast charge carrier transport during charge and discharge of the battery.
2. Minimum residual electronic conductivity to act as an insulator between the electrodes.
3. A wide electrochemical stability window to enable contacting with high-performance electrodes, such as Li metal anodes and high-voltage/high-capacity cathodes.

Approaching market readiness for large volume industries, additional requirements for ASSBs such as processibility, scale-up manufacturing, low cost and material sustainability become more decisive factors [53]. Since the focus here is on a deeper understanding of funda-

mental SSE material inherent phenomena, these economical and ecological performance indicators are not explicitly covered.

Ionic conductivity

The thermodynamic driving forces for ion transport in electrolytes are chemical and electrochemical potential gradients induced during cycling. With negligible concentration gradients at moderate potentials, the conductivity σ is defined as

$$\sigma = F^2 \sum_i c_i \eta_i, \tag{2.1}$$

where F is the Faraday constant, c_i is the mobile ion concentration and η_i is the ion mobility defined by $\eta_i = D_i/RT$ with the diffusion coefficient D_i, the gas constant R and the temperature T [51]. The concentration of mobile ions can be understood as the ability of ion-pair dissociation. As mentioned above, sulfide based electrolytes generally show high ionic conductivity due to weakened Li^+-S^{2-} interactions as compared to oxide based equivalents. Ion mobility is controlled by material specific physical and chemical properties which build up the ion-transport pathways. Structurally, most SIEs are based on a coordinated polyhedron framework with a given periodicity for highly symmetric crystalline materials and amorphous SSEs with no long range order.

In crystalline ionic conductors the mobile ions can hop from one defined lattice site to another, given the hopping energy barrier is sufficiently low [83, 84]. Defects in the crystal sublattice such as interstices, vacancies or higher order lattice distortions play a crucial role in facilitating fast ionic movement [51, 84–89]. For amorphous SIEs such as sulfide based glasses, the conduction mechanism differs from the crystalline materials in that there are no defined sites but the ionic transport is rather free volume driven by the inherent high entropy [84].

Ionic conductivities for the previously introduced SIE subclasses are shown in Figure 2.2. Especially sulfide based thio-LISICON materials such as LGPS and glass-ceramic Li_2S-P_2S_5 show the highest ionic conductivities of up to 10^{-2} S cm^{-1}, competitive even to organic liquid electrolytes. However, the inherent instability in ambient atmosphere limits their applicability. Oxide based NASICON-like electrolytes in contrast exhibit chemical stability not only in air but also in water [104]. With sufficiently high ionic conductivities up to 10^{-4}–10^{-3} S cm^{-1} at room temperature, they present a promising material class for ASSB applications.

While both, anti-perovskite and garnet type electrolytes display similar conductivities in the mS cm^{-1} regime, they are chemically reactive with moisture in the air and require operation in an inert atmosphere [52]. Perovskite type electrolytes are promising in terms of chemical stability and show good ionic conductivity for pristine bulk materials. Orders of magnitude lower grain boundary conductivities, however, lead to total RT conductivities of 10^{-5} S cm^{-1} which are not competitive to other SIEs. Owing to the underlying chemistry of Argyrodites, this material class suffers from similar chemical instabilities in ambient atmosphere as thio-LISICON and other sulfide based electrolytes. Despite these operational challenges, Argyrodites show conductivities of 10^{-7}–10^{-3} S cm^{-1} depending on the ionic radius of the halide.

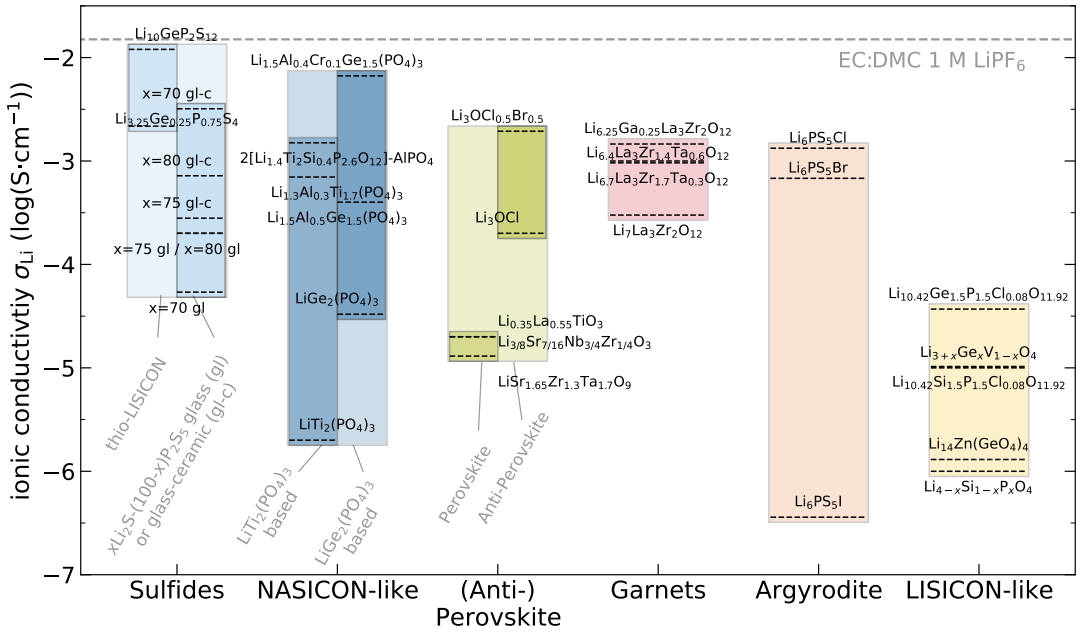

Figure 2.2: SIE ionic conductivities at room temperature. Sulfides: $Li_{3.25}Ge_{0.25}P_{0.75}S_4$ [90], $Li_{10}GeP_2S_{12}$ [73] (LGPS), x Li_2S-(100-x)P_2S_5 (with x=70 [91], 75 [92, 93], 80 [75, 93]). NASICON-like: $LiTi_2(PO_4)_3$ [61] (LTP), $LiGe_2(PO_4)_3$ [61] (LGP), $Li_{1.5}Al_{0.5}Ge_{1.5}(PO_4)_3$ [94] (LAGP), $Li_{1.3}Al_{0.3}Ti_{1.7}(PO_4)_3$ [61] (LATP), 2[$Li_{1.4}Ti_2Si_{0.4}P_{2.6}O_{12}$]-$AlPO_4$ [94], $Li_{1.5}Al_{0.4}Cr_{0.1}Ge_{1.5}(PO_4)_3$ [64]. (Anti-)Perovskite: $LiSr_{1.65}Zr_{1.3}Ta_{1.7}O_9$ [95], $Li_{3/8}Sr_{7/16}Nb_{3/4}Zr_{1/4}O_3$ [96], $Li_{0.35}La_{0.55}TiO_3$ [65] (LLTO), Li_3OCl [97], $Li_3OCl_{0.5}Br_{0.5}$ [67]. Garnets: $Li_7La_3Zr_2O_{12}$ [70] (LLZO), $Li_{6.7}La_3Zr_{1.7}Ta_{0.3}O_{12}$ [98], $Li_{6.4}La_3Zr_{1.4}Ta_{0.6}O_{12}$ [99], $Li_{6.25}Ga_{0.25}La_3Zr_2O_{12}$ [100]. Argyrodite: Li_6PS_5I [101], Li_6PS_5Br [102], Li_6PS_5Cl [103]. LISICON-like: $Li_{4-x}Si_{1-x}P_xO_4$ [58], $Li_{14}Zn(GeO_4)_4$ [57], $Li_{10.42}Si_{1.5}P_{1.5}Cl_{0.08}O_{11.92}$ [60], $Li_{3+x}Ge_xV_{1-x}O_4$ [59], $Li_{10.42}Ge_{1.5}P_{1.5}Cl_{0.08}O_{11.92}$ [60].

LISICON type electrolytes show the lowest ionic conductivities in the SIE material class and are currently not competitive with other subclasses.

Electrochemical stability against metallic Lithium

In order to ensure thermodynamic stability when operating an ASSB, the electrochemical potential of both electrodes needs to lie within the electrochemical stability window of the electrolyte, i.e. the voltage gap between its oxidation and reduction potential [41, 105]. Generally, a wide electrochemical stability window is preferred to facilitate the use of both, high performing cathodes and anodes.

Electrochemical stability windows against Li/Li^+ of the most prominent candidates in each SIE subclass are shown in Figure 2.3. First-principles based calculations are adopted from Schwietert et al. [106] and compared to respective experimentally measured electrochem-

ical stabilities [65, 90, 103, 107–109]. It has recently been shown that electrochemical stability windows obtained from computational simulations yield more narrow windows than observed in experiment [108]. For the experimental measurements, a clear distinction of actual bulk thermodynamic properties is difficult to obtain and reported values may be masked by other regimes.

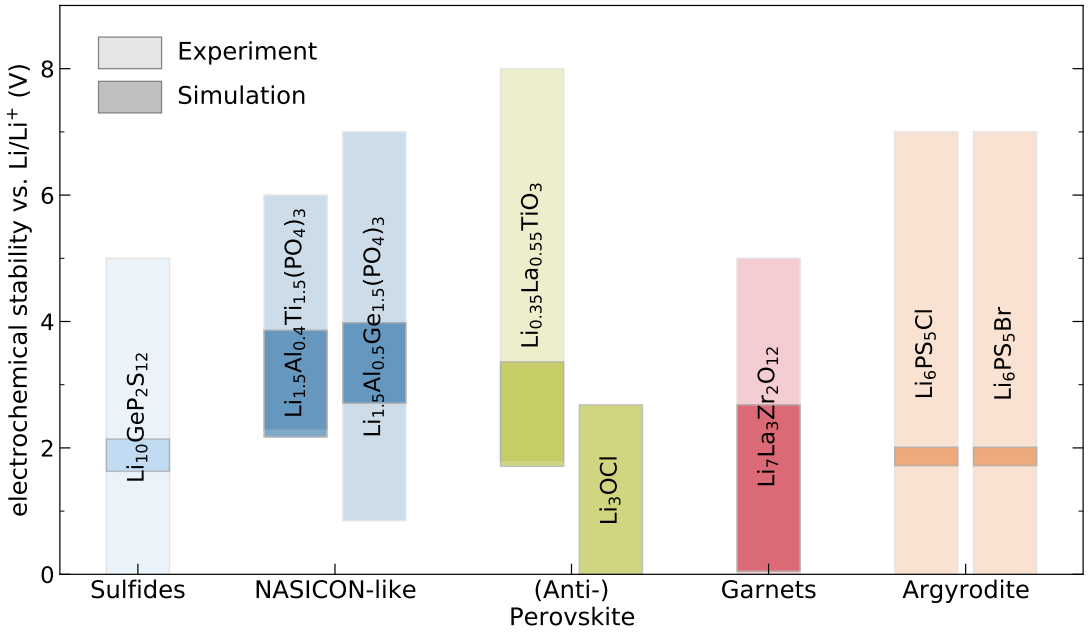

Figure 2.3: SIE electrochemical stability window vs. Li/Li^+. Stabilities predicted from first-principles calculations (darker bars) are adopted from Schwietert et al. [106]. Experimental values (lighter bars) are adopted for LGPS [90], LAGP [107], LATP [108], LLZO [65], LLTO [109] and Li_6PS_5X with X=Cl, Br [103].

Figure 2.3 corroborates that many subclasses of SIEs show electrochemical stability against Li/Li^+ with a wide voltage window. While both NASICON-like electrolytes LATP and LAGP, and perovskite LLTO are not stable against a LMA, their oxidation potential enables the use of high-performing cathode materials. To further expand the electrochemical stability windows and bridge potential gaps, electrolyte-electrode interfaces are actively engineered, e.g. via the introduction of interfacial layers [51]. In general, SIEs outperform commercial organic liquid electrolytes in terms of electrochemical stability windows, enabling higher energy density ASSBs.

2.2 $Li_{1+x}Al_xTi_{2-x}(PO_4)_3$ NASICON Electrolyte

NASICON-type electrolytes with high ionic conductivities and wide electrochemical stability windows have recently experienced renewed interest due to their chemical stability in air/water atmosphere and low toxicity and manufacturing cost [110, 111]. The most promis-

ing candidates are $Li_{1+x}Al_xTi_{2-x}(PO_4)_3$ (LATP) and $Li_{1+x}Al_xGe_{2-x}(PO_4)_3$ (LAGP). Replacing the highly reducible Ti^{4+} in LATP with less reactive Ge^{4+} in LAGP widens the electrochemical stability window, cf. Figure 2.3, thus improving the interfacial stability toward LMA. However, the higher cost of germanium compounds with a factor of 350 for GeO as compared to TiO_2 [110], renders LAGP uneconomical for commercial applications. Additionally, the low abundance of germanium (0.00016 % in the Earth's crust [112]) as compared to titanium (0.41 % in the Earth's crust [113]) identifies LAGP to be unsustainable and therefore nullifies its utilization in large-scale volumes. Therefore, further emphasis is directed toward LATP as a SSE material for next generation ASSB usage.

2.2.1 Crystal Structure and Li^+ Conductivity

The underlying $LiTi_2(PO_4)_3$ crystal structure of LATP is composed of TiO_2 octahedra and PO_4 tetrahedra, which share an oxygen corner to form a three dimensional skeletal framework, see Figure 2.4 (a), and constitute a rhombohedral unit cell of space group $R\bar{3}c$ [114]. The interconnected anionic polyhedra framework constitutes voids for Li ions and structurally determines the charge carrier transport pathways. Crystallographically, three Li sites are differentiated in $LiTi_2(PO_4)_3$, the $M1$ site (6b, six-fold oxygen coordination), the $M2$ site (18e, ten-fold oxygen coordination) and the $M3$ site (36f, four-fold oxygen coordination) [115, 116]. The Li sites are arranged in an alternating fashion along conducting channels and the $M1$ site is expected to be fully occupied [117] while the $M2$ and $M3$ occupation depends on the amount of excess Li^+ introduced from doping with Al^{3+}. The exact ion migration pathway of Li^+ through Al^{3+} doped LATP has been studied both by means of computational analysis [118] and experimental Nuclear Magnetic Resonance (NMR) spectroscopy [119]. Fourier map differences combined with neutron diffraction [120], suggest an increased occupation of $M3$ sites with Al^{3+} doping and a consequent $M1$-$M3$-$M3$-$M1$ three dimensional zig-zag diffusion pattern [120]. Molecular Dynamics (MD) simulations employed in this work, corroborate these findings by Monchak et al. [120], suggesting this zig-zag pattern to be the primary diffusion pathway for Li^+ ions, cf. Figure 2.4 (b).

Aono et al. have first reported an increase in ionic conductivity when doping the rather poor LTP ionic conductor with Al^{3+} onto formal Ti^{4+} sites [61, 121, 122]. Since then the mechanism behind this conductivity enhancement and respective efforts to maximize this effect have been studied extensively [123–125]. The observed improvement of Li conductivity can be attributed to:

1. The number of charge carriers Li^+ is increased to maintain net charge neutrality when substituting the tetravalent Ti^{4+} for the trivalent Al^{3+}. The additional Li^+ is prone to occupy not only the $M1$ site but preferentially also the $M3$ site in LATP [126]. This reduces electrostatic repulsion between $M1$ and $M3$ ions and increases vacancy concentration on the $M1$ position, contributing to the observed enhanced conductivity.

2. A smaller ionic radius of Al^{3+} cations as compared to Ti^{4+} results in a densification of the material. From the crystal structure of LATP, cf. Figure 2.4 (a), it is evident that the effect on lattice parameters is anisotropic and especially the c-axis is compressed.

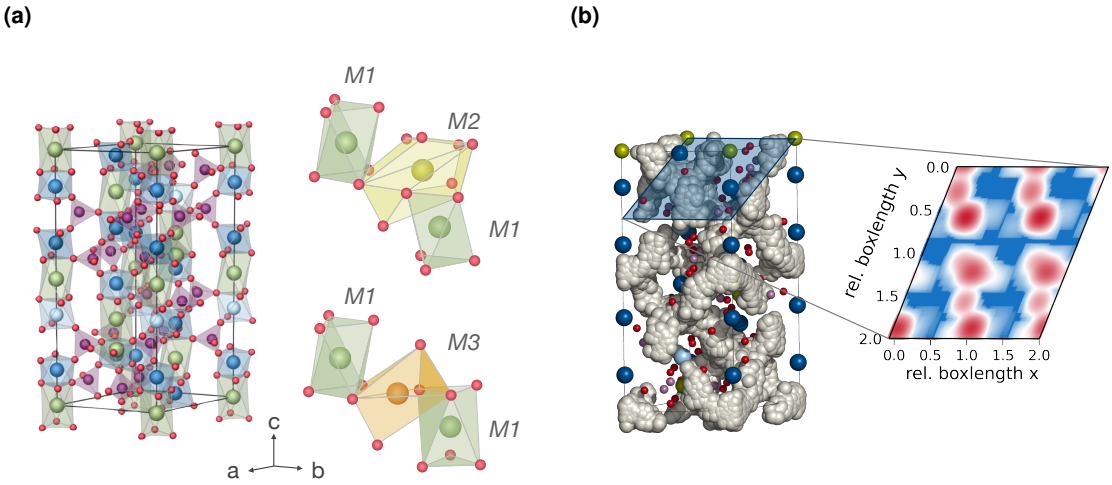

Figure 2.4: LATP Solid State Electrolyte: **(a)** Crystal Structure of $Li_{1+x}Al_xTi_{2-x}(PO_4)_3$ and corresponding Li sites. Elemental colors are chosen according to Li $(M1)$ ●, Li $(M2)$ ●, Li $(M3)$ ●, Al ●, Ti ●, O ● and P ●. **(b)** Diffusion pathway obtained from Li density mapping and 2D projection of Molecular Dynamics Simulation of LATP for 2 ns at 700 K.

The a-axis is only indirectly affected through the gradual shrinkage of AlO_6 along the c-axis [110]. While densification of the material promotes Li diffusion since the interstitial voids become more accessible, there is an optimum amount of doping before the Li channels become too narrow for effective ion transport.

3. Grain boundary interfacial resistance of adjacent LATP grains is efficiently reduced by the Al^{3+} induced structural changes and aforementioned densification [120, 122].

Conductivity changes in $Li_{1+x}Al_xTi_{2-x}(PO_4)_3$ depend on the amount of aluminum incorporated. Rettenwander et al. have systematically screened different contents of $x_{Al^{3+}}$ and the reported ionic conductivities are illustrated in Figure 2.5 (a) [127].

Stoichiometrically the aluminum content can be varied between $0 \leq x_{Al^{3+}} \leq 1$ resulting in full occupation of possible Li sites. Starting around $x_{Al^{3+}}$=0.4–0.5, however, Al^{3+} is reaching its solubility limit in LTP, indicated by the shaded area in Figure 2.5 (a), and the formation of secondary phases such as $AlPO_4$ becomes predominant [125, 139]. An optimum aluminum concentration in LATP is estimated around $x_{Al^{3+}}$=0.3–0.4 [61, 140, 141] with bulk ionic conductivities of up to $5 \cdot 10^{-3}$ S cm^{-1} [127] which is about three orders of magnitude higher than observed in pristine LTP. These stoichiometric changes substantiate the sensitivity of the conductivity enhancement upon Al^{3+} insertion. A balancing of Li charge carrier concentration, material densification and sufficient residual vacancy concentration is needed for an optimum LATP SSE design.

Similar to the chemical composition in stoichiometric LATP, the chosen synthetic route may have a crucial impact on conductivity. A comprehensive overview of possible synthesis

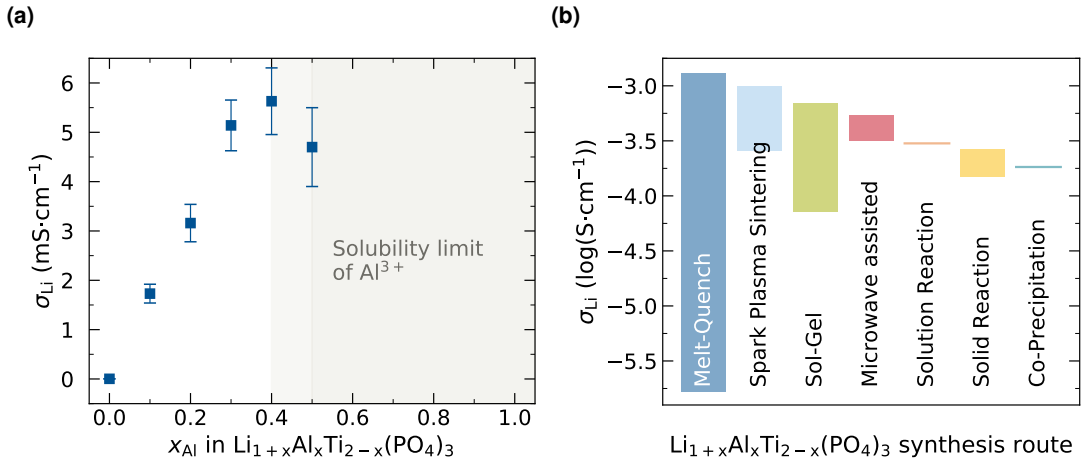

Figure 2.5: Effects on LATP conductivity: **(a)** Effect of chemical composition, i.e. incorporated Al^{3+} content $x_{Al^{3+}}$ on Li ionic conductivity at room temperature. Values are adopted from Rettenwander et al. [127]. **(b)** Effect of LATP synthesis method on Li ionic conductivity at room temperature for melt-quench synthesis [94], spark plasma sintering [123, 128], sol-gel synthesis [96, 129–132], microwave assisted sintering [133, 134], solution reaction [135], solid reaction [136, 137] and co-precipitation [138].

methods for LATP is provided by DeWees et al. [111]. Generally, due to its chemical stability, LATP can be synthesized via solid-based or liquid-based approaches. Solid-based approaches include solid-state synthesis [136, 137], melt-quench methods [94] and fast sintering such as spark plasma sintering [123, 128] or microwave assisted sintering [133, 134]. Liquid-based approaches mainly refer to sol-gel synthesis [96, 129–132], solution-reaction [135] or co-precipitation [138]. The reported room temperature Li ion conductivities for the different synthesis methods are shown in Figure 2.5 (b). Chemically the LATP material is particularly impacted by the choice of precursors, while physically the sintering parameters such as temperature and heating time significantly affect ion conductivity [111].

2.2.2 Application and Modifications

When employing an SSE in a battery setup, i.e. contacting it with high-performing electrodes, interfacial reactions and instabilities often leads to significant performance loss or even complete battery failure. Here, a brief summary of selected advances reported in literature on LATP specific modifications is given.

The application of pristine LATP in an ASSB setup faces the major challenge of electrochemical instability against Li metal, cf. Figure 2.3. Single-phase LATP electrolytes have thus been modified by introducing chemically more inert buffer layers such as PEO [142], Lithium Phosphorus Oxy-Nitride (LiPON) [143] or Li_3PO_4 [144]. Furthermore, surface coating has proven efficient to stabilize the interface via e.g. coating with Al_2O_3 via atomic layer deposition [145] or coating the ceramic LATP electrolyte with a protective polyphosphazene/PVDF-

HFP/LiBOB setup [146]. Compared to pristine LATP, the surface modified Li/Al_2O_3-coated LATP/Li symmetric cell setups exhibit promising performance [111]. Even LATP surface modifications via radio frequency sputtering with electrochemically more stable NASICON-like amorphous LAGP have shown superior performance [147].

LATP solid state electrolyte is a promising material candidate for future ASSB applications and has proven to be eligible for more complex composite battery architectures. In order to further improve its performance, a better material understanding of interfacial processes is needed since targeted interfacial engineering is becoming increasingly accessible.

2.3 Working Solid-Solid Interfaces

Due to the solid nature of all components employed in ASSBs, i.e. both electrodes and electrolyte, solid-solid interfaces are pervasive. While in the past research focus has been dedicated to optimizing bulk material properties, the focus has been shifted towards tackling interfacial challenges in recent years [27, 28, 148]. Solid-solid interfaces play a crucial role in overall cell behavior and are often the root for performance loss and/or complete cell failure especially when realizing metal anodes with SSEs. It is thus imperative to better understand the mechanisms on how these interfaces are formed and how they impact battery performance.

2.3.1 Challenges and Interface Instabilities

The underlying principles responsible for the manifold of challenges attributed to solid-solid interfaces can be clustered into 1) mechanical instabilities and 2) (electro-)chemical instabilities. A schematic overview of possible failure modes due to interfacial processes is ASSBs is shown in Figure 2.6.

Mechanical Instabilities

In contrast to liquid electrolytes, the assembling of two solid compounds, i.e. electrolyte and electrode, often suffers from poor interfacial contacting and the formation of microstructural defects such as surface voids [149], cf. Figure 2.6. SIE materials exhibit an inherent high shear modulus, making them brittle and prone to crack formation. This is problematic when operating electrodes with high volume changes. The low flexibility of SIEs cannot compensate for the increasing volume demands of electrodes and cracks may form in the SSE [26]. Generally, poor contacting through voids and cracks not only impairs Li ion conductivity but further presents an accessible route for Li dendrite growth [32]. Originally, according to the theoretical model of Monroe and Newman [150], a high shear modulus of crystalline materials was suggested to decelerate Li reduction kinetics thus stabilizing the SSE against dendrite formation. However, recent studies on structurally different amorphous, polycrystalline, and single-crystal SSEs have shown that Li penetration does not depend on the shear modulus [151]. A more detailed overview and resulting mechanical design rules for SIE applications can be found in [26, 152].

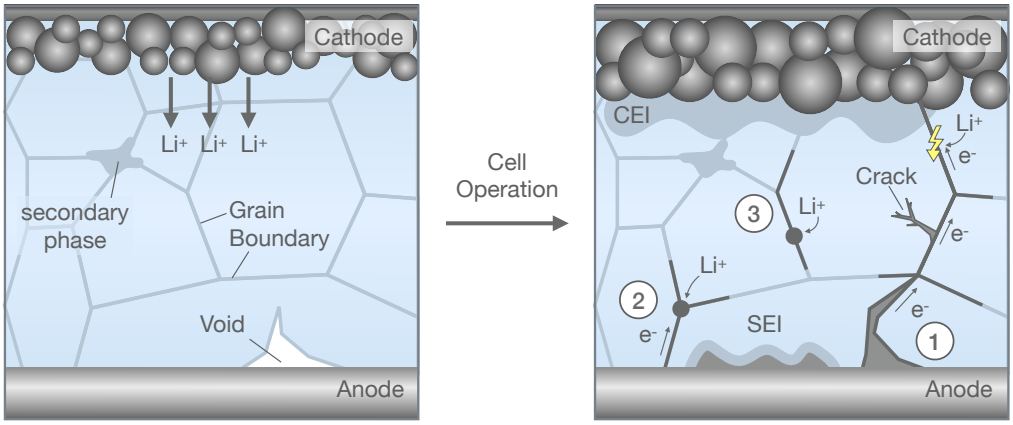

Figure 2.6: Interfacial processes in SSEs leading to cell degradation and possibly cell failure. Left: Microstructural defects introduced during synthesis and cell assembly: voids leading to poor anode-SSE contacting, grain boundary formation, pores and secondary phases within SSE material. Right: Failure modes induced by interfacial processes: electrolyte-electrode interphase formation (Solid Electrolyte Interface (SEI) at anode and Cathode Electrolyte Interphase (CEI) at cathode), volume expansion of cathode, short-circuit risk of dendrites reaching cathode, dendrite penetration into SSE grains through cracks and dendrite nucleation: ① from anode contact defects, ② from residual electronic conductivity of SSE, ③ from high chemical overpotential in grain boundaries. Figure adapted and extended from Zhao et al. [51].

(Electro-)Chemical Instabilities

Continuous interfacial chemical reactions between electrolyte and electrode can lead to the build up of extensive interphase layers. These phases are referred to as Solid Electrolyte Interface (SEI) at the anode interface and Cathode Electrolyte Interface (CEI) at the cathode side, respectively, cf. Figure 2.6. Decomposition products at the anode interface may have a detrimental effect, when forming a Mixed Ionic-Electronic Conducting Interphase (MIEC) [153]. These interphases exhibit constant thickening and lead to increased interfacial resistance, large polarization and eventually to cell failure [27]. Oxide based SIEs which contain easily reducible cations such as Ti^{4+}, P^{5+}, Nb^{5+} etc., can form alloy phases (20 µm thickness), as well as lower valent transition metal species [154]. CEI phases at the cathode/SSE interface form due to interdiffusion of the materials in contact [27, 155]. For cathode and SIE compounds which exhibit a Li^+ chemical potential mismatch, i.e. there is a driving force for local Li^+ accumulation or depletion, so called space charge layers have been reported to form [156–158]. The induced polarization leads to increased interfacial resistance for Li^+ ion migration and consequentially to capacity fading [158].

In order to employ a lithium metal anode, which is considered to be the ultimate anode material due to its high capacity and energy density [7, 8], the anode/SSE interface must be

electrochemically stable. If the cathodic limit of the SIE is lower than the electrochemical potential of the anode, this mismatch in electrochemical stability window facilitates the reduction of Li^+ to metallic Li^0 and may lead to dendrite nucleation. A potential match between the ASSB components in contact is shown in Figure 2.7. Complete propagation through the SSE, i.e. connecting anode and cathode through electronically conducting Li^0 metallic dendrites, leads to a short-circuit and premature battery failure. The SSE plays a crucial role in suppressing dendrite nucleation and proliferation to avoid such fatal cell deterioration.

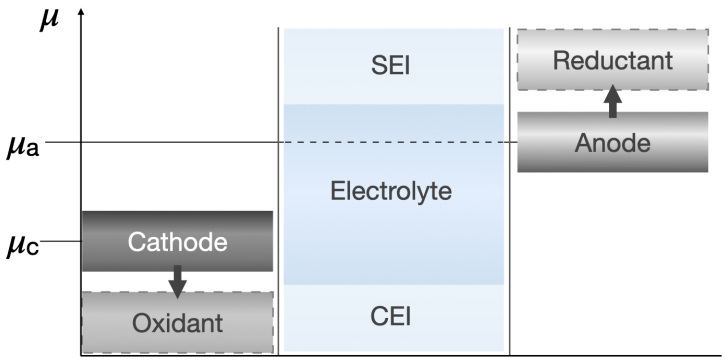

Figure 2.7: Relation between potentials of ASSB components. If the cathode and anode potentials μ_c and μ_a, respectively, do not lie within the SSE window, kinetic stabilization by the formation of an interphase layer is required. Figure adopted from Goodenough et al. [159].

As indicated in Figure 2.6, there are different scenarios facilitating dendrite nucleation and growth. The first of which is dendrite growth induced by discontinuous interfacial contacting, i.e. voids and holes at the interface [29, 160], but also pores within the SSE [161]. Even a single-crystal SE prepared by Chiang et al. exhibited dendrite propagation caused by crack formation [151]. A second mechanism of dendrite nucleation in the SSE phase can be attributed to residual high local electronic conductivity [40]. While the dendrites may grow in proximity to the anode as the electron donor, electrochemical reduction of Li^+ is also reported in the SSE bulk with electrons removed from e.g. O^{2-} of the anionic framework, impurities, dopants and other sources of residual electrons [35–37]. Recently, a third dendrite nucleation process was introduced which is driven by local chemical potentials μ_{Li} above the standard chemical potential of Li metal μ^0_{Li} [38, 39]. The observed kinetically forced potential "overshoot" at SSE grain boundaries is suggested to be induced by ionic diffusion bottlenecks or local gradients in Li transference number [38].

2.3.2 Grain Boundaries and Complexions in Solid Electrolytes

Grain boundaries in SSEs, i.e. solid-solid interfaces between adjacent grains, typically form during synthesis and subsequent thermal treatment of the electrolyte [111]. Ceramic SSE powders are comprised of numerous, loosely arranged individual grains before compres-

sion and sintering. The formed grain boundaries are interconnected and organized in a network extending through the electrolyte cell compound. Though orders of magnitude smaller than typical grain sizes in the µm regime [47], grain boundary widths can span over several nano-meters and thus often constitute extended interphases rather than sharp atomic interfaces [47, 162, 163]. The distinct chemical composition and structural properties of grain boundaries do not necessarily resemble the underlying SSE bulk material and can differ significantly [164, 165]. Such interphases have recently been termed complexions [43–46] if they 1) are thermodynamically self-limiting in thickness, 2) exhibit structures which are neither fully amorphous nor completely crystalline, 3) show structural and/or chemical composition gradients, and distinctively differ from neighboring 4) compositional and 5) thermodynamical bulk characteristics [44].

Grain boundaries, like all interfaces, play a crucial role in the electrolyte performance. They are often considered to be a bottleneck for Li^+ ion diffusion [47, 166] and present an accessible route for Li dendrite nucleation [38, 39] and penetration [32–34]. Recent studies have shown however, that grain boundary modifications and targeted design may in fact stabilize SSE performance by e.g. better interfacial contacting through grain boundary densification [167, 168]. Findings obtained from studies conducted in this work further point toward complexions, which have been shown to occasionally form between ceramic grains in LATP [1], to have a stabilizing effect on the LATP electrolyte.

The exact functionality of grain boundaries in SSEs remains ambiguous even though their impact on SSE performance is indisputable. It is thus essential to gain a deeper atomistic-level understanding to fully utilize their potential.

2.3.3 Atomistic Modeling of Solid-Solid Interfaces

Characterization of solid-solid interfaces proves difficult experimentally since they are comparably small in size and often these interfaces are buried and thus hardly accessible. Further complications arise due to the evolution of solid-solid interfaces during cycling. Changing operating parameters, such as applied potentials and temperature, as well as non-reversible chemical interface reactions, influence the form and extent of such "working" interfaces. Post-synthesis and post-mortem analyses, i.e. *ex situ* studies where the cell is removed from the testing environment after cycling, either fail to capture or interrupt the material evolution especially at interfaces [49]. In recent years, more intricate experimental setups have allowed for *in situ* or even *in operando* material characterizations [48, 49]. Since experimental approaches are hitting their time and length-scale resolution limits, insights gained from computational studies of atomistic interface models are imperative.

The atomistic modeling of solid-solid interfaces can be classified into 1) sharp interfaces between two crystalline grains and 2) diffuse interphases between either structurally different slabs and/or chemically different phases. Schematic representations falling into these categories are shown in Figure 2.8. For atoms in the interfacial region to relax into local basins of the potential energy surface, the construction of atomistic solid-solid interfaces is typically followed by structural relaxation at elevated temperatures [166, 169, 170].

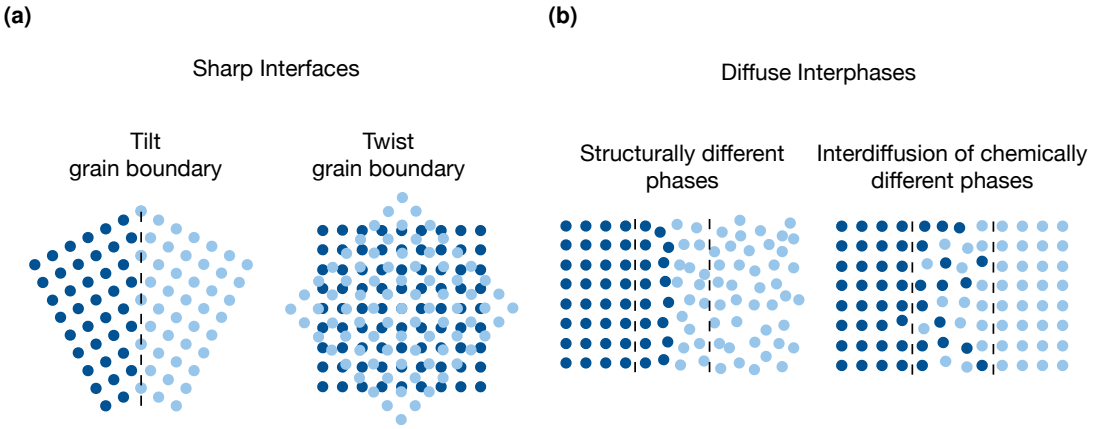

Figure 2.8: Schematic of atomistic modeling approaches for solid-solid interfaces: **(a)** Sharp interfaces obtained from coincidence site lattice (CSL) theory, where the rotation axis is parallel to the boundary plane for tilt grain boundaries (left) or perpendicular to the boundary plane for twist grain boundaries (right). **(b)** Diffuse Interphases of structurally different phases (left) and interdiffusion of chemically different phases (right).

The depicted "sharp interfaces" are typically constructed using the Coincidence Site Lattice (CSL) theory [171]. Here, crystal slabs with a defined lattice are deliberately misoriented by a rotation axis which is either parallel, i.e. tilt grain boundaries, or perpendicular, i.e. twist grain boundaries, to the boundary plane. Most computational studies on solid-solid interfaces in solid electrolyte materials employ this ansatz [166, 169, 172] leading to interfaces with only several Å widths.

Grain boundaries which are set up following the CSL theory, require high symmetry of the two underlying crystal lattices and with their small widths represent rather idealized interfaces. Recent studies have introduced the generation of more realistic, extended atomistic interphases [170, 173]. Kim et al. have fused two slabs of structurally different, i.e. ceramic and amorphous, phases of $(Li_2S)_{0.75}(P_2S_5)_{0.25}$ to study Li^+ diffusion in a glass-ceramic model [170]. A solid-solid interphase representing interdiffusion of chemically different lanthanum strontium manganite (LSM) anode and yttria-stabilized zirconia (YSZ) electrolyte via a Monte-Carlo approach has recently been proposed by Türk et al. [173]. Building on these advancements, a novel approach driven by experimental findings toward atomistic modeling of realistic multi-phase grain boundaries is presented in Section 4.4.

3 Computational Methods

The construction of extended atomistic grain boundary models and subsequent Li-ion dynamics studies are conducted using MD Simulations based on classical force field potentials. Though many classical force fields have been gradually replaced by so-called Machine-Learned potentials in recent years [174, 175], an accurate description of complex ternary systems, such as LATP, exceeds current capabilities of these data driven approaches. In order to parameterize classical potentials, first-principles electronic structure calculations at the Density Functional Theory (DFT) level are utilized as reference. To bridge the gap between nano-second time scales of MD simulations to experimental observables, atomistic motion is extrapolated to macroscopic ion diffusion behavior. Similarly, structural comparison of atomistically resolved models can be achieved by Transmission Electron Microscopy (TEM) Image simulation. The respective underlying theoretical concepts are presented in this chapter.

3.1 Density Functional Theory

Due to an often advantageous balance of accuracy versus computational efficiency, DFT has become an established electronic structure method in materials research. The main selling point of DFT is the description of a many-electron system using the spatially dependent electron density as the central property. By following this approach, the complexity is reduced significantly as compared to e.g. wavefunction based methods. In this section a brief outline of the DFT method is given. A more profound derivation is provided in Ref. [176].

3.1.1 Hohenberg-Kohn Theorems

Within the adiabatic Born-Oppenheimer approximation heavy nuclei are treated as static due to their orders of magnitude higher inertia of motion as compared to electrons. Interaction of electrons in an effective external potential induced by the nuclei can thereby be represented by a mapping of the ground state electronic density $\rho(\mathbf{r})$ onto this external potential. Based on this principle, Hohenberg and Kohn have formulated their first theorem, stating that the external potential is uniquely described by the electronic density $\rho_0(\mathbf{r})$ of the system ground state E_0 [177]. Variation of the electron density of a given system by default results in states

with higher energy than the ground state, which describes the second Hohenberg-Kohn theorem [177]

$$E_0 = E\left[\rho_0(\mathbf{r})\right] < E\left[\rho(\mathbf{r})\right]. \tag{3.1}$$

The energy functional is comprised of interaction contributions according to

$$E\left[\rho(\mathbf{r})\right] = \underbrace{V_\mathrm{e}\left[\rho(\mathbf{r})\right] + V_\mathrm{ee}\left[\rho(\mathbf{r})\right] + V_\mathrm{ne}\left[\rho(\mathbf{r})\right]}_{\text{known}} + \underbrace{V_\mathrm{xc}\left[\rho(\mathbf{r})\right]}_{\text{unknown}}, \tag{3.2}$$

where the *known* parts are the non-interacting electron kinetic energy $T_\mathrm{e}\left[\rho(\mathbf{r})\right]$, the classical electron-electron interaction $V_\mathrm{ee}\left[\rho(\mathbf{r})\right]$, and the electron-nuclei interaction $V_\mathrm{ne}\left[\rho(\mathbf{r})\right]$. There is however an *unknown* part, the exchange-correlation (xc) functional $V_\mathrm{ex}\left[\rho(\mathbf{r})\right]$. Concepts to approximate the exchange-correlation functional are illustrated in Section 3.1.3.

3.1.2 Kohn-Sham Approach

An established approach to describe the electron density is based on the idea of a non-interactive reference system for which the exact solution of the Schrödinger Equation can be calculated. Kohn and Sham demonstrated the mapping of a real system onto such an ideal reference system, where summing over the non-interacting single particle states Φ_i^KS corresponds to the electron density of the real interacting system via

$$\rho(\mathbf{r}) = \sum_i |\Phi_i^\mathrm{KS}(\mathbf{r})|^2. \tag{3.3}$$

Minimizing the energy functional in Equation (3.2) with respect to the Kohn-Sham states Φ_i^KS, yields the actual Kohn-Sham equations

$$\left[-\frac{\hbar^2}{2m_e}\nabla_{r_i}^2 + \hat{V}_\mathrm{eff}(\mathbf{r})\right]\Phi_i^\mathrm{KS}(\mathbf{r}) = \epsilon_i^\mathrm{KS}\Phi_i^\mathrm{KS}(\mathbf{r}), \tag{3.4}$$

where $-\frac{\hbar^2}{2m_e}\nabla_{r_i}^2$ operates on the kinetic energy of the non-interacting reference electrons. $\hat{V}_\mathrm{eff}(\mathbf{r})$ is the effective Kohn-Sham potential which combines the classical and exchange-correlation potential. Since the Kohn-Sham approach is generally free of approximations, the exact ground state energy could in principle be obtained, given the exact exchange-correlation functional is known. Unlike in other wavefunction-based methods, the converged Kohn-Sham states $\Phi_i^\mathrm{KS}(\mathbf{r})$ and their corresponding eigenvalues ϵ_i^KS do not represent molecular orbitals (MOs) but lack any physical meaning. Depending on the chosen exchange-correlation functional though, they often exhibit similar shape and energy as seen for MOs [178–180].

3.1.3 Approximation for the Exchange-Correlation Functional

Following the Kohn-Sham approach, the *known* contributions in Equation (3.2), comprised of the classic Coulomb interactions and the kinetic energy of the non-interacting reference system, make for the largest part of the total energy. Only a small part is covered by the *unknown* exchange-correlation functional which needs to be approximated. This small portion though is decisive in achieving chemical accuracy as it involves physical effects originating from the missing static exchange and dynamic correlation [176]. Since there is no systematic way of improving such approximations of the exchange-correlation functional, they are to a certain extent always empiric. Approximate functionals can be classified into rungs based on the underlying approximation strategy [176].

Rung 1: Local Density Approximation (LDA)
Assuming the electron density is a slowly varying function, the problem can be reduced to local points in space. Describing these local density points with a corresponding homogeneous electron gas, the exchange-correlation energy can be calculated with high precision. The LDA approximation is applicable especially for extended systems with delocalized electronic states, such as metals, but fails for molecular systems with non-local effects resulting in a strongly inhomogeneous electronic density [176].

Rung 2: Generalized Gradient Approximation (GGA)
Building on the LDA approach, the GGA method considers also the local gradient of the electron density. Due to the improved performance for molecular and slab systems as compared to LDA functionals [181–183], this approximation is widely used in solid state applications [184]. A prominent GGA representative is the functional developed by Perdew, Burke and Ernzerhof (PBE) [185] which is also employed in the DFT calculations conducted herein.

Rung 3: meta-GGA
Including even higher order derivatives of the electron density constitutes the meta-GGA class of exchange-correlation functionals [186]. Depending on the specific application, improvements are not as significant in comparison to GGA functionals.

Rung 4: Hybrid functionals
Hybrid functionals are based on the idea to first calculate the exact exchange energy of the Kohn-Sham reference system from Hartree-Fock theory and incorporate them into LDA or GGA expressions. This mixing of exchange-correlation functional terms accounts for non-local contributions and reduces the self-interaction error [186].

3.2 Classical Force Field Potentials

Chemical systems can be described in terms of interactions between the constituting particles. In classical force field potentials, these interactions are modeled after analytical expressions motivated by physical behavior. Interaction parameters of these mathematical expressions need to be parameterized against higher-level theory or even experimental data. From a computational perspective, classical force fields are particularly attractive for larger length

and time scale simulations, as they neglect explicit electronic treatment thereby reducing computational cost significantly [176]. Effective parallelization of simulations based on classical force fields facilitates the study of systems beyond a billion atoms [187]. However, this computational efficiency often comes at the cost of chemical accuracy. The determining factors for the obtained accuracy of a classical force field are the underlying analytical expression, the parameterization and subsequent validation. Depending on the diversity of the reference data for parameterization, classical force fields are often limited in transferability between different chemical systems and physical states.

Classical force fields are parameterized for a specific class of materials. Owing to the inherently large system sizes, they are popular in biology and polymer research [188]. For molecular systems, which often possess characteristic chemical features such as covalent bonds, *cis-trans* configurational isomerism etc., explicit supplementary terms for bonds, bond angles, dihedrals, and out-of-plane distortions are added to the force field. Typically, the chosen analytical expressions for such terms are simple and for instance modeled via a harmonic spring [189]. Interactions in bulk materials like ionic solids and van der Waals systems can often be approximated by potentials which solely comprise pair-wise terms.

Since classical force field potentials do not account for the electronic structure but are based on static bonding information, they are unable to describe chemical reactions via bond formation and breaking or change of oxidation state. An increasingly popular extension to such force fields is the ReaxFF introduced by van Duin et al. [190], which relies on bond orders rather than explicit bonds. However, the parameterization of a ReaxFF is usually high-dimensional, requiring an extensive training set and an intricate parameterization scheme.

A recent addition are Machine-Learned force fields, which do not rely on analytical forms to mimic physical behavior. Instead, meaningful particle interactions are retrieved from a training set, sufficiently spanning the configurational space of interest. Current challenges of efficient training and computational performance scaling with higher order systems, however, often limit the applicability of these force fields to more complex systems [174, 175].

3.2.1 Born Model of Solids

Simple bulk materials can be approximately characterized via the Born Model of Solids [191]. Within this approach the interactions are isotropic and can be represented via solely two-body terms, i.e. the long-ranged Coulomb potential, short-range van der Waals interactions, and repulsive interactions due to Pauli repulsion [191].

In crystalline solids, the underlying infinitely extended ionic lattice induces an effective background potential which needs to be accounted for in the long-range Coulomb potential. A possible remedy is the incorporation of a correction term from the Ewald method [192] or the application of the Particle-Particle-Particle-Mesh (PPPM) formalism [193]. Short-range contributions originating from fluctuating dipoles of electron clouds, i.e. van der Waals interactions, can be derived from the polarization of averaged second order energies. These interactions exhibit a fast decay of ion eigen-energies Δ_i and ion polarizability α_i with parti-

cle distance r_{ij} according to $\frac{C_{ij}}{r_{ij}^6}$, with $C_{ij} = -\frac{2}{3}\frac{\Delta_i \Delta_j}{\Delta_i + \Delta_j}\alpha_i \alpha_j$. The short-range repulsion term is typically heuristically approximated using a Lennard-Jones or Buckingham potential [191]. The latter is described by an exponential expression $A_{ij}\exp(-\frac{r_{ij}}{\rho_{ij}})$ and the van der Waals interactions. Due to its particular analytical form, the Buckingham potential may suffer from instabilities at small values of r_{ij} [189].

Combination of these interaction potential contributions yields the Coulomb–Buckingham potential given as

$$U_{ij} = \underbrace{\frac{1}{4\pi\epsilon_0}\frac{q_i q_j}{r_{ij}}}_{\text{Coulomb}} + \underbrace{A_{ij}\exp\left(-\frac{r_{ij}}{\rho_{ij}}\right) - \frac{C_{ij}}{r_{ij}^6}}_{\text{Buckingham}}, \tag{3.5}$$

where ϵ_0 is the dielectric constant in vacuum, q_i are the ionic charges and A_{ij}, ρ_{ij} and C_{ij} are interaction specific constants which need to be parameterized. Since the parameterization is driven to reproduce reference data and not directly derived from quantum chemical calculations, potentials described by Equation (3.5) may include covalency information to a certain extent. As a result, high-quality force field potentials following the Born Model of Solids have been introduced for oxides, halogenides and polyanionic solids such as phosphates and silicates [194]. The original choice of point charges based on oxidation state, i.e. formal charges, is often replaced by fractional charges since they better describe the mean static polarization of ions. While fractional charges usually yield better results for the parameterized system, the underlying force fields are less transferable. The lower transferability can be attributed to these charges being highly dependent on the local chemical environment [195, 196].

3.2.2 Polarizable Core-Shell Model

Fractional charges account for polarization as an effective mean static potential in an isotropic fashion since they are treated as point charges. An extension to this simplified picture is the introduction of an anisotropically acting electronic polarization α. This extension is essential for improving bulk material properties such as ionic diffusion [197, 198]. Dick and Overhauser [199] have introduced a core-shell (cs) approach to model the polarization of ions. In this picture, the electrostatically induced deformation of the outer electronic shell [200, 201], is explicitly mimicked by a shell pseudoparticle attached to the original ion core. The interaction U_{cs} between the two and particles, i.e. core and shell particle, is described via a harmonic spring with

$$U_{\text{cs}} = k r_{\text{cs}}^2, \tag{3.6}$$

where r_{cs} is the core-shell distance and k is the spring force constant. The polarization is directly proportional to the induced dipole $p = q_{\text{s}} r_{\text{cs}}$ with the shell charge q_{s} and the induced

electric field E. Insertion of the harmonic force $F_{\mathrm{cs}} = kr_{\mathrm{cs}}$ into the electric field via $E = \frac{F}{q_{\mathrm{s}}}$ yields the polarizability as

$$\alpha = \frac{q_{\mathrm{s}}^2}{k}. \tag{3.7}$$

In MD simulations, a polarized core-shell pair yields a combined Coulomb interaction. Van der Waals as well as short-range repulsive interactions are assumed to act only between shells of different pairs, cf. Figure 3.1. This approximation introduces an error, scaling with the separation of two core-shell pairs $r_{\mathrm{cs}}^i - r_{\mathrm{cs}}^j$, which is negligibly small [199].

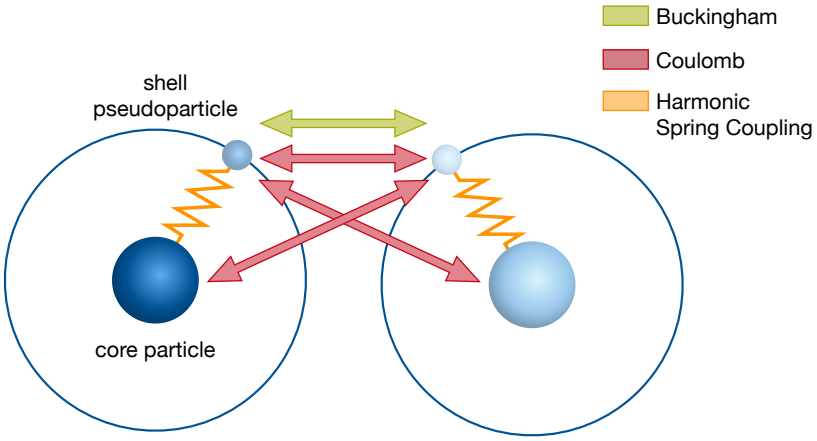

Figure 3.1: Schematic core-shell model. The internal interaction between core and shell particle is described via the harmonic potential U_{cs} ■. Short-range repulsion and van der Waals interactions ■ only act between the two shell pseudoparticles of two core-shell pairs, while the Coulomb interactions ■ act between cores and shells of the two pairs.

3.2.3 Force Field Parameterization

Classical force field parameterization typically is a high dimensional, non-linear problem. The number of parameters depends on the number of species N_{species} described by the force field and the number of parameters to be fitted by the choice of interaction potential. For a Buckingham potential there are three parameters A_{ij}, ρ_{ij} and C_{ij} per interaction pair. From combinatorics, the total number of parameters scales with

$$N_{\mathrm{parameters}} = N_{\mathrm{buck}} \binom{N_{\mathrm{species}} + 1}{2} = N_{\mathrm{buck}} \frac{(N_{\mathrm{species}} + 1)!}{2\,(N_{\mathrm{species}} - 1)!}. \tag{3.8}$$

If the force field contains additional terms, the parameter space is extended even further, e.g. by force constants in a harmonic potential. The number of species in a force field does not necessarily coincide with the number of chemical elements. In organic systems, carbons are often differentiated into multiple species according to their immediate local environment.

Training Strategy and Scoring Functions

In terms of training strategy, the reference structure set needs to entail the chemical systems of interest. For vast chemical spaces, it is beneficial to include local environments which are far from equilibrium. Following this approach, the training set is modified iteratively and intermediate potentials exploring the chemical subspaces eventually result in a robust and transferable force field potential. Such an iterative extension strategy is applied in the parameterization of the force field used in this work, see Section 4.3.1.

The force field parameters are fitted to a set of higher-level theory or empirical data. For *ab initio* based force fields, atomistic properties of the training structures, namely energy E, forces F and stress σ, are obtained from single point first-principles calculations. The reference system parameters are then compared to the analogous parameters obtained from the current force field parameter set yielding scoring functions in Equations (3.10) to (3.12) for ΔE, ΔF and $\Delta\sigma$. A cost function according to

$$\Gamma(\{p_i\}) = w_{\mathrm{E}}\Delta E + w_{\mathrm{F}}\Delta F + w_{\sigma}\Delta\sigma \tag{3.9}$$

enters into a global optimization scheme to find an optimum set of force field parameters to represent the training set [202, 203]. Here, $\{p_i\}$ is the parameter set describing all interactions in the force field, w_{E}, w_{F}, and w_{σ} are weights assigned to the contributions arising from respective energy, force, and stress deviations. A weight distribution with $w_{\mathrm{E}} \leq w_{\mathrm{F}}$ is often advantageous to account for the abundance of atomic force data versus the single energy per structure [203]. Such a weight consideration however, depends on the specific choice of scoring functions.

All scoring functions are normalized by the squared sum of the *ab initio* data. The energy scoring function ΔE is given as

$$\Delta E = \frac{\sqrt{\sum_{s,s'>s}\left[\left(E_s^{\mathrm{DFT}} - E_{s'}^{\mathrm{DFT}}\right) - \left(E_s^{\mathrm{FF}} - E_{s'}^{\mathrm{FF}}\right)\right]^2}}{\sqrt{\sum_{s,s'>s}\left[E_s^{\mathrm{DFT}} - E_{s'}^{\mathrm{DFT}}\right]^2}}, \tag{3.10}$$

where the subscript DFT denotes energies from *ab initio* single point calculations and FF the respective energy from the classical force field potential. The index s runs over all structures in the training set. Energies are only compared amongst structures with the same stoichiometry to account for relative, rather than total energies. The force scoring function ΔF is accordingly described via

$$\Delta F = \frac{\sqrt{\sum_{s,\alpha,\beta}\left[F_{s,\alpha,\beta}^{\mathrm{DFT}} - F_{s,\alpha,\beta}^{\mathrm{FF}}\right]^2}}{\sqrt{\sum_{s,\alpha,\beta}\left[F_{s,\alpha,\beta}^{\mathrm{DFT}}\right]^2}}, \tag{3.11}$$

with α running over atoms of the same structure and β denoting the cartesian coordinates x, y and z. Lastly, the stress scoring function $\Delta\sigma$ is formulated as

$$\Delta\sigma = \frac{\sqrt{\sum_{s,\beta_i,\beta_j} \left[\sigma^{\mathrm{DFT}}_{s,\beta_i,\beta_j} - \sigma^{\mathrm{FF}}_{s,\beta_i,\beta_j}\right]^2}}{\sqrt{\sum_{s,\beta_i,\beta_j} \left[\sigma^{\mathrm{DFT}}_{s,\beta_i,\beta_j}\right]^2}}, \tag{3.12}$$

with the stress tensor $\sigma_{\beta_i,\beta_j} = -\frac{\sum_\alpha r_{\beta_i} f_{\beta_j}}{3V}$ as given by the virial theorem. Here, β_i and β_j describe cartesian directions yielding orthogonal tensor components σ_{xx}, σ_{yy} and σ_{zz} and the respective off-diagonal elements.

Global and Local Parameter Optimization

Optimum force field parameters are obtained by minimizing the non-linear cost function Γ given in Equation (3.9). Due to the high-dimensionality of the optimization problem, cf. Equation (3.8), a thorough global optimization strategy is required which is typically followed by local optimization. A comprehensive overview of optimization algorithms is given in Ref. [204].

The multidimensional cost function hypersurface is likely comprised of multiple superbasins and local minima. Therefore, heuristic methods need to be employed for efficient global optimization. Evolutionary motivated algorithms satisfy such complex optimization problems. In this thesis, a Genetic Algorithm (GA) as implemented in the General Utility Lattice Program (GULP) [205] and a Particle Swarm Optimizer (PSO) as implemented in the *INSPYRED* python package [206] are employed.

Genetic Algorithm (GA): In this approach, a selection procedure is applied mimicking Darwin's theory of evolution. The algorithm is initiated by randomly chosen configurations, i.e. parameter sets $\{p_i\}$, which evolve iteratively. Each parameter is encoded as a binary string by normalizing to the respective parameter bounds. The initial parameter set evolves according to the following principles. Firstly, random pairs of parameter configurations are chosen and compared according to their fitness, cf. Equation (3.9). The *fitter* set is inherited by the next generation, while the *weaker* set is passed on with a randomly drawn probability. This *reproduction* process is repeated as many times as there are configurations to maintain a constant count of individuals. Secondly, two parent configurations may be *crossed-over* to create a new individual with potentially higher fitness. This can be achieved by taking a weighted average of the parent binary strings. Thirdly, new individuals are created by randomly modifying a parent binary string to represent genetic *mutation*. This process occurs with a certain probability, i.e. the mutation rate. The final result from a GA is a number of configurations, from which the *fittest* is selected. Unless the GA confidently runs into a smooth global minimum, it may be beneficial to investigate a sample of *fittest* configurations via subsequent local optimization.

Particle Swarm Optimization (PSO): The PSO approach is mimicking *swarm intelligence* as often observed in fish or bird swarms. Similar to a GA, an initial population, or *swarm* in

the PSO jargon, of random parameter sets is found. Individuals are referred to as *particles* and move through the optimization process with a certain velocity v_i defined by the algorithm. Initial velocities are either uniformly distributed at the parameter bounds or follow a normal gaussian distribution. In each iteration or timestep t, the particle position and velocity is updated based on individual and collective memory. Both, individual p_i^{best} and collective p_g^{best} highest scores are stored for each iteration. Therefore, an individual particle is not only influenced by its own personal best score, but benefits also from the *swarm* best score with

$$v_i(t+1) = c_0 v_i(t) + c_1 n_1 (p_i^{\text{best}} - p_i(t)) + c_1 n_1 (p_g^{\text{best}} - p_i(t)). \tag{3.13}$$

Randomizing (n_1, n_2) and weighing (c_0, c_1, c_2) of these contributions allows for a robust exploration of parameter space and tuning of a particle's exploration ability. The weights are termed c_0 inertia, c_1 cognitive rate, and c_2 social rate. Analogous to the GA, a local optimization should be coupled to the PSO approach as single particles only draw the swarm slowly to a current minimum.

Local optimization of parameter samples from global optimization is subsequently performed by using either a Newton-Raphson optimizer in the GULP framework or a Limited-memory Broyden-Fletcher-Goldfarb-Shanno (L-BFGS) algorithm as implemented in the *SciPy* python library [207].

3.3 Molecular Dynamics Simulations

MD Simulations allow for the study of dynamical system properties from time evolution statistics. Therefore, the atomistic model of interest is propagated in time obeying classical mechanical laws, i.e. Newton's equations of motion.

3.3.1 Integration of Equations of Motion

In order to compute time resolved atomistic trajectories, the equations of motion need to be integrated over time. The corresponding time step for integration Δt should be as large as possible to minimize computational cost, yet it needs to be small enough to resolve particle motion. An established algorithm to numerically solve this problem is the Velocity Verlet algorithm [208] as implemented in the LAMMPS MD Simulator [209].

To account for errors introduced by numerical integration, i.e. the choice of a finite time step, certain physical principles must not be violated. First, the energy or effective energy, respectively, needs to be conserved. In this regard, short and long term energy drifts need to be corrected. Second, complying with Newton's equations of motion, particle movement needs to be reversible in time. Therefore, in order to retrieve forward and backward particle motion, the integration scheme needs to be symmetric with time as well. Lastly, the phase space needs to be conserved. In a broader sense, this means that a meaningful statistical ensemble needs to be maintained upon integration.

In deriving the Velocity Verlet algorithm, the required velocity $v(t)$ and change in momentum via the force $f(t)$ at a point in time is readily obtained from classical force field calculations. Time symmetrical approximation of the particle position, i.e. $r(t+\Delta t)$ and $r(t-\Delta t)$, is considered utilizing Taylor expansions up to the fourth order. By combining forward and backward time evolution, odd power terms in Δt are canceled. If fourth order terms are further assumed to be negligible, the Verlet algorithm with

$$r(t+\Delta t) \approx 2r(t) - r(t-\Delta t) + \frac{f(t)}{m}\Delta t^2 \tag{3.14}$$

is obtained. While the Verlet algorithm presents a robust integration scheme, the particle velocity is not explicitly included resulting in errors on the order of Δt^2. A natural extension is to include the velocity which yields the Velocity Verlet algorithm with

$$r(t+\Delta t) = r(t) + v(t)\Delta t + \frac{f(t)}{2m}\Delta t^2. \tag{3.15}$$

The velocity

$$v(t+\Delta t) = v(t) + \frac{f(t+\Delta t) + f(t)}{2m}\Delta t \tag{3.16}$$

needs to be computed in an extra step. Alternative algorithms including higher order Taylor expansion terms are provided in Ref [208].

3.3.2 Implementation of the Adiabatic Core-Shell Model

The core-shell polarization approach, cf. Section 3.2.2, as implemented in the LAMMPS Simulator [210] follows the *adiabatic* core-shell model by Mitchell and Finchman [198]. The artificial splitting of a single ion into a core-shell pair introduces additional *technical* degrees of freedom as compared to the *physical* system. In the model introduced by Mitchell and Finchman, the shell pseudoparticle is given a fraction of the core particle's mass (m_s and m_c). In other implementation schemes, the shell particle resembles an electron cloud and according to the Born-Oppenheimer approximation has negligible mass. However, assigning a mass fraction allows for the shell particle to be included in the overall propagation scheme. The required mass fraction can be derived from an oscillation frequency ν_cs modeled after a harmonic oscillator as

$$\nu_\mathrm{cs} = \frac{1}{2\pi}\sqrt{\frac{\mu}{k}} \quad \text{with} \quad \mu = \frac{m_\mathrm{c} m_\mathrm{s}}{m_\mathrm{c} + m_\mathrm{s}}, \tag{3.17}$$

where k is the spring constant and μ is the effective mass. To ensure instantaneous relaxation of the shell particle, the oscillation frequency needs to be significantly higher than the atomic vibrations.

Special attention needs to be drawn to the core-shell system when thermostating, i.e. conducting constant temperature MD simulations. This is particularly the case for initialization

and equilibration of the technical core-shell system. Upon assigning initial velocities, relative motion between the core and shell particle must be avoided. A thermostat must then rescale the Center Of Mass (COM) of the core-shell pair in order to not influence the *technical* degree of freedom. While some energy will inevitably flow into the artificial degree of freedom to account for polarization, the decoupling from the thermostat and high core-shell vibrations ν_{cs} ensure this energy transfer to be minimal. After equilibration the core-shell subsystem is considered thermalized and non-elastic interactions with neighboring particles are not expected to lead to further energy leackage into the core-shell motion [198].

In a physical system, the instantaneous temperature T for thermostatting is defined by

$$T = \frac{2}{3Nk_{\mathrm{B}}}K = \frac{1}{3Nk_{\mathrm{B}}}\sum_{i}^{N} m_i v_i^2, \tag{3.18}$$

with the Boltzmann constant k_{B}, the number of particles N, the kinetic energy K, and m_i and v_i the particle mass and velocity [211]. The instantaneous pressure P is given by

$$P = \frac{2}{3V}K + \frac{1}{3V}W = \frac{1}{3V}\sum_{i}^{N} m_i v_i^2 + \frac{1}{3V}\sum_{i}^{N} r_i f_i, \tag{3.19}$$

with W the internal virial, V the system volume and r_i and f_i the particle position and force. In the adiabatic core-shell picture, the temperature may either depend on the COM velocity of core-shell pairs or all velocities, including relative core-shell motion. Regardless of the exact definition, the $3N$ degrees of freedom entering into the temperature correspond to the actual physical system [198]. For the pressure definition, the core and shell particles are treated as separate atoms. Here, the kinetic contribution of all atoms and the force contribution to the system virial W needs to be taken into account [212]. The adiabatic core-shell model requires fairly small time steps Δt in order to resolve the fast core-shell motion.

3.4 Ion Dynamics – Microscopic to Macroscopic Extrapolation

Diffusion of ions through solid electrolytes is a key performance criterion. Computationally, the motion of individual ions can be resolved with high accuracy. However, statistical mechanics is needed to extrapolate from averaged ensemble properties to apparent macroscopic coefficients. Such a relation from microscopic to macroscopic ion transport quantities can be described by the Einstein formalism. Following this formalism, a macroscopic transport coefficient λ can be expressed from a dynamic variable A as

$$2\Delta t\lambda = \langle (A(t) - A(0))^2 \rangle. \tag{3.20}$$

The Einstein formalism is originally based on Brownian motion and holds only at long sampling times [211, 213]. For ionic diffusion, the dynamic variable of interest is a displacement of atoms, i.e. the Mean Square Displacement (MSD) of charge carriers

$$\mathrm{MSD}(t) \equiv \langle |\vec{r_i}(t) - \vec{r_i}(0)|^2 \rangle, \tag{3.21}$$

with $\vec{r_i}$ the position of atom i. To reduce statistical errors, a lag time τ is introduced via

$$\mathrm{MSD}(\tau) \equiv \langle |\vec{r_i}(t+\tau) - \vec{r_i}(t)|^2 \rangle. \tag{3.22}$$

The displacement of atoms is considered in different intervals and shifted along the trajectory with simulation time t [214]. A schematic lag time averaging is illustrated in Figure 3.2.

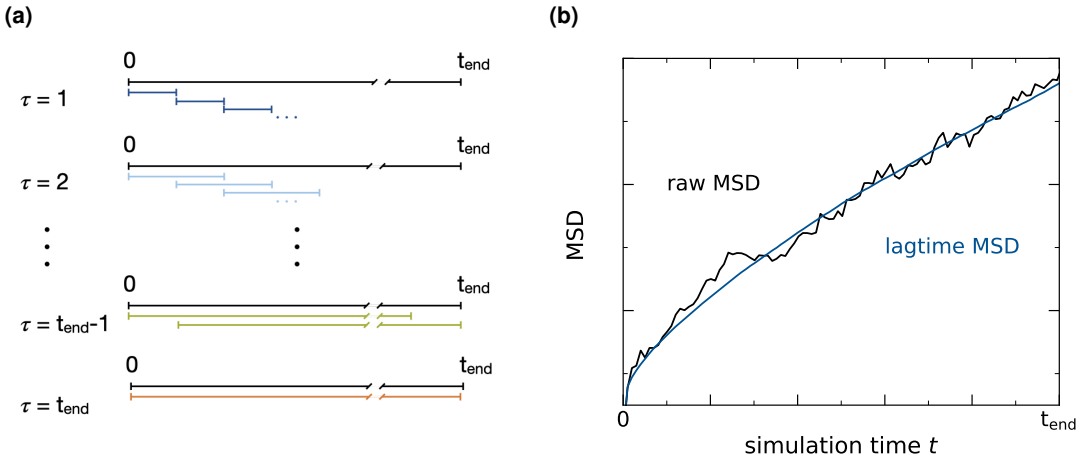

Figure 3.2: Lag time averaging of MSD. **(a)** Sliding lag time across simulation trajectory for different values of τ. **(b)** Smoothing of MSD from lag time averaging of *raw* MSD.

As shown in Figure 3.2 (b), this statistical averaging leads to a smoothing of the *raw* MSD, which is retrieved from considering only the first frame of the MD simulation for atomic displacements.

The tracer diffusion coefficient D^* based on the ensemble averaged MSD is defined as

$$D^* = \frac{1}{3} \frac{\langle |\vec{r_i}(t+\tau) - \vec{r_i}(t)|^2 \rangle_\tau}{2\Delta t}, \tag{3.23}$$

where Δt is the sampling time and the prefactor $1/3$ accounts for the three spatial dimensions. The tracer diffusion was originally applied to a system of non-interacting particles, i.e. random walkers in a homogeneous medium [213]. Findings by He et al. [215] suggest the relevant sampling regime for macroscopic extrapolation to be above 10 % of the sampling time, to exclude ballistic motion, and below 70 %, due to poor observed linearity from statistics. A corresponding MSD and its regime separation is shown in Figure 3.3 (a).

Such a partitioning of ion trajectories is generally possible for any given sampling time. The underlying assumption of the Einstein formalism, however, requires a sufficiently long sampling. To identify an appropriate simulation time, the phenomenological diffusion regimes can be quantified via the anomalous diffusion coefficient α given as $\mathrm{MSD} \propto t^\alpha$ [216]. Figure 3.3 (b) schematically shows the ballistic regime at $\alpha = 2$, an intermediate correlated

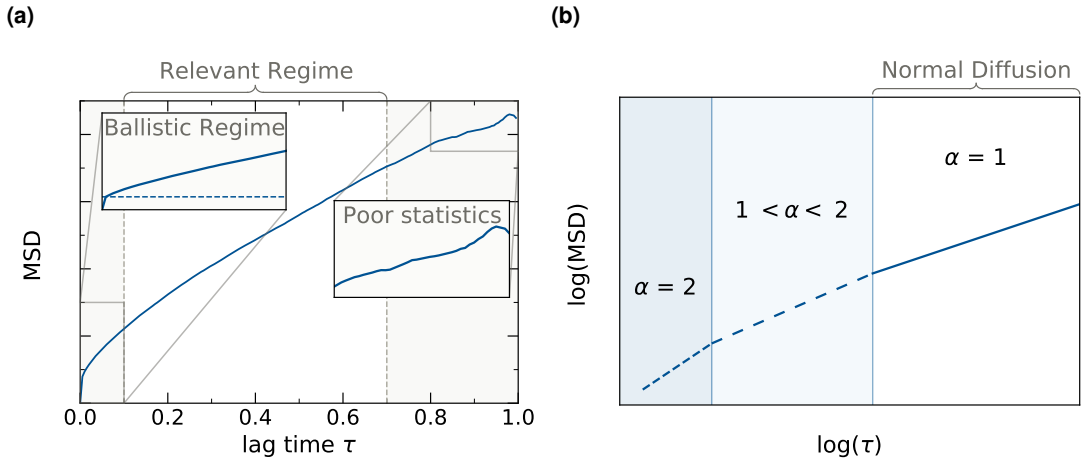

Figure 3.3: Ion dynamic regimes. **(a)** Schematic MSD over simulation time τ for the lag time averaged and raw trajectory. According to He et al. [215] only a regime between 10–70 % of the sampling time qualifies for statistical averaging due to the ballistic regime at smaller times and poor statistical sampling at larger times. **(b)** Separation of dynamics into diffusion regimes based on the anomalous coefficient α with $\mathrm{MSD} \propto t^{\alpha}$. Only at α=1 *normal diffusion* is observed as required by the Einstein formalism.

motion regime and eventually the long range ion transport regime for $\alpha = 1$. Only in the latter, the Einstein formalism holds for what is referred to as *normal diffusion*.

Another macroscopic property which is typically of interest for battery materials is the ionic conductivity. Considering slight changes of an external field acting on an ionic system, the induced small perturbation can be formulated as a response of the microscopic currents

$$\vec{j}^{\mathrm{ion}} = \sum_{i=1}^{N} q_i \vec{v}_i. \tag{3.24}$$

Here, N is the number of particles i with charge q_i and velocity $\vec{v}_i$. By time integration and neglecting of cross-correlation terms, an idealized ionic conductivity σ^* can be expressed via the tracer diffusion coefficient as

$$\sigma^* = \frac{1}{3Vk_{\mathrm{B}}T} \int_0^{\infty} \left\langle \sum_{i=1}^{N} q_i^2 \vec{v}_i(t)\vec{v}_i(0) + \underbrace{\sum_{i=1}^{N}\sum_{j\neq i}^{N} q_i q_j \vec{v}_i(t)\vec{v}_j(0)}_{\text{cross-correlation term}} \right\rangle dt \tag{3.25a}$$

$$= \frac{1}{3Vk_{\mathrm{B}}T} \sum_{\beta}^{n_\beta} q_\beta^2 D_\beta^* N_\beta \tag{3.25b}$$

In this so-called Nernst-Einstein relation [213], V is the cell volume, k_B is the Boltzmann-constant, T is the system temperature and q_β, D^*_β, N_β are the charge, tracer diffusion coefficient and number of particles of species β, respectively.

An extrapolation from microscopic, atomistic motion to macroscopic properties requires sufficient statistical sampling. This means sufficiently long simulation trajectories and system sizes to capture rare ion hopping events. For elevated simulation temperatures, ions may surpass diffusion barriers more easily and thus more frequently. At ambient temperatures, however, these rare events are often not sampled sufficiently within accessible simulation length and time scales. As a result, errors attributed to diffusion coefficients and ionic conductivities are significantly larger at lower temperatures [1].

3.5 TEM Image Simulation

TEM is a well-established microscopy technique in which electrons are transmitted through a probe, i.e. specimen, forming an image determined by the electron-probe interaction. In comparison to optical microscopes, TEM allows for the imaging of orders of magnitude smaller samples with significantly higher resolution. The physical reason behind this is the inherently small de Broglie wavelength of electrons in the pm-range as compared to visible light in the 400–700 nm range. A microscope's theoretical resolution is directly proportional to the wavelength of the employed particles.

Depending on the experimental setup, there are different variants of TEM techniques. The Conventional TEM (CTEM) is defined by a rather broad electron beam with apertures between 5–20 mrad and a uniform current density [217]. An immediate advancement is the High-Resolution TEM (HRTEM), which features objective apertures greater than 20 mrad to absorb electrons scattered at large angles, thereby reducing background noise. Another increasingly popular method is the Scanning TEM (STEM) technique. In a STEM setup, the electron beam is more narrow and an area of the specimen is scanned over. An advantage of the STEM method is the absence of lens aberrations, which require complex post processing. In CTEM and HRTEM, the resulting images are rather complex and simulation tools need to be utilized for their analysis.

Herein, a brief outline of the TEM method, i.e. CTEM and HRTEM, and corresponding implementation as used in the Dr. Probe Software [218] is given. An extensive overview of TEM techniques and underlying physical background can be found in Ref. [217].

3.5.1 Electron-Probe Formation

In a TEM setup, incident electrons are initially accelerated by a microscope voltage U, resulting in electron kinetic energies of $E_\mathrm{kin} = eU$. Considering the wave-like properties hypothesized by de Broglie, the voltage dependent electron wavelength is given as

$$\lambda = \frac{h\,c}{\sqrt{E_\mathrm{kin}(m_0c^2 + E_\mathrm{kin})}}, \tag{3.26}$$

where h is Planck's constant, c is the speed of light and m_0 is the rest mass of the electron. The electron beam is then focused along the z-axis on a point $\mathbf{R}(x, y)$ of the specimen plane. Interactions between the incident electrons and the specimen lead to scattering and diffraction of the former. Figure 3.4 schematically shows the different forms of possible interactions for thin specimen.

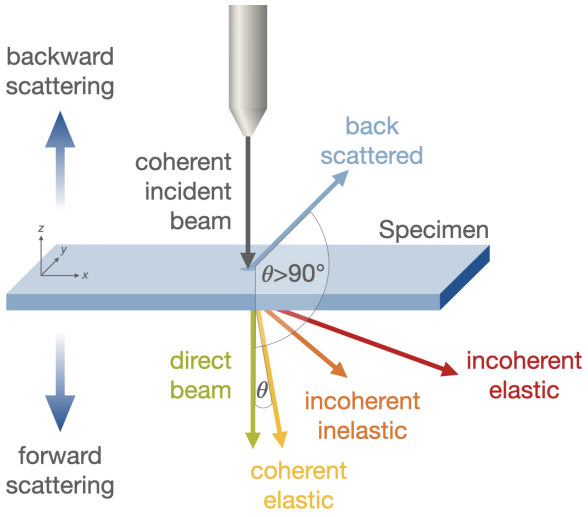

Figure 3.4: TEM interactions between an incident electron beam and the specimen. Forward versus backward scattering depending on the scattering angle θ. Forward scattering is differentiated into elastic scattering, with no loss in energy, and inelastic scattering. For small angles $\theta < 10°$, the scattering is typically coherent, i.e. in phase with the incident beam.

In TEM image formation, only the *forward scattered*, i.e. electrons scattered at angles <90°, are relevant. Furthermore, explicit simulation by the Dr. Probe Software [218] is limited to electrons with insignificant energy loss and low scattering angles between 1–10° [219]. In this picture, energy loss from e.g. plasmon excitation, surface plasmons or interband transitions is neglected. To incorporate inelastic contributions in simulation, multiple quasi-elastic substitute images at different defocus values are superposed to form the resulting images, see Section 4.4.3. However, merely the optical effect of energy loss is accounted for and this approach does not accurately describe the physical inelastic scattering of electrons.

The incident electrons can be described in a conjugate reciprocal-space plane with vectors $\mathbf{k}_{x,y}$ according to

$$\Psi_0(\mathbf{k};\mathbf{R}) = A(\mathbf{k}) \exp\left[-\mathrm{i}\chi(\mathbf{k})\right] \exp\left[-2\pi\mathrm{i}\,\mathbf{k}\cdot\mathbf{R}\right], \tag{3.27}$$

where $A(\mathbf{k})$ is an aperture function and $\chi(\mathbf{k})$ describes the coherent aberrations within the probe. The vector $\mathbf{k}$ is assumed to be two-dimensional as in the small angle approximation. For incident electrons perpendicular to the specimen surface, contributions along z are negligible. The aperture function $A(\mathbf{k})$ ensures a sufficiently narrow beam focus by blocking incident electrons with angles larger than a given objective aperture $\theta > \alpha$ from the z-axis.

Transmitted electrons which have travelled through the specimen are passed to the imaging system of the TEM setup. Due to multiple objective, intermediate, and projector lenses in the experimental setup, the electrons experience lens specific aberrations [217]. To model these deviations, the aberration function

$$\chi(\mathbf{k}) = \frac{2\pi}{\lambda}\mathfrak{R}\left[\sum_{j=1}^{N}\sum_{l=0}^{L(j)}\frac{C_{j+l-1,j-l}}{j+l}\lambda^{j+l}(k^*)^j k^l\right] \tag{3.28}$$

is introduced, where N is the aberration expansion order. $L(j)$ is a dynamic limit to minimize $\min(j, N-j)$, such that $1 \leq j+l \leq N$. The symbol $\mathfrak{R}$ denotes to only consider the real part of the polynomial as a function of complex wave-vector components $k = k_x + \mathrm{i}\, k_y$ and complex-valued aberration coefficients $C_{m,n} = C_{m,n,x} + \mathrm{i}\, C_{m,n,y}$. The most dominant aberrations in common TEM setups are the defocus $C_{1,0}$, or Δz, and the spherical aberration $C_{3,0}$, or C_s [217]. Taking these two aberration orders into account, Equation (3.28) becomes rotationally symmetric about the optical axis of the microscope and can be simplified to

$$\chi(k) = \frac{\pi}{2}C_s\lambda^3 k^4 - \pi\Delta z\lambda k^2. \tag{3.29}$$

The defocus can be adjusted in experiment and enters as a parameter into the simulation of TEM images. A common approach to choose an optimum defocus value is the Scherzer defocus given as

$$\Delta z_{\mathrm{Scherzer}} = \sqrt{\frac{4}{3}\lambda C_s}. \tag{3.30}$$

In Equation (3.29), the k^4 term is countered by the $\Delta z\, k^2$ term to flatten the overall aberration function $\chi(k)$. This allows for a transfer of low spatial frequencies k into image intensity with a similar phase. To obtain the probe wave function in real space, an inverse Fourier transformation of Equation (3.27) is performed.

3.5.2 Electron Diffraction Calculations

A common approach to simulate electron scattering in specimen with finite thickness is the Multislice method introduced by Cowley and Moodie [220]. The atomistic structure is partitioned into slices j along the z-dimension which ideally contain only one monolayer of atoms. The electron scattering is mathematically described by multiplication of the wave function with a transmission function $T_j(\mathbf{r})$. Propagation of the wave function to the next slice is approximated by a propagation through vacuum. Mathematically this propagation is described as the multiplication of the scattering result with a propagator function $P_j(\mathbf{k})$ in reciprocal space. By translating into reciprocal space via the Fourier transform $\mathfrak{F}$, a convo-

lution of transmission and propagation can be reformulated as a multiplication. The wave function in a subsequent slice Ψ_{j+1} can thus be expressed as

$$\Psi_{j+1}(\mathbf{r}) = \mathfrak{F}^{-1}\underbrace{\left[P_j(\mathbf{k})\ \mathfrak{F}\underbrace{\left[T_j(\mathbf{r})\Psi_j(\mathbf{r})\right]}_{\text{scattering}}\right]}_{\text{propagation}}. \tag{3.31}$$

Starting with the incident wave function Ψ_0 as described in Equation (3.27) in slice j=0, this sequence is repeated until the target specimen thickness is reached. Computationally, the Fast numerical Fourier Transform (FFT) algorithm as described by Ishizuka and Uyeda [221] is employed. Figure 3.5 schematically shows the scattering and propagation of an incident wave function through a specimen with finite thickness according to the Multislice method.

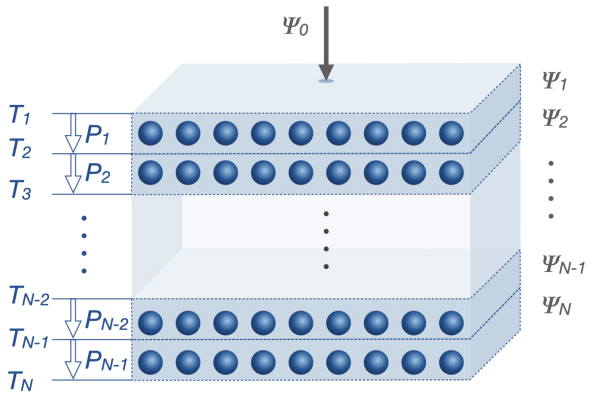

Figure 3.5: Schematic of the TEM Multislice method. The specimen is partitioned into slices and scattering of the incident electron beam Ψ_0 is accounted for by a transmission function T_j followed by propagation of the propagator function P_j. Iterative scattering and propagation yields the final electron wave function Ψ_N.

The transmission function describes scattering of the electrons from the specimen atoms in a given slice by the phase change to the wave function. Assuming high electron energies, i.e. $m_0c^2 \gg V(\mathbf{r})$, the phase change can be expressed in terms of a projected scattering potential $V_j^P(\mathbf{r})$ as

$$T_j(\mathbf{r}) = \exp\left[i\sigma V_j^P(\mathbf{r})\right] \quad \text{with} \quad V_j^P(\mathbf{r}) = \int_{z_j}^{z_{j+1}} V(\mathbf{r},z)dz. \tag{3.32}$$

The interaction constant is given as $\sigma = m\lambda/(2\pi\hbar^2)$, where $m = \gamma m_0$ with $\gamma = 1 + eU/(m_0c^2)$ and $\hbar = h/(2\pi)$. The projected potentials $V_j^P(\mathbf{r})$ are integrals of the formally three dimensional scattering potential along the z-axis.

The propagator function accounts for a phase shift χ_j of the plane waves after diffraction. It is described as

$$P_j(\mathbf{k}) = \exp\left[-i\chi_j\right] \quad \text{with} \quad \chi_j = \frac{2\pi}{\lambda}\Delta s_j, \tag{3.33}$$

where a phase shift under a given diffraction angle is proportional to a respective difference in optical path Δs_j. In principle, the geometrical considerations of scattering angles allows for the simulation of tilted crystal structures away from the zone axis. However, the approximation of small angle values significantly reduces complexity. Simulated TEM images in this work strictly follow a specimen alignment along the z-axis.

3.5.3 Thermal-Diffusive Scattering

Thermal-diffusive scattering leads to loss of probe current due to phonon excitation. To account for these effects in simulation, the frozen-lattice approach is applied [222]. Herein, a random atomic displacement is added to the particles, following a normal distribution. The Root Mean Square Displacement (RMSD) with

$$\mathrm{RMSD} \equiv \left[\langle|\vec{r_i}(t) - \vec{r_i}(0)|^2\rangle\right]^{1/2}, \tag{3.34}$$

is parameterized by isotropic, equivalent thermal-displacement parameters. These parameters, referred to as Debye-Waller factors, with

$$B_{\mathrm{iso}} = 8\pi^2 U_{\mathrm{iso}} = 8\pi^2 \langle \mathrm{RMSD}\rangle^2, \tag{3.35}$$

are provided for each atomic species individually. In each slice, random displacements are added to each atom position $\mathbf{R}_{\alpha,l}$ in equilibrium, which are drawn from a normal distribution scaled to the respective Debye-Waller factor. From this, a structure factor can be computed which enters in the numerical realization of the transmission function. A pre-calculated set of frozen states with different displacements for each slice of the input structure is prepared. The specific transmission function then randomly chooses from this set to account for slightly displaced atoms from thermal vibration.

The resulting simulated TEM images accounting for thermal-diffusive behavior are more realistic and better reproduce experimentally measured images. This is especially important for materials with higher atom mobility, see Section 4.4.3.

4 Protective nanoscale Complexion at Grain Boundaries in LATP[4.1]

The focus of this chapter is to disentangle the ambiguous role of grain boundaries in solid state electrolytes for the specific $Li_{1+x}Al_xTi_{2-x}(PO_4)_3$ (LATP) material. Intricate experiments allow for the structural and chemical resolution of such grain boundaries at the nanoscale. By leveraging these experimental findings, a novel approach to atomistically model realistic, multi-phase grain boundaries is introduced. The computational models verify the formation of distinct complexions encapsulating the LATP grains. Dynamic analyses suggest that LATP grain boundaries, and thus the newly found complexions, do not present an insuperable diffusion bottleneck. Furthermore, electronic structure calculations predict a local spatial separation of mobile Li ions from reducing electrons, which effectively suppresses dendrite nucleation. The complexions therefore serve as a thin protective layer coating the grains.

The pursued closely interlinked experiment-theory approach presented herein, is crucial to bridge the complexity gap of solid-solid interfaces. To provide a holistic picture, contributions of experimental collaborators will briefly be outlined.

4.1 Motivation

In order to advance in the technical realization of ASSBs, contact instabilities at solid-solid interfaces need to be resolved, see Section 2.3. Among the most prominent interfacial challenges are nucleation and growth of metallic Li dendrites [29, 30, 223]. The problem becomes emphasized when employing a LMA. To better understand the mechanism behind dendrite proliferation, bulk thermodynamic properties of the phases in contact have been of focus. In this context, large-scale material screening for interfacial compatibility has been conducted both, experimentally and via high-throughput computational studies [41, 42]. A possible remedy to dendrite growth is the introduction of coating materials or the targeted formation of passivizing interphases. For liquid electrolytes, the evolution of such a SEI has proven to be crucial for stable cycling [224].

[4.1] Adapted in parts from Stegmaier et al. [1] under CC BY 4.0.

Naturally forming and thermodynamically stable nanometer sized interphases, i.e. complexions [43–46], at grain boundaries may serve exactly such a protective purpose in the LATP solid electrolyte.

Due to their mechanical softness, the grain boundary network in SSEs often presents an accessible route for dendrite penetration and proliferation [29, 33]. The focus is typically on nucleation at the anode and penetration into the network of the SSE bulk phase. However, recent studies have shown that dendrites may nucleate within the bulk SSE itself [35–37]. In Section 2.3, two main reasons for this have been introduced. First, an overshoot in Li chemical potential above the standard chemical potential of Li metal [38, 39] and second, a high residual local electronic conductivity [40]. Consequently, a minimization of residual electronic conductivity in the solid electrolyte is desirable.

Han et al. have recently proposed dendrite-free operation in ASSB setups to require low electronic conductivities of the underlying SSE material [40]. In their work, they postulate critical values of current densities of $\approx 1-10\ \mathrm{mA\,cm^{-2}}$ and electronic conductivities below $\approx 10^{-10}-10^{-12}\ \mathrm{S\,cm^{-1}}$ [40]. When defining such critical values for material properties, i.e. ionic or electronic conductivity, these are typically bulk specific. However, to date there is no reported SSE material exhibiting such an extremely low bulk electronic conductivity and a concurrent satisfactorily large ionic conductivity.

Defying this picture of required absolute bulk properties, the super ionic conducting LATP SSE material has exhibited high cycling stability against dendrite formation [146, 169]. This is intriguing, as the measured electronic conductivity is orders of magnitude larger than the suggested critical value. Changes in local electrochemical stability and charge carrier mobility on the scale of a few nanometers, are hypothesized herein to crucially impact macroscopic material properties. Other research fields, i.e. semiconductor physics [225] and nano-ionics [226, 227], already actively exploit such local phenomena to design high-performing materials.

The particular properties of complexions at the LATP grain boundary interface are assumed to be responsible for the observed high stability and dendrite suppression capability of this SSE. The existence of these complexions is supported by a joint experimental-computational ansatz. Structural and chemical experimental insights of the interfacial built up are incorporated into an atomistic grain boundary model. It is found that the crystalline grains are capped by a distinct complexion at the surface and the adjacent grain boundary is highly amorphous. Computational atomistic simulations are crucial to resolve charge carrier dynamics on the nano-scale. A high Li mobility is identified within the amorphous part, while the thin complexion presents a sizable intergranular electronic impedance. The complexions therefore serve as a thin protective layer coating the LATP grains.

A classification of viable SSE candidates based on bulk properties alone, does not suffice for dendrite-free operation. The importance of local motifs, such as complexions found in this work, adds to a more nuanced understanding of solid-solid interfaces in SSEs.

4.2 Experimental Insights

4.2.1 LATP Synthesis and DC Polarization Measurements[4.2]

The LATP material for experimental analyses is prepared from a precalcined Li-Al-Ti-P-O powder precursor. Electrolyte pellets are die pressed at 177 MPa and subsequently cold isostatically pressed at 504 MPa. The powder is compacted and densified via sintering at a heating rate of 0.2 K min^{-1} to a maximum temperature of 1100 °C. After maintaining this sintering temperature for eight hours in ambient atmosphere, the pellet thickness is controlled not to exceed 300 µm. A detailed synthesis protocol is provided by Yu et al. [33].

To obtain the electronic conductivity Direct Current Polarization (DC) measurements are conducted of a LATP pellet. The pellet is prepared with 0.284 mm thickness and 9.82 mm diameter and sputtered with a thin Au layer of approximately 300 nm on each side. Measurements are performed on a Cu/LATP/Cu setup with two copper ion blocking electrodes. A current-time decay curve of such a cell under DC polarization is shown in Figure 4.1.

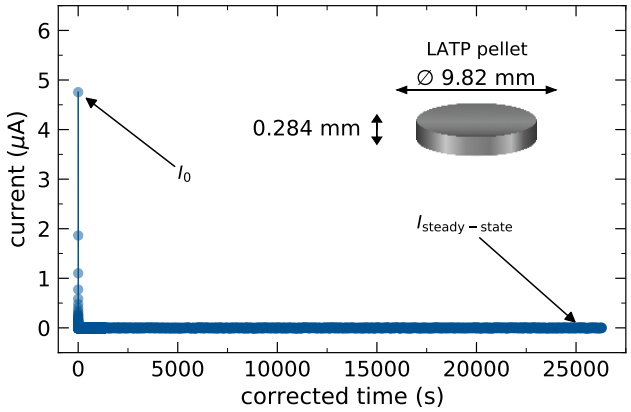

Figure 4.1: Current-time decay curve for DC polarization measurement of a Cu/LATP/Cu cell at 11 mV at 50 °C. Image adapted from Stegmaier et al. [1] under CC BY 4.0.

A constant voltage of 11 mV at 50 °C is applied over a polarization time of ≈26,000 s, i.e. 7.3 h. An initial current drop I_0 is observed, after which a steady state $I_{\mathrm{steady-state}}$, associated with electronic leakage, is reached. The DC polarization measurements yield an upper limit to the bulk electronic conductivity σ_{el} of 4.7·10^{-9} S cm^{-1}. This value is by 1 – 3 orders of magnitude larger than the suggested critical bulk value by Han et al. [40]. In conjunction with reported high cycling stability of LATP [33, 146], these experimental findings motivate further in depth analyses.

[4.2] LATP material synthesis and DC polarization measurements were conducted by Dr. S. Yu, Institute of Energy and Climate Research Fundamental Electrochemistry (IEK-9), Forschungszentrum Jülich.

4.2.2 Transmission Electron Microscopy[4.3]

High Resolution TEM (HRTEM) images are conducted on LATP samples featuring a grain boundary. The image shown in Figure 4.2 (a) reveals an extended grain boundary of ≈9 nm width. Microscopy of multiple such LATP samples yields widths between 5 – 20 nm, which is in agreement with reported ranges from Atomic Force Microscopy (AFM) line scans [47].

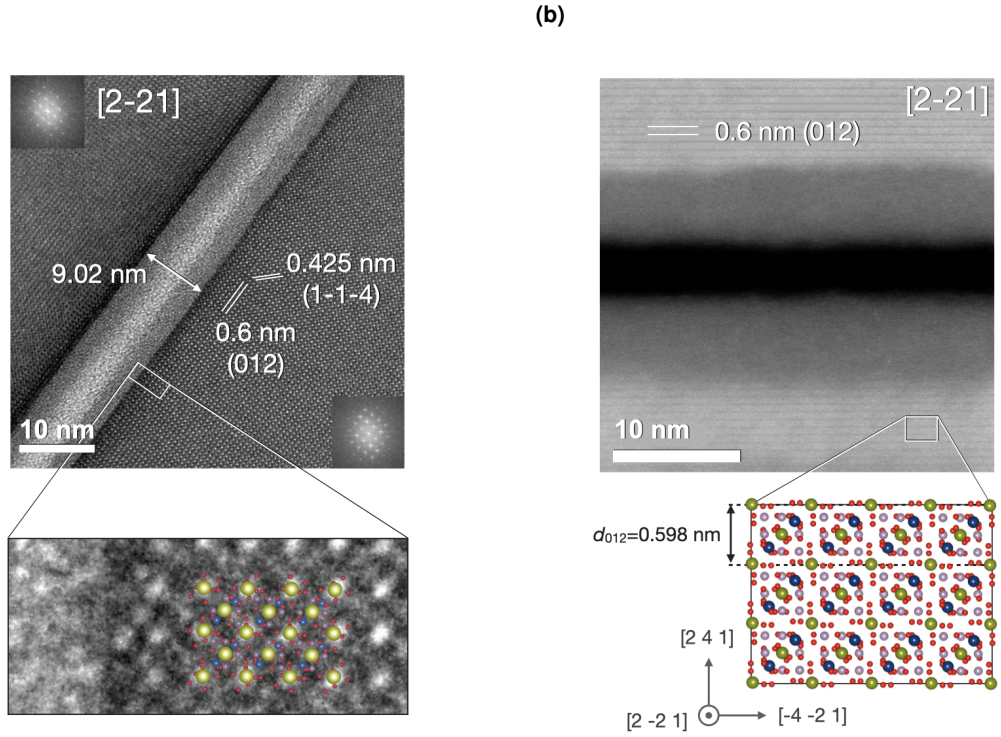

Figure 4.2: Experimental TEM images of LATP grain boundary. Elemental colors of atomistic structures are chosen as Li ●, Ti ●, O ●, and P ●. **(a)** HRTEM image of LATP grain with partially wetted amorphous grain boundary. Close-up of the grain boundary aligned with crystal structure (ICSD:253240). The pseudocubic arrangement of brighter reflexes can be attributed to interference at Lithium positions. **(b)** HRSTEM-HAADF signal of the same grain boundary in $[0\,2\,-1]$ orientation is in line with respective planes and distances in the crystal structure. Images adapted from Stegmaier et al. [1] under CC BY 4.0.

A pronounced intensity profile across the grain boundary allows for the identification of three distinct structural domains. These are crystalline grains to both sides of the boundary, interfaced by thin and darker semi-amorphous rims toward a brighter amorphous region in the grain boundary center. The grains are oriented in $[2\,-2\,1]_{\mathrm{hex}}$ zone axis and the symmetric bright reflexes can be ascribed to a $[1\,0\,0]_{\mathrm{pc}}$ pseudocubic sublattice of Li positions, cf. close-

[4.3] TEM measurements were conducted by Dr. R. Schierholz, Institute of Energy and Climate Research Fundamental Electrochemistry (IEK-9), Forschungszentrum Jülich. Details on TEM sample preparation and imaging specifications are given in Ref. [1].

up in Figure 4.2 (a). These reflexes are not directly caused by scattering of the highly mobile Li ions, but are formed from constructive interference of electron waves scattered off neighboring transition metal centers.

The relative grain orientation toward the interface is most likely terminated by $(0\,1\,2)_{\mathrm{hex}}$-planes. In Figure 4.2 (b), the plane distance of $d_{012} = 0.6$ nm found in an High-Angle Annular Dark Field (HAADF) HR-STEM image coincides with the distance from the corresponding crystal structure $d_{012} = 0.598$ nm. Due to severe beam damage, however, an exact assignment of the grain terminating domain from experimental TEM images is not possible. Brighter contrast in the amorphous grain boundary center may be attributed to a lower relative density of the amorphous phase as compared to crystalline LATP [132]. This effect is potentially masked by a reduced sample thickness introduced during sample preparation. The dark contrast in Figure 4.2 (b) supports such a thickness effect. Similar observations have been made for amorphous Li_3PO_4 and $AlPO_4$ in triple points between grains [96, 165]. Explicit TEM simulations are performed in Section 4.4.3 to scrutinize a possible thickness effect on TEM image contrast.

The observed variation of the grain boundary widths, i.e. the amorphous domain, may be ascribed to wetting by a secondary phase. The formation of secondary phases, such as $AlPO_4$ and Li_3PO_4, has been reported previously for LATP [96, 165]. Especially $AlPO_4$ is known to impede ion diffusion pathways and hence reduce the overall Li ion conductivity [129, 132, 228]. Energy Dispersive X-ray Spectroscopy (EDS) analyses [1], as well as Atom Probe Tomography (APT) studies, see Section 4.2.3, however, do not support the presence of these secondary phases, as they only show slight variations of stoichiometric Al content. For the atomistic modeling of a LATP grain boundary, the existence of secondary phases is thus neglected.

4.2.3 Atom Probe Tomography[4.4]

Complementing the structural information obtained from TEM, APT is able to provide chemical information and resolve elemental profiles at the nanoscale. The measurements conducted in Ref. [1] pioneer in applying APT methods to Li conducting solid-state electrolytes.

Figure 4.3 (a) shows a Scanning Electron Microscope (SEM) image of a needle-shaped LATP specimen for APT measurements. The brighter contrasted streak reveals the position of a grain boundary at the specimen surface. A corresponding 3D atom map of Li is shown in Figure 4.3 (b). Here, the high contrast of accumulated Mg^{2+} impurity is exploited to visualize the grain boundary.

Averaging over the indicated rectangle yields the spatially-resolved elemental concentration profiles across the grain boundary presented in Figure 4.3 (c). The Ti profile exhibits a local depletion by about 1.5 atom percent (at%) at the grain boundary, which is predominantly at

[4.4] APT measurements were conducted by Dr. I. Povstugar, Central Institute for Engineering, Electronics and Analytics (ZEA-3), Forschungszentrum Jülich. Details on specimen preparation, APT measurements and image post-processing are given in Ref. [1].

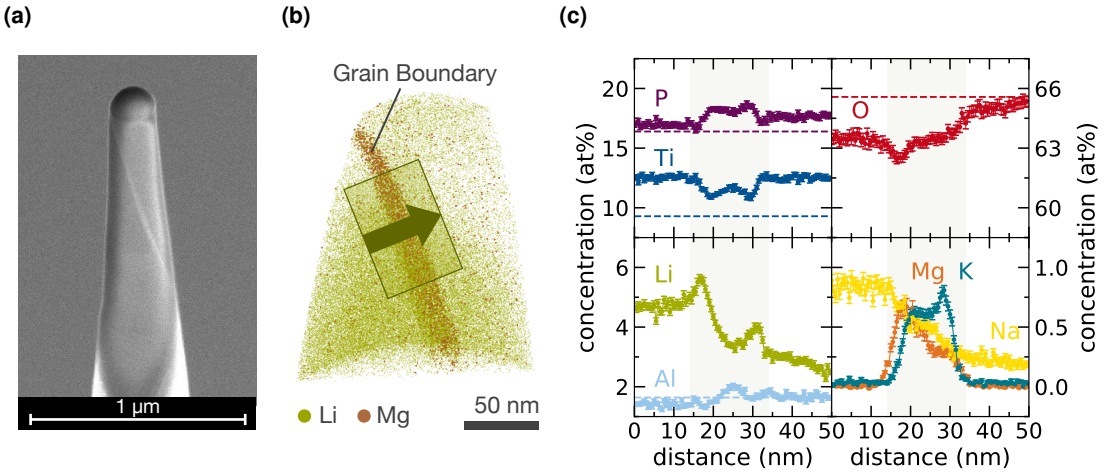

Figure 4.3: Atom Probe Tomography measurements. **(a)** Pt deposited APT needle with LATP specimen featuring a grain boundary. **(b)** Reconstructed atom map clearly showing the grain boundary by exploiting the high contrast of accumulated Mg impurities. **(c)** Corresponding atom profiles for each element across the grain boundary □ (the overlayed rectangle in panel (b) indicates the selected subvolume used for averaging, with the arrow indicating the direction used for positive distances) from APT experiment. Nominal LATP elemental concentrations are indicated by respective dashed lines. Images adapted from Stegmaier et al. [1] under CC BY 4.0.

the expense of P. An observed lower oxygen profile from the nominal LATP stoichiometry by a few at.% is a known artifact in APT [229–231]. This is due to the field evaporation of neutral species and a post-dissociation of oxygen-containing complex ions, which are identified in the corresponding mass spectra, cf. Ref. [1]. For the atomistic modeling of chemical composition, the oxygen distribution does not rely on APT data, but is based on structural TEM information and force field based simulation.

In Figure 4.3 (c), the Li concentration profile shows significant asymmetry between the adjacent grains. This could point toward an inhomogeneity of the synthesized LATP material. Moreover, the absolute Li concentration may not be directly retrievable from APT. The inherently low evaporation field [229], as well as the high mobility under electric fields, may lead to a bias in Li distribution. Since the averaging of atom maps is performed virtually normal to the electric field lines however, the relative Li distribution across the interface is reliable. A characteristic feature of Li distribution is a local enrichment to both sides of the grain boundary, which agrees with an observed aforementioned Ti-depletion.

Apart from the stoichiometric LATP elements, other cationic impurities are detected by APT. The Na^+, Mg^{2+}, and K^+ local concentrations never exceed 1 at.%, cf. Figure 4.3 (c). Assuming a brick-layer model with experimental grain edge size and grain boundary widths [47], the absolute number of impurity ions lies within the order of 30 – 150 ppm. Due to these low concentrations, possible implications on the electrolyte properties are neglected. Effects on

microscopic properties, such as lattice distortion, vacancy introduction etc., is specific to the impurity itself and a generalization is not straight forward. In Chapter 5, advantages of local interfacial doping with higher concentrations of divalent Mg^{2+} are scrutinized.

4.3 Computational Details

The LAMMPS software package [209] is employed for all MD Simulations performed in this work. For short-range interactions, a cutoff of 9 Å is chosen and 3D Periodic Boundary Conditions (PBC) are applied. The long-range interactions are handled using a PPPM solver [193]. Following the adiabatic core-shell model, cf. Section 3.3.2, a small timestep of 0.2 fs is chosen to capture high frequency core-shell vibrations. Thermostatting in the canonical NVT ensemble is achieved via a Nose-Hoover thermostat, as implemented in the LAMMPS software [232]. Analogously, simulations in the isothermal-isobaric NPT ensemble are performed using a Nose-Hoover barostat. Relaxation times are adopted as $T_{\mathrm{damp}} = 10^2 \Delta t$ and $p_{\mathrm{damp}} = 10^3 \Delta t$, respectively.

4.3.1 Core-Shell Force Field Parameterization[4.5]

The force field employed for all MD simulations is parameterized specifically for the LATP $Li_{1.3}Al_{0.3}Ti_{1.7}(PO_4)_3$ material to reproduce its key structural and dynamic properties. As a basis, the force field for the structurally similar $Li_4Ti_5O_{12}$ [233] is used. Building on this, additional intermediate potentials are parameterized in a multi-step fashion by including structure sets of $LiTi_2(PO_4)_3$, $AlPO_4$, $LiTiPO_5$ and LATP. This parameterization scheme promises a high transferability of the resulting force field. A total of 247 atomistic bulk structures are constructed and random displacement of individual atomic positions, drawn from a normal distribution with standard deviation of 0.2 Å, is applied.

Particle interactions are described via a Buckingham potential and the ions are assigned partial charges. A core-shell model is used for the oxygen anion to account for polarization of the poly-ionic phosphate tetrahedra. Parameters of effective mass, partial charges and the harmonic spring constant for the core-shell system are adopted from Ref. [234].

The fitting procedure for the interaction parameters is performed using the General Utility Lattice Program (GULP) [205]. Herein, energy matching of atomistic structures with first-principle based DFT reference data is conducted. Additional force matching is considered at a manual level. The FHI-aims code [235] with the PBE exchange-correlation functional [185] is used for DFT reference calculations. An all-electron description in the *tight tier2* basis is chosen, which employs a $(4 \times 4 \times 2)$ Monkhorst-Pack [236] k-point grid. With these computational settings, densities of the k-point grid consistently exceeded 41469 k-points Å^3 with a maximum k-point grid spacing of 0.034 Å^{-1}. Convergence of relative energies is found within $5.56 \cdot 10^{-3}$ meV atom^{-1}. Resulting LATP force field parameters are listed in Table A.1.

[4.5] Force Field parameterization was performed by Dr. S. Rostami, Chair of Theoretical Chemistry and Catalysis Research Center, Technical University of Munich.

4.3.2 Core-Shell Force Field Validation

Correlation of both, structure energies and atomic forces, from force field calculations and DFT reference data is shown in Figure 4.4 (a). While the energy correlation shows a systematic force field overestimation for higher energies, the force correlation does not reproduce this behavior. A separation of force contributions by elemental species is illustrated in Figure 4.4 (b). Generally, the correlation is satisfactory considering the high dimensionality of the force field and its classical analytical character.

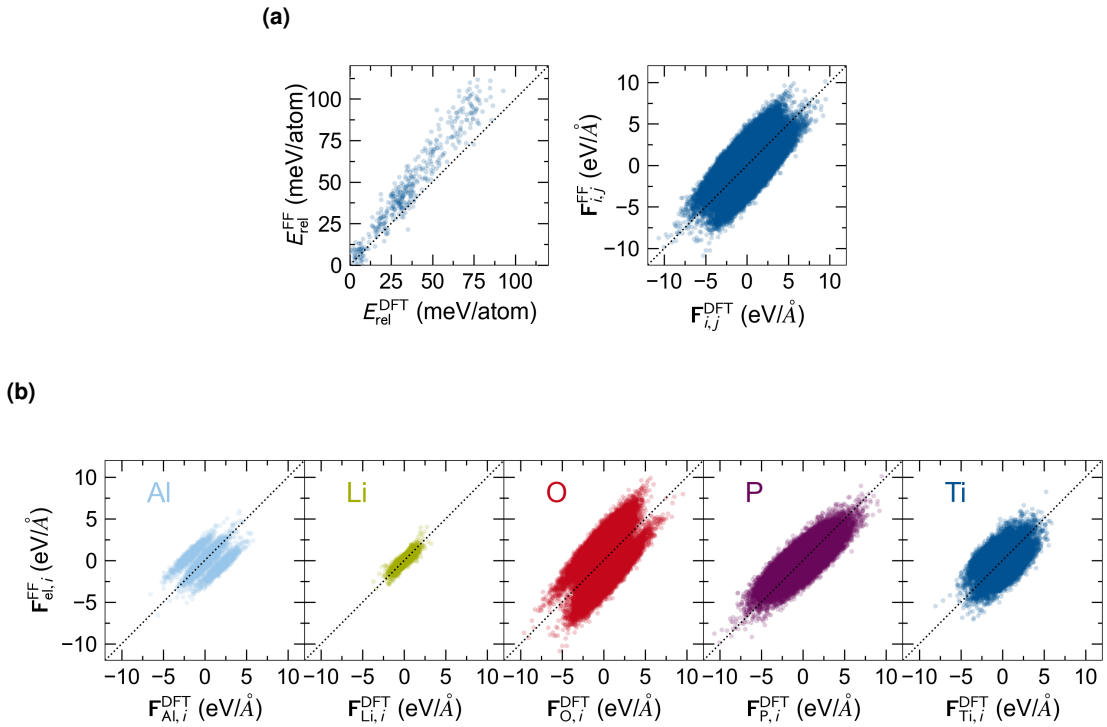

Figure 4.4: Energy and force correlation of LATP structures computed with parameterized force field and reference DFT data. **(a)** Correlation between energy and force of randomly displaced atoms in different LATP configurations. **(b)** Atomistically resolved force correlation for each element in the corresponding LATP configurations. Images adapted from Stegmaier et al. [1] under CC BY 4.0.

A key characteristic of the LATP material is an inherent anisotropic behavior along the c-crystalline axis [132]. To further validate the obtained core-shell force field, this anisotropy is first screened in a Birch-Murnaghan like graph shown in Figure 4.5 (a). Here, the relative change in energy is monitored upon changes of the lattice constants. $\Delta(a, b)$, which are varied collectively, and Δc are varied between -2.5 % and 5 % of the original lattice constants. The core-shell force field is able to capture the anisotropic behavior and reproduces the DFT reference lowest energy lattice constants.

Experimentally, the anisotropic behavior of LATP has been shown from asymmetric lattice expansion when measuring the thermal expansion coefficient [132]. Figure 4.5 (b) depicts

the change in lattice constants $L_{a,b}$ and L_c, when the LATP system is heated up. To obtain these values, NpT MD simulations at different temperatures are conducted. The systems are equilibrated for 20 ps to reach convergence and the following 40 ps trajectory is used as the production run. To account for stochastic effects from realizing fully occupied LATP structures, 10 bulk configurations containing 110 atoms are simulated at each temperature. Respective errors are taken from the standard deviation of these structural ensembles. Despite a small systematic offset, the LATP core-shell force field reproduces the extended thermal expansion along the c-axis and shows negligible variation along a and b-axes.

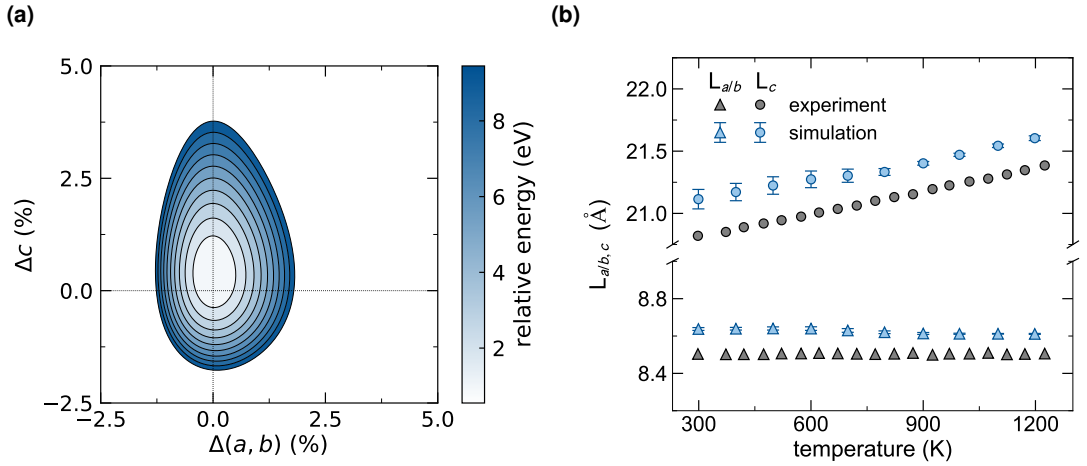

Figure 4.5: Anisotropic behavior of LATP. **(a)** Relative energy changes of an LATP bulk unit cell upon variation of lattice parameters $\Delta(a, b)$ (altered collectively) and Δc, as obtained from the core-shell force field. The intersection of the dashed lines corresponds to the energetic minimum structure obtained by DFT. **(b)** Lattice constant expansion upon heating for the core-shell force field from short NpT simulations as compared to experiment [132]. Error bars are computed from standard deviations of ten LATP structures for each point. Images adapted from Stegmaier et al. [1] under CC BY 4.0.

To further validate the dynamic behavior of the underlying core-shell force field, Figure 4.6 (a) shows element specific MSDs from NVT simulations conducted at 600 K and Figure 4.6 (b) depicts a respective Arrhenius plot of Li ion conductivities at different temperatures. From the force field MSDs, elements of the rigid host, i.e. O, Al, Ti, and P, are virtually immobile as compared to the Li ions. This accurately reproduces the expected behavior for ion mobility in a Li conducting SSE. The computed Li ion conductivities over a temperature range between 300 – 1200 K shows a slight overestimation of the activation energy with $E_{\mathrm{a,core-shell}} = 243$ meV, which can be retrieved from the slope in the Arrhenius formalism. However, experimental values [47] are measured at low temperatures and a linear extrapolation across such an extended temperature range may be subject to errors. The parameterized core-shell force field is able to reproduce key features of the LATP material, such as anisotropic behavior and ion dynamics.

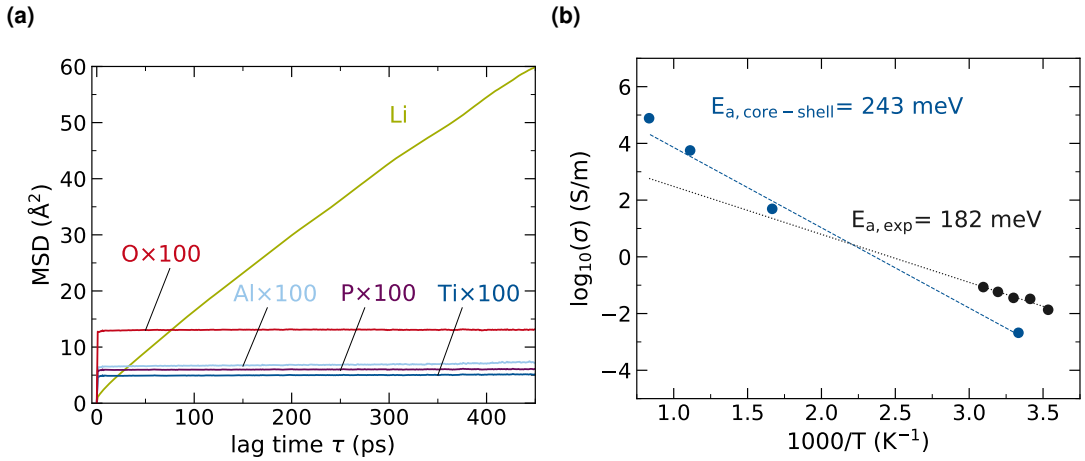

Figure 4.6: Ion dynamic validation of LATP force field. **(a)** MSD of different ion species at 600 K from NVT simulations conducted with core-shell force field. Immobile ion species O, Al, Ti, and P are magnified by a factor 100 to visualize their convergence. **(b)** Arrhenius plot of Li ion conductivities as determined from MD simulations at different temperatures and corresponding bulk LATP experimental values [47].

4.4 Atomistic Grain Boundary Model

As evidenced by TEM and APT findings, grain boundaries in LATP exhibit a complex and multi-phase structure. The modeling of sharp interfaces via coinciding lattices, see Section 2.3.3, is thus not suitable in this case, but a more elaborate scheme is needed. A novel approach introduced herein, explicitly features slabs of two structurally different phases, which are motivated from experimental findings. A computational sintering protocol is employed to fuse these slabs to a target density. By design, the resulting atomistic model in Figure 4.7 is comprised of these crystalline and amorphous bulk phases. The most striking feature, which has not entered the construction of the model, is the formation of nanometer sized complexions to both sides of the grain boundary.

A key characteristic of these complexions is the gradual loss of structure going from the crystalline grain to the fully amorphous interphase in the center of the boundary, cf. phosphate cuts displayed in Figure 4.7. The quantifiable structural differentiation from adjacent bulk phases and an observed thermodynamically self-limited thickness qualifies these regions as actual complexions [44].

Following elemental profiles across the grain boundary from APT measurements, these complexions feature a Ti depletion at the crystalline grain interface. An energetically favorable segregation of Al and Ti at the grain surface is crucial for the observed local separation of charge carriers and thus the dendrite suppression capabilities of LATP.

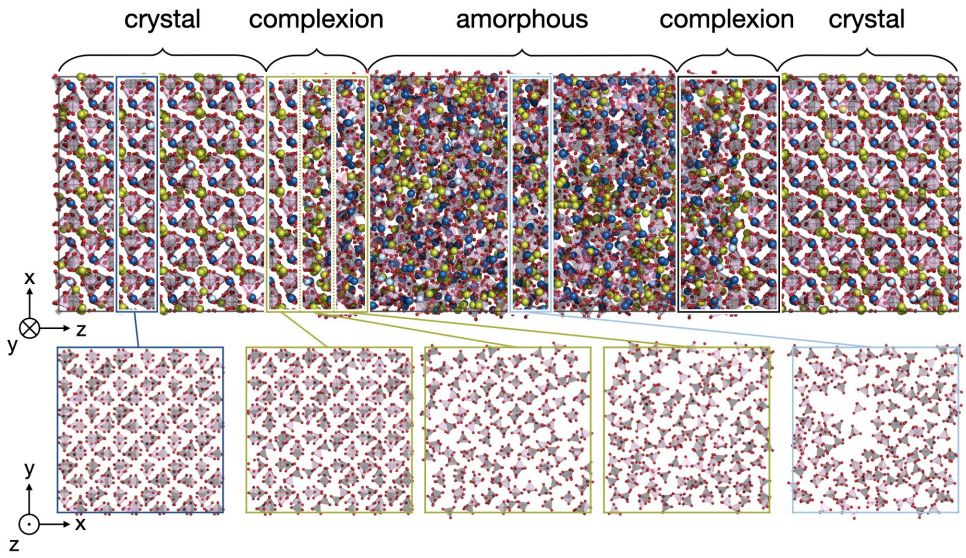

Figure 4.7: Atomistic model of the grain boundary. The crystalline grains, the amorphous interphase, and the semi-amorphous complexions at the grain surfaces are shown. Elemental colors are chosen as Li ●, Al ●, Ti ●, O ●, and P ●. The gradual loss of structure across the grain boundary is illustrated by five close-ups displaying LATP phosphate units. Image adapted from Stegmaier et al. [1] under CC BY 4.0.

4.4.1 Construction of Two Slab Model

In a first step, a crystalline LATP slab is cut to reproduce the orientation from experimental TEM results. In order to obtain an orthogonal slab, the original LATP ICSD unit cell is extended and cut into a $(1 \times 1 \times 2)$ supercell with the three real-space box vectors $\vec{x} = [2\ -2\ 1]$, $\vec{y} = [2\ 4\ 1]$ and $\vec{z} = [-4\ -2\ 1]$, as shown in Figure 4.8 (a). The first vector is dictated by the observed $[2\ -2\ 1]$ zone-axis direction of the TEM image, cf. Figure 4.2, and the characteristic Li cubic sub-lattice is aligned in $(0\ 1\ 2)_{\mathrm{hex}}$ relative to the grain boundary. Partially occupied Ti/Al and Li sites in the crystal structure are sampled to full occupancy to reproduce the $Li_{1.3}Al_{0.3}Ti_{1.7}(PO_4)_3$ stoichiometry. Though this sampling is a stochastic process, a single realization for Li occupation suffices, as these ions are highly mobile in LATP. Al-Al distances do not show a significant energetic effect, which similarly justifies a single realization of Aluminum sampling, cf. Ref. [1].

To avoid inducing a dipole in the truncated slab, the terminating Ti/Al layers toward vacuum are sampled to half occupancy on both sides. An anti-symmetric configuration is chosen for the two opposite planes, which yields a total of $\binom{n_{\mathrm{atoms}}}{n_{\mathrm{sites}}} = \binom{18}{36} = 9.075{\cdot}10^9$ possible combinations. Single point energies for 500 randomly chosen realizations are shown in Figure 4.8 (b) (left). The energetically most favorable configuration from electrostatic considerations is a maximum spreading of ions on the site grid. Ten equidistant structures of the lowest 100 configurations have been chosen to screen for energetic preference of Al^{3+} versus Ti^{4+} ter-

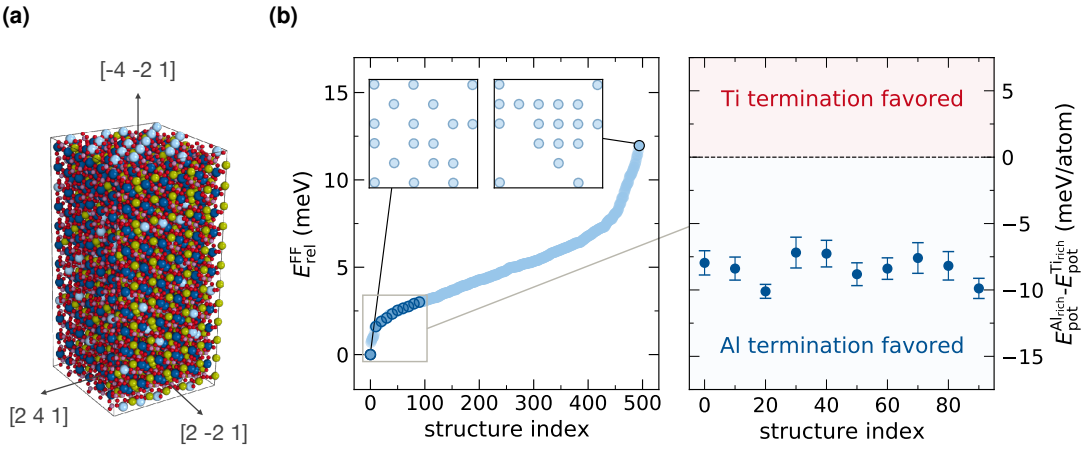

Figure 4.8: Crystalline LATP slab construction. **(a)** Atomistic structure of truncated LATP slab with $(0\,1\,2)$, $(1\,-1\,2)$ and $(1\,0\,-2)$ planes and real space vectors $[2\,-2\,1]$, $[2\,4\,1]$ and $[-4\,-2\,1]$. Elemental colors are chosen as Li ●, Al ●, Ti ●, O ●, and P ●. **(b)** Single point energies of 500 randomly chosen surface terminations. Energetic difference between ten relaxed structures at 300 K of the two different surface terminations Al-rich versus Ti-rich. Images adapted from Stegmaier et al. [1] under CC BY 4.0.

mination. A 1 nm vacuum slab is introduced between terminating planes and the truncated grain slab is extended through PBC.

In Figure 4.8 (b) (right), the energetic difference for each corresponding Al-rich and Ti-rich termination is computed from 100 ps MD simulations at 300 K. For all surface realizations, a consistent energetic preference for Al-termination is shown. Therefore, the lowest energy rank Al-terminated configuration is chosen as basis for the grain boundary model.

To model the amorphous domain, information about chemical composition is employed from experimental APT measurements. The interface model is constructed to model a representative for the ensemble composition of stoichiometric LATP. Therefore, the experimentally observed elemental profiles are shifted to fit nominal values for the LATP crystalline grain. This allows for comparison of macroscopic properties, such as ion conductivities, to experiment. Since the atomistic model is extended through PBC, the elemental profiles are further mirrored at the center of the grain boundary to yield Figure 4.9 (a). The adjusted profiles of Al, Ti, Li and P are translated into an absolute number of ions for the amorphous phase. The oxygen distribution strictly follows the P profile, as only tetrahedral phosphate units are considered. While the so enforced local charge neutrality compensates the lack of an exact oxygen profile from APT, the excess amount of phosphorous from APT cannot be met.

A regular 3D host grid with 5.2 Å spacing in vacuum is introduced between the terminating planes. A surplus of grid points is deliberately chosen, to allow for more flexibility when stochastically sampling the LATP building blocks, i.e. phosphates, Ti, Al and Li, onto the grid. Phosphate polyhedra are considered as fixed units and randomly rotated before sampling.

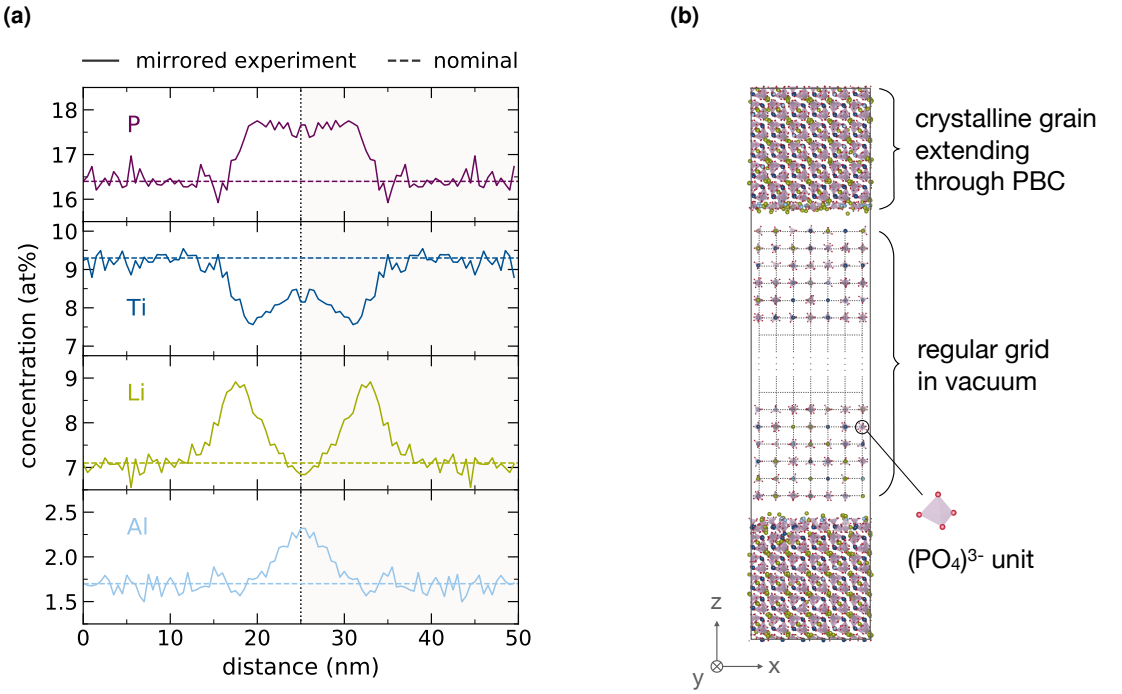

Figure 4.9: Chemical composition and modeling of amorphous bulk phase. **(a)** Adjusted elemental profiles from APT experiment mirrored in the grain boundary center and shifted to nominal bulk composition. **(b)** Exemplary structure of the initial stochastically sampled amorphous phase onto a regular grid in vacuum. Elemental colors are chosen as Li ●, Al ●, Ti ●, O ●, and P ●. Phosphate tetrahedra are considered as fixed units. Images adapted from Stegmaier et al. [1] under CC BY 4.0.

The stochastic nature of this sampling protocol required multiple realizations to obtain a representative structural ensemble. A schematic realization is shown in Figure 4.9 (b).

While the large grid spacing avoids overlap of atoms, the obtained sparsely occupied vacuum slab does not represent a physical system. Therefore, the amorphous phase is compressed iteratively following the scheme shown in Figure 4.10 (a). First, the z-coordinate of atoms in the vacuum slab are rescaled by a factor of 0.99. This results in an unoccupied region between atoms in vacuum and the adjacent crystalline grain. Second, the crystal domain on top is collapsed by this unoccupied space. Geometry optimization in a third step allows for relaxation of the atoms from the regular grid and avoids unfavorable close contacts, which may have been introduced by the rigid compression. These steps render one iteration to compress the overall structure into a more realistic system.

Energetic stabilization of five such atomistic models upon iterative compression is shown in Figure 4.10 (b). An initially low density from the sparse model is compressed to $\rho = 2.5\ \mathrm{g\,cm^{-3}}$.

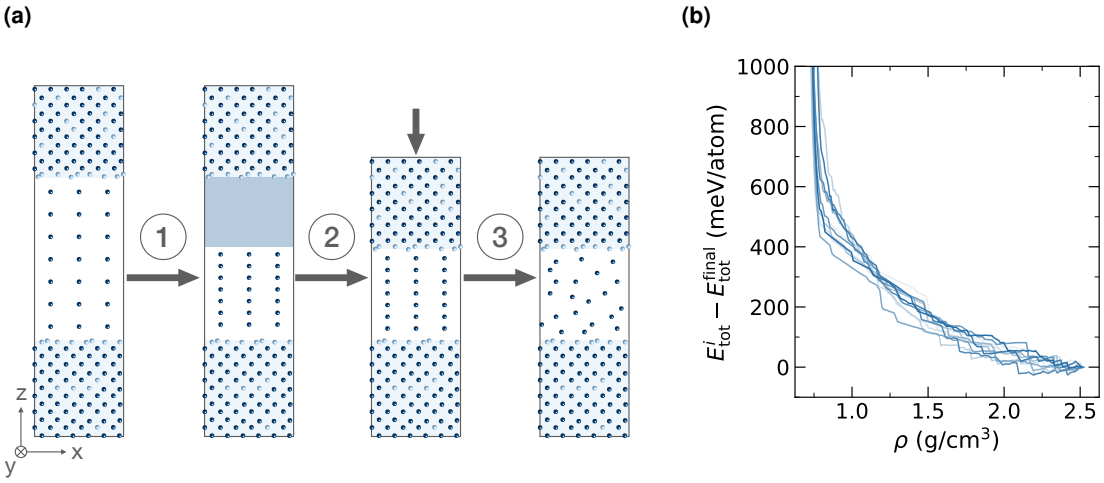

Figure 4.10: Compression of sparse grain boundary model. **(a)** Schematic of iterative process to compress the vacuum slab. ① rescaling of z-coordinate, ② collapsing of structure by unoccupied region and ③ geometric optimization to allow for structural relaxation. **(b)** Energetic stabilization of stochastically sampled grain boundary structures upon vacuum compression. Image (b) adapted from Stegmaier et al. [1] under CC BY 4.0.

The resulting atomistic structures enter a computational sintering protocol to further relax into more favorable configurations and meet experimentally reported relative densities.

4.4.2 Computational Sintering Protocol

The relatively short geometry optimization in the iterative compression scheme to eliminate vacuum does not sufficiently ensure full structural minimization and the elimination of an artificial long-range structure introduced by the regular host grid. A computational sintering protocol is established, closely following the experimental procedure [96]. A schematic of the sintering protocol employed in experiment is shown in Figure 4.11 (a). An initial densification in the computational setup is achieved by rescaling and simultaneous step-wise heating of the system. A subsequent *melting*, i.e. MD simulations at elevated temperatures, and quenching step yield an atomistic structure which is relaxed in NpT to obtain the final grain boundary model.

The target density entering the compression step as well as the maximum sintering temperature and melting simulation time are not known *a priori* and are investigated in a Design Of Experiment (DOE) ansatz. In the compression phase, MD simulations are conducted in NVT for 20 ps at each iteration to allow for relaxation into more favorable structures. This one dimensional compression in z-direction corresponds to the uni-axial pressing in experiment. The maximum sintering temperature employed in experiment is 1100 °C, which is maintained for eight hours [96]. These time scales exceed the computational power and necessitate a shorter melting step at elevated temperatures. Quenching the system to ambient temperatures is achieved via step-wise NVT simulations with sufficient dwelling times.

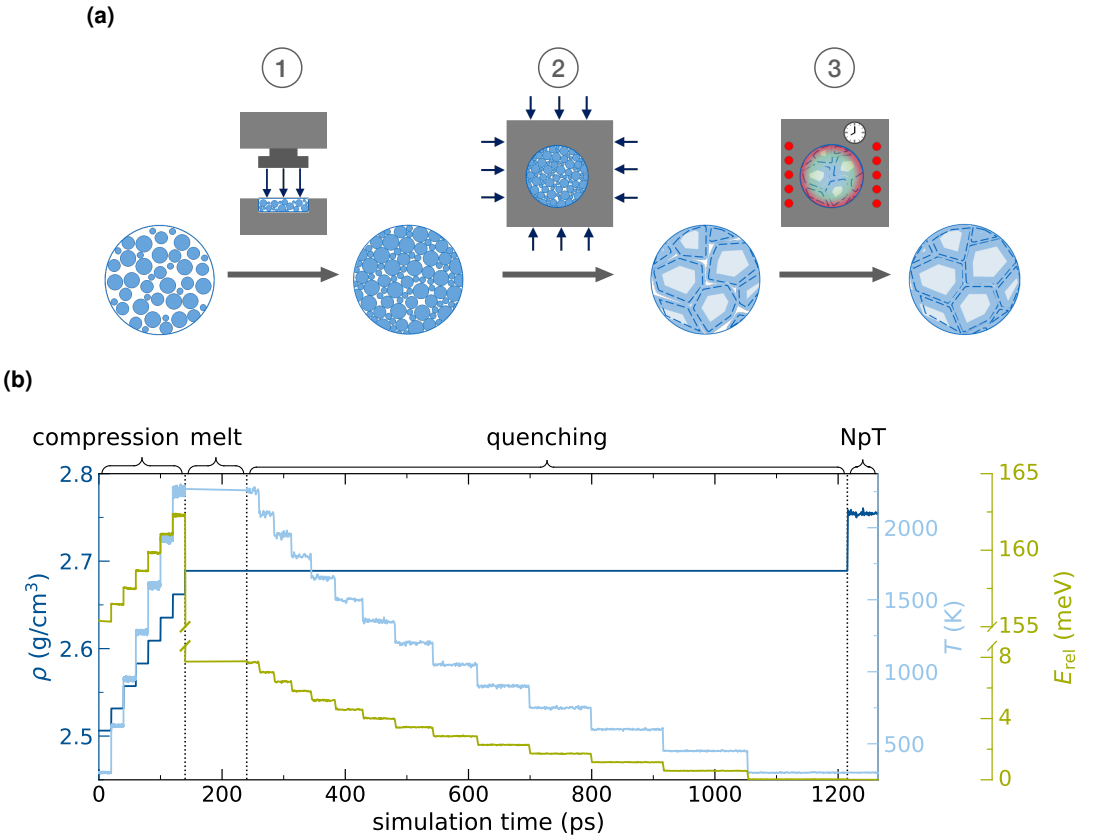

Figure 4.11: Sintering of LATP powder. **(a)** Schematic experimental sintering procedure. ① Uniaxial die pressing of powder precursors, ② cold isostatic pressing and ③ sintering at high temperatures for several hours [96]. **(b)** Computational sintering profile for mass density, temperature, and relative energy change. Image (b) adapted from Stegmaier et al. [1] under CC BY 4.0.

Due to slower relaxation at lower temperature, dwelling times are extended exponentially with a quenching rate of $2\,\mathrm{K\,ps^{-1}}$. In a final step, the system is relaxed in NpT to fully relax the system at ambient atmosphere. The three properties of mass density, temperature and system energy along the computational sintering profile are shown in Figure 4.11 (b).

To identify the effect of sintering parameters on the final density after equilibration ρ_{npt} and the relative energy gain, a fullfactorial DoE analysis is conducted. A target final density can be estimated from reported 94 % relative amorphous density as compare to the LATP crystal bulk [132]. This yields a density of $\rho_{\mathrm{npt}} = 0.94 \cdot 2.81\ \mathrm{g\,cm^{-3}} = 2.641\ \mathrm{g\,cm^{-3}}$. The target energy is to be minimized. The three parameters, i.e. factors, are the density after compression ρ_{comp}, the maximum sintering temperature T_{max} and the equilibration time t_{equil} for the melting step. For each factor, a lower and upper limit, i.e. level, is screened. For the compression density, the lower limit is chosen as the target density $\rho_{\mathrm{comp},-} = 2.641\ \mathrm{g\,cm^{-3}}$ and the upper limit is chosen as 110 % of this final density. The effect of sintering temperature

is tested between $T_{\mathrm{max},-} = 1500\,\mathrm{K}$ and $T_{\mathrm{max},+} = 2250\,\mathrm{K}$. The lower limit is the experimental sintering temperature and the upper limit temperature is chosen above which LATP grains start to actually melt and lose integrity. By design the amorphous composition may not required an additional melting step. The limits for the melting time are therefore chosen as $t_{\mathrm{equil},-} = 0\,\mathrm{ps}$ and $t_{\mathrm{equil},+} = 100\,\mathrm{ps}$. The factors of interest and their respective levels are listed in Table 4.1. The fullfactorial design plan is provided in Table B.1.

Table 4.1: DoE factors and levels to screen effects on system energy and hit a target experimental density from the computational sintering protocol.

Factor	**Level**	
	$-$	$+$
ρ_{comp}	2.641 g cm^{-3}	2.904 g cm^{-3}
T_{max}	1500 K	2250 K
t_{equil}	0 ps	100 ps

The sensitivity analysis shown in Figure 4.12 (a) reveals the final density ρ_{npt} to be merely affected by the target density in the compression step ρ_{comp}. The other two factors of maximum temperature and melting simulation time show virtually no effect on this observable. Since both, lower and upper limit of the compression density, lead to an increase in final density, a sparse sweep at lower values of ρ_{comp} is conducted. A suitable compression density of 2.54 g cm^{-3} is identified, see Ref. [1].

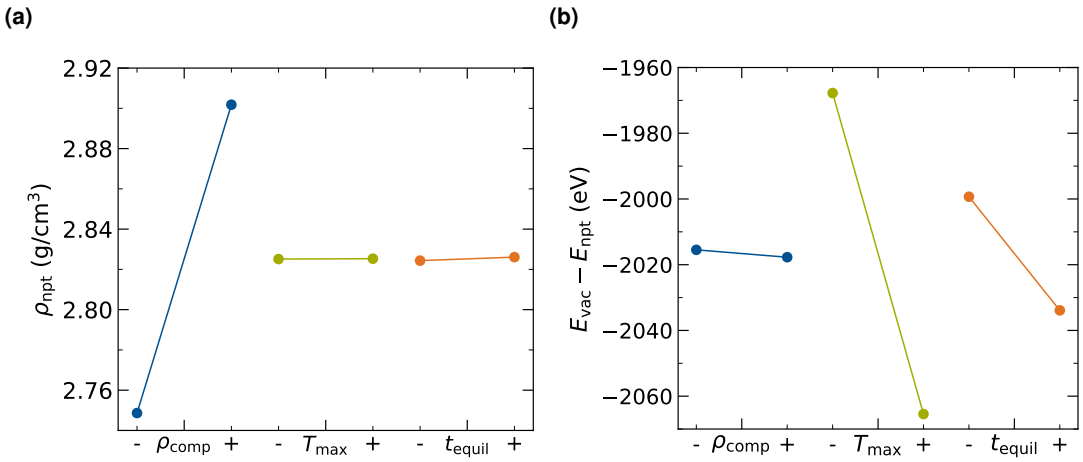

Figure 4.12: Sensitivity analysis of three factors and two respective levels of the computational sintering protocol for **(a)** final density ρ_{npt} and **(b)** relative system energy. Images adapted from Stegmaier et al. [1] under CC BY 4.0.

The corresponding sensitivity analysis for system energy is shown in Figure 4.12 (b). The dominant lever for energy minimization is the maximum temperature $T_{\mathrm{max},+} = 2250\,\mathrm{K}$. The

sensitivity analysis further supports the need for a melting step in the sintering protocol, as system energy decreases with $t_{\mathrm{equil},+}$. Since energy convergence is achieved after 50 ps, this shorter simulation time is chosen.

The established protocol is generally transferable to other ceramic grain-grain interphases. Exact simulation parameters, however, need to be reevaluated for each individual case.

4.4.3 Structural Characterization of Interface

Density and Chemical Composition

While for the sintering protocol the total mass density of the system is considered, a spatial resolution of the density across the different domains is shown in Figure 4.13 (a). To account for stochastic effects, the density is averaged over five sampled grain boundary configurations after sintering. In the crystalline domain, the density exhibits an oscillation across the distinct planes of the underlying orientation. A reference density of 2.84 g cm^{-3} is maintained locally for the crystal during sintering. The grain boundary area shows a decreased density of 2.49 g cm^{-3} and larger deviation between the different configurations.

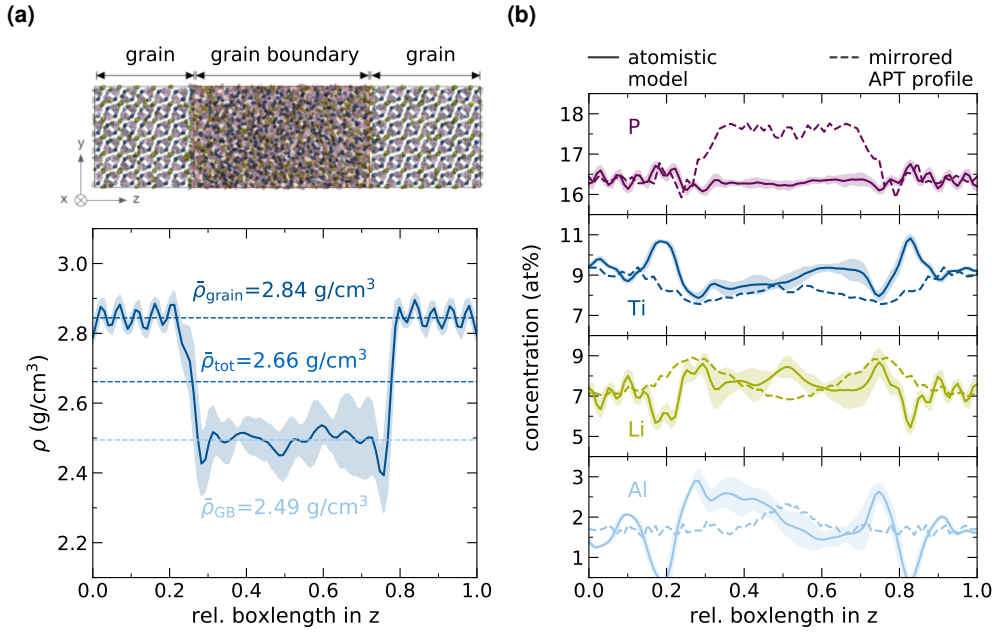

Figure 4.13: Density and chemical composition of final grain boundary structures. **(a)** Spatially resolved mass density profile across the grain boundary. **(b)** Elemental profiles across the grain boundary and corresponding experimental profiles (dashed lines). Images adapted from Stegmaier et al. [1] under CC BY 4.0.

Elemental profiles for P, Ti, Li, and Al across the grain boundary are shown in Figure 4.13 (b). The corresponding mirrored and shifted experimental profiles are indicated by respective

dashed lines. Analogously to the density, the atomistic distribution is averaged over five atomistic models to account for the stochastic nature. The largest deviation from APT is observed for P, which can be attributed to the limited flexibility since phosphates are taken as fixed units. Due to charge neutrality restrictions, the phosphate profile is thus governed by all other cations. The deliberate complete segregation of Al and Ti at the complexion interface leads to enhanced Al peaks at the intersection between grain and grain boundary and Al depletion in sub-surface grain layers. The Ti profile exhibits the respective opposite behavior. Though Li ions are initially stochastically sampled into the amorphous grain boundary, there is a local enrichment close to the interface on both sides of the grain boundary. This is also characteristic in the Li profiles retrieved from APT measurements, cf. Figure 4.3 (c).

TEM Simulations[4.6]

TEM images of the obtained grain boundary models are simulated using the Dr. Probe Software [218] to compare the key structural characteristics with experimental TEM findings. Simulation parameters are adopted from the FEI Tecnai microscope used for imaging [237] and a list of the parameters is provided in Table C.1. A Modulation Transfer Function (MTF) for the detector is used, as measured by the knife edge method [238]. Aligning the resulting simulated HRTEM image with a respective close-up of the experimental image, see Figure 4.14, both crystalline and amorphous region are reproduced as well as the darker thin regions attributed to the complexions.

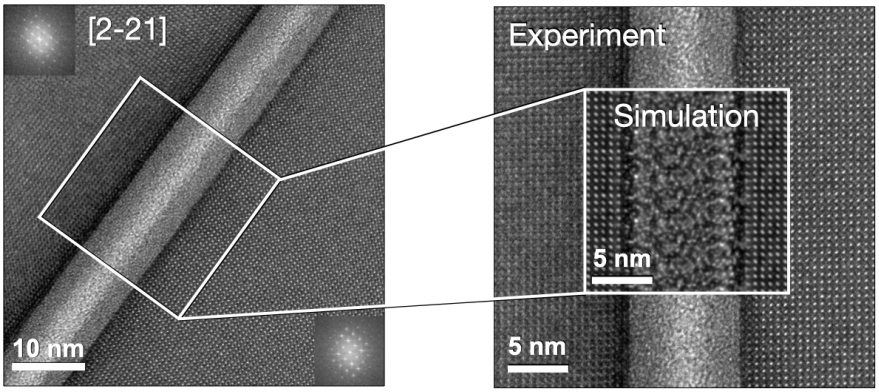

Figure 4.14: Alignment of experimental and simulated TEM image. Close-up of the grain boundary as obtained from experimental TEM aligned with a simulated TEM image of the atomistic model. Image adapted from Stegmaier et al. [1] under CC BY 4.0.

In order to resolve the TEM contrast from simulation, the dominant lens aberrations, i.e. defocus and spherical aberration, need to be determined. A Scherzer-focus of $z_{\mathrm{Scherzer}} = 63.3\,\mathrm{nm}$ is applied in all simulations, which is calculated from Equation (3.30) with the electron

[4.6] Dr. J. barthel, Ernst Ruska-Centre for Microscopy and Spectroscopy with Electrons (ER-C 2), Forschungszentrum Jülich, has provided parameters and advised in TEM simulations.

wavelength $\lambda = 2.508\,\text{pm}$ of an employed 200 keV laser beam. The spherical aberration $C_s = 1.2\,\text{mm}$ is taken from the microscope specifications, cf. Table C.1.

The system thickness in beam direction, i.e. the x-axis, is screened in ≈5 nm steps up to a thickness of ≈100 nm as shown in Figure 4.15. At a thickness of ≈49 nm the reflexes from the Li sub-lattice best reproduce the experimental pattern. Thermal diffusive scattering is accounted for by introducing isotropic Debye-Waller factors B_{iso}, according to Equation (3.35), for each atom. The factors are calculated from the MSD of a 1 ns MD trajectory at 300 K. Domain resolved averaged of the element specific B_{iso} values are listed in Table C.2. Ions in the amorphous bulk are generally more mobile than in the crystalline grain.

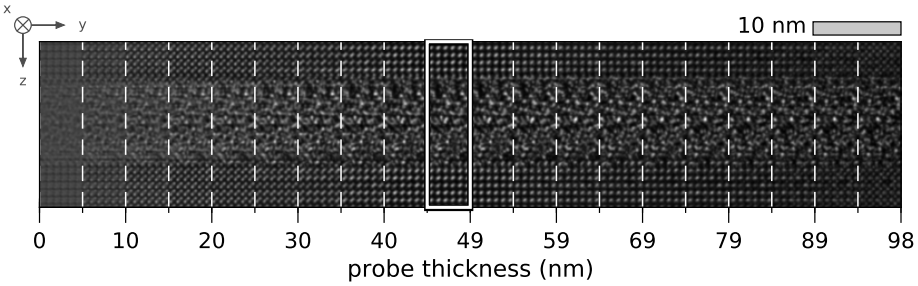

Figure 4.15: Thickness map of a simulated TEM image at a focus of 63.3 nm. Image adapted from Stegmaier et al. [1] under CC BY 4.0.

For sample thicknesses of ≈50 nm, the dominant contribution to the image contrast can be attributed to elastic scattering. Energy loss from e.g. plasmon excitation, surface plasmons or interband transitions, may however lead to inelastic contributions. To account for both scattering effects, the final simulated TEM is a weighted sum of images with different defocus values. An averaged inelastic contribution is simulated assuming equally weighted energy loss in a range of 10 – 100 eV. An additional defocus of $dz = C_\text{c} \frac{dE}{E_0} \approx 600\,\text{nm}$ is considered. C_c is the microscope chromatic aberration of 1.2 mm and E_0 is the beam energy of 200 keV. A focal series from 0 – 600 nm in steps of 5 nm is simulated to obtain the inelastic contribution image. The resulting TEM image is weighted with equally 0.5 elastic and inelastic contribution. A mean free path of 200 nm of the scattered electrons is assumed. The obtained quasi-elastic substitute image does not account for the physical origin of inelastic scattering but merely account for the optical effect.

To compare simulated TEM imaged directly with experiment, the contrast ranges of the gray scale images are aligned by shifting and normalization, cf. Ref. [1]. Figure 4.16 shows the contrast intensity profiles and corresponding images of both, experimental and simulated TEM. For the simulated images, pure elastic and inelastic and the weighted sum of both contributions is shown.

The intensity profile across the grain boundary averaged over the pixel columns of the TEM gray-scale image exhibits distinct local minima at the aforementioned darker stripes and an

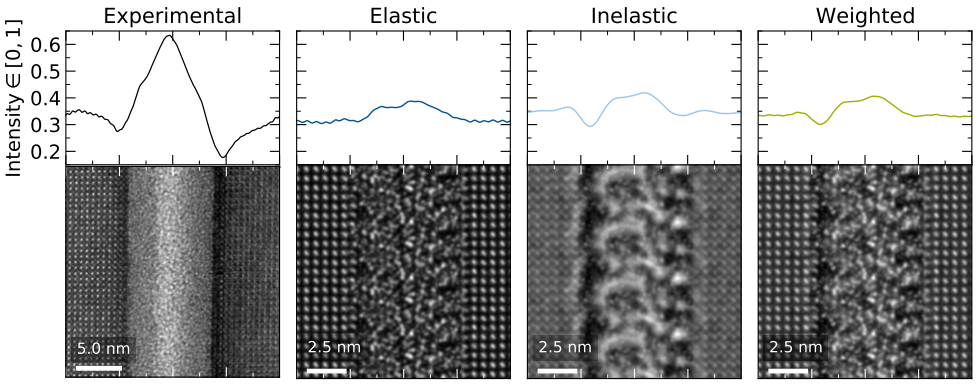

Figure 4.16: Contrast intensity profiles from experimental and simulated TEM images. From left to right: Inset of experimental TEM image with corresponding intensity profile across grain boundary. Elastic simulated TEM image of atomistic model at Scherzer defocus of 63.3 nm and corresponding intensity profile. According "inelastic" contribution of averaged TEM images with defocus values between 0 – 600 nm in steps of 5 nm and corresponding intensity profile. Weighted sum of elastic and inelastic contribution to the simulated TEM image and corresponding intensity profile. Images adapted from Stegmaier et al. [1] under CC BY 4.0.

increase towards the grain boundary center. There are two subtle symmetrical kinks toward the grain boundary center. While the elastic contribution from simulation more accurately reproduces the bright, distinct reflexes, the inelastic contribution image shows higher agreement with experiment for the intensity. Both, the dark regions at the interface, as well as a brighter grain boundary center are better reproduced for the inelastic image. However, neither of the simulated images shows quantitative agreement with experiment. In the final weighted sum of elastic and inelastic contribution, the intensity profile is flattened, yet the characteristic darker rims are maintained.

Other possible reasons, besides inelastic scattering, for an observed intensity brightening can be attributed to changes in chemical composition toward lower atomic numbers, a lower local density, and a decreased sample thickness. Since neither APT measurements, nor STEM EDS suggest a significant chemical change towards lower atomic number elements, the first effect is neglected. Hence, the effect of a lower local density and heterogeneous sample thickness on TEM image contrast are scrutinized. The resulting intensities, density and thickness profiles, as well as the corresponding TEM images are shown in Figure 4.17.

In order to investigate the impact of a lower local density, the grain boundary atomistic model is artificially stretched in an iterative fashion and subsequent thermal annealing. An extreme stretching of the amorphous domain yields a local density of $\approx$1.5 g cm^{-3} in the grain boundary center. The corresponding TEM contrast does exhibit slight brightening, yet the intensity profile is not in quantitative agreement with experiment. Since further stretching is not possible due to ripping effects and such low values do not align with experimentally

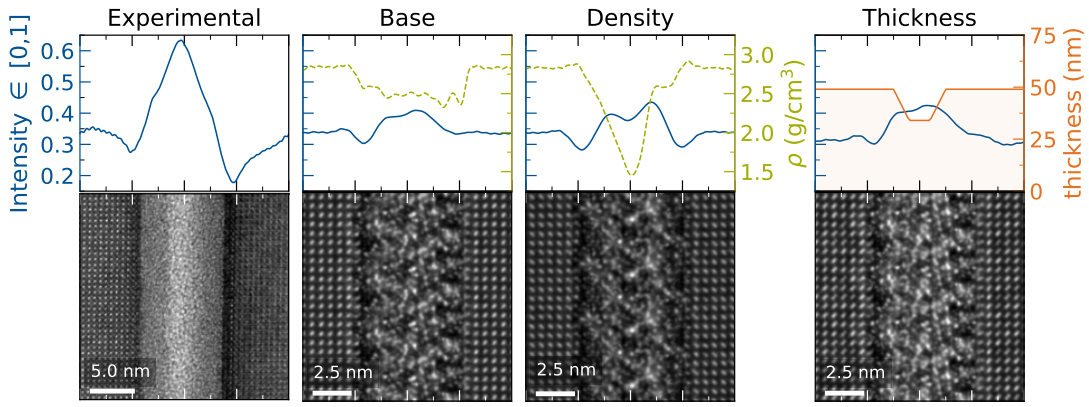

Figure 4.17: Possible density and thickness effects on TEM contrast. All simulated TEM image are a superposition of elastic and inelastic contribution obtained as stated in the text above. From left to right: Experimental inset of TEM image and intensity profile for reference. Simulated grain boundary TEM image of the unchanged atomistic model with intensity across the grain boundary. Effect of grain boundary density variation. Preferential thinning in the grain boundary and respective TEM intensity profile. Images adapted from Stegmaier et al. [1] under CC BY 4.0.

reported relative densities [132], the mass density as obtained from computational sintering is adopted for further analyses.

Preferential thinning, e.g. introduced during TEM sample preparation with Focused Ion Beam (FIB) [239, 240], is modeled by locally altering the sample thickness from a bulk value of 49 nm to a decreased value of 34 nm in the grain boundary center. Similar to the lower density, a reduced thickness does lead to an increase in intensity, yet the strong gradient as seen in experiment is not reproduced.

Neither local density, nor thickness variation satisfactorily reproduces the sharp intensity increase in the LATP grain boundary center as observed in experiment. Therefore, other inelastic effects, such as phonon excitation and interband transitions, are hypothesized to cause the bright streak in the grain boundary center. These are however not in scope of the current work.

4.4.4 Domain Analysis

Quantitative Complexion Assignment

To quantitatively assign the complexion region, a 2D Fourier Transform based approach is introduced. Here, the periodicity of the underlying LATP Ti-Al framework is assessed and spatially resolved across the grain boundary. Atomic positions, i.e. point vectors in space, of Ti^{4+} and Al^{3+} ions are translated into densities by placing 3D Gaussians and mapping onto a regular 3D grid. Density slabs along the z-axis of width Δz are projected into the

2D xy-plane. Taking a 2D Fourier Transform of these density slabs and shifting the zero-frequency component to the plane center, yields the structure characteristic patterns shown in the insets of Figure 4.18 (a). For Ti/Al atoms in the crystalline region, which are aligned in a periodic fashion, the resulting Fourier approach yields few distinct reflexes (left inset). In the amorphous domain, the Ti/Al atoms are more randomly displaced, leading to less intense, yet more reflexes (right inset).

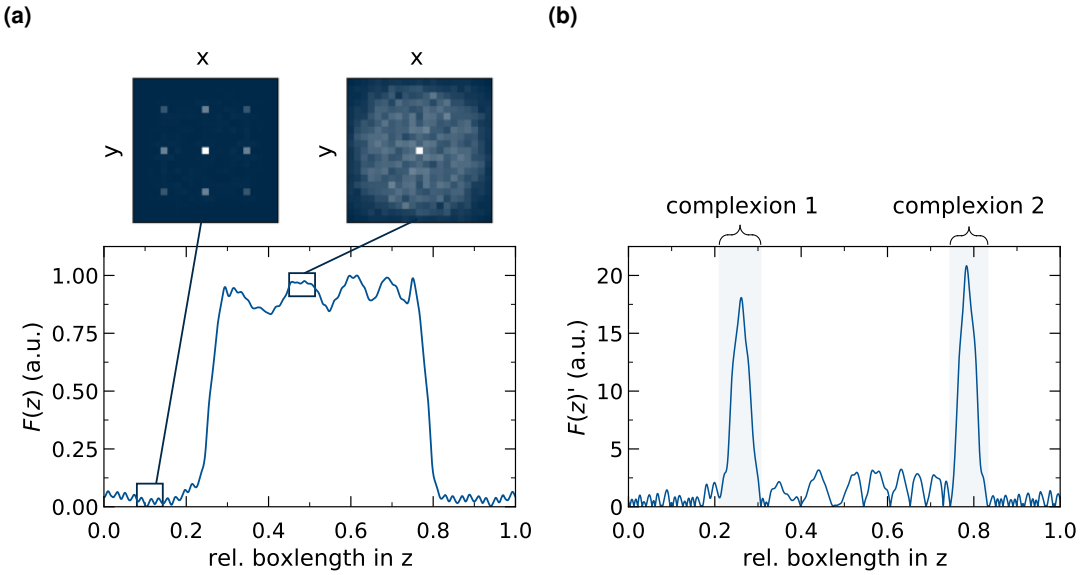

Figure 4.18: Fourier approach for complexion assignment. **(a)** Sum of 2D Fourier Transform intensities $F(z)$ as a measure of amorphization along the z-axis. Insets show 2D Fourier intensity map of crystalline domain (left) and amorphous domain (right) with characteristic reflex patterns. **(b)** Complexion assignment by structural transition obtained from first derivative of $F(z)'$. Images adapted from Stegmaier et al. [1] under CC BY 4.0.

In order to obtain a profile of the degree of structure, or amorphization, respectively, scalar values for each density slab are obtained by summation of the Fourier intensities $I_{\mathrm{2D-FFT}}(z)$ and normalization to its maximum values as

$$F(z) = \frac{\sum_{xy} I_{\mathrm{2D-FFT}}(z)}{\sum_{xy} I_{\mathrm{max}}}. \tag{4.1}$$

In this picture, few and distinct reflexes yield lower values for the sum of intensities, while many less pronounced reflexes yield larger values, cf. Figure 4.18 (a).

The actual assignment into crystalline bulk, complexion and amorphous bulk across the z-axis is based on the transition of structural degree, i.e. the numerical derivative $F(z)'$. The widths for the two complexions can be clearly assigned according to Figure 4.18 (b).

Complexions, by definition, require a thermodynamically self-limiting thickness [44]. To validate an independent complexion width from the adjacent bulk regions, grain boundary struc-

tures are realized with different extended amorphous domains. Five such atomistic models are obtained, following the same construction and sintering protocol. In Figure 4.19 (a), two such atomistic structures with largest amorphous domain L_5^{amorph} and respective smallest amorphous domain L_1^{amorph} are shown. The crystalline domains are the same for all structures. Specifications of the atomistic set up and resulting domain widths for all five structures $L_1 - L_5$ are provided in Table D.1.

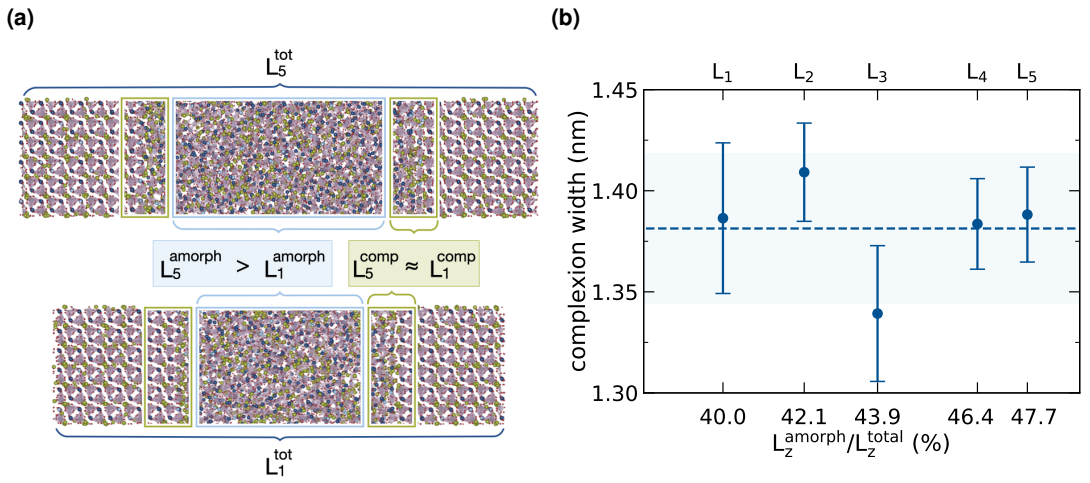

Figure 4.19: Self-limiting complexion width. **(a)** Comparison of atomistic grain boundary structures with different size amorphous domain ($L_5^{\text{amorph}} > L_1^{\text{amorph}}$), yet similar size complexion widths ($L_5^{\text{comp}} \approx L_1^{\text{comp}}$). **(b)** Width of the complexion as quantified by 2D Fourier transforms for simulation cells in which the fraction of the amorphous part ($L_z^{\text{amorph}}/L_z^{\text{total}}$) after computational sintering varied between 40 – 48 % of the total simulation cell length L_z^{total}. Image **(b)** adapted from Stegmaier et al. [1] under CC BY 4.0.

The amorphous part for the five different size structures takes between 40 – 48 % of the total width, i.e. $L^{\text{amorph}}/L^{\text{total}}$. Within error bars, the identified width of the intermediate regions are found to be constant, cf. Figure 4.19 (b), thus justifying the formation of complexions.

Ti-Al Segregation in the Complexion

A consistent energetic preference toward Al-termination of the crystalline slabs against vacuum has been shown for different stochastic surface realizations, cf. Figure 4.8 (b). To prove this segregation prevails also for the sintered structures, five atomistic models are constructed with both, Al- and Ti-termination. For maximum comparability, the truncated slabs for both terminations have the exact same stochastic sampling and merely the surface Al^{3+} ions are swapped for nearest sub-surface Ti^{4+} ions. Equal simulation parameters for the sintering protocol are taken for all models. Relative energy differences $(E_{\text{pot}}^{\text{Al}_{\text{rich}}} - E_{\text{pot}}^{\text{Ti}_{\text{rich}}})/N_{\text{atoms}}$ are shown in Figure 4.20.

Since the majority of atoms in the bulk phases remain energetically unaffected, normalization with the total number of atoms • N_{total} suggests merely small energetic gain for the

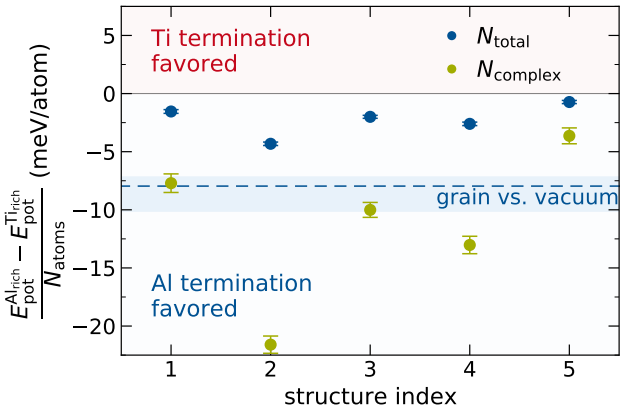

Figure 4.20: Energetic difference of five Ti- vs. Al-terminated sintered grain boundary structures normalized to the number of all atoms ● N_{total} and the number of complexion atoms ● N_{complex}. Image adapted from Stegmaier et al. [1] under CC BY 4.0.

Al-termination. Therefore, the energy difference needs to be normalized by the affected atoms in the complexion ● N_{complex}, which make about 20 % of the entire structure. The energetic analysis confirms a surface termination preference toward Al-rich termination with energetic gains in the range of the slab-vacuum systems. The local Ti-depletion is thus not an artifact introduced by the initial slab design, but renders a key chemical feature of the LATP grain boundary.

The local Ti distribution on a nanometer scale is crucial for electronic conductivity in the ceramic LATP SSE. This is due to the tetravalent Ti^{4+} ion being easily reducible to Ti^{3+} by a nearby electron, which leads to the generation of small polarons [241, 242]. Polaron hopping is the main electron conduction mechanism in ceramic insulators such as LATP and exhibits an exponential dependence on the height and width of the hopping barrier [243]. The electronic conductivity is thus highly sensitive to nearest-neighbor (NN) Ti-Ti distances.

From Radial Distribution Functions (RDFs), the local density of Ti can be spatially resolved and is shown for both, the grain and the grain boundary domain in Figure 4.21 (a). Zooming into the first peak reveals a subtle peak at 4.65 Å for Ti-Ti NN distance in the grain domain, which vanishes for the grain boundary.

An average minimum Ti-Ti NN distance $\langle d^{\text{Ti-Ti}} \rangle$ can be retrieved from the RDF from integrating over the first peak according to

$$\langle d_{\text{Ti-Ti}} \rangle = \frac{\sum d \cdot \text{RDF}(r)}{\int \text{RDF}(r)}. \tag{4.2}$$

The resulting domain resolved distances are shown in Figure 4.21 (b). With an average $\langle d_{\text{crystal}}^{\text{Ti-Ti}} \rangle$ = 4.88keV, the Ti atoms in the crystalline grain approach each other more closely as compared to the amorphous domain and especially the complexion. The local Ti depletion

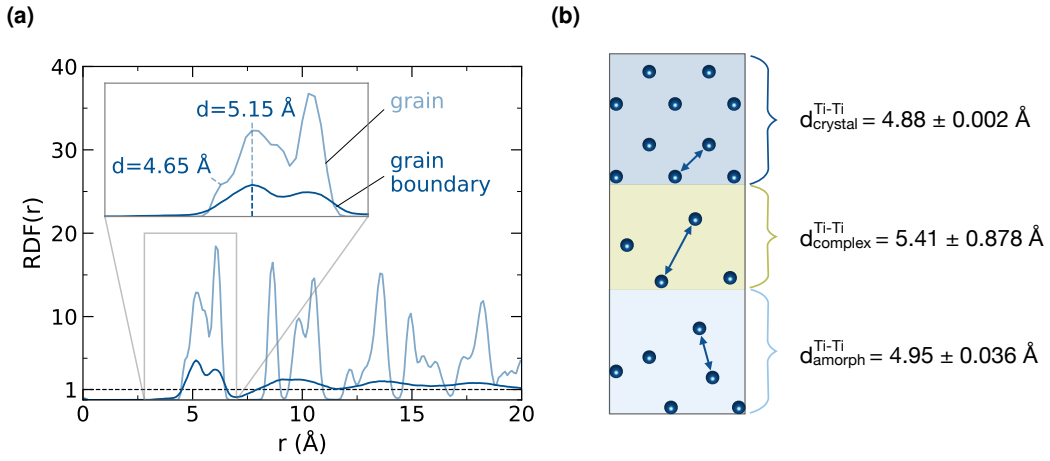

Figure 4.21: Ti nearest neighbor distances. **(a)** Bulk partial RDF of Ti-Ti for grain and grain boundary region with inset of first peaks. **(b)** Schematic illustration of Ti-Ti nearest distances in the different domains as retrieved from RDF analysis. Image **(a)** adapted from Stegmaier et al. [1] under CC BY 4.0.

from Ti-Al segregation at the grain surface leads to a significant increase of the Ti-Ti NN distance by more than 0.5keV with $\langle d^{\mathrm{Ti-Ti}}_{\mathrm{complex}} \rangle = 5.41$ Å. This increase presents a sizable anisotropic electronic impedance for the polaron hopping across the complexion.

4.5 Li Diffusion Simulations and Ion Conductivity

By means of MD Simulation, Li dynamic behavior is accessible in the different domains of the established structural grain boundary models. After equilibration in NVT and NpT for 25 ps and 1 bar, respectively, production runs for 1 ns are conducted at varying temperatures. Following the Nernst-Einstein relation introduced in Section 3.4, the obtained MSDs from ion trajectories are extrapolated to respective ion conductivities. For each temperature, an ensemble of five grain boundary structures is considered and an Arrhenius-like representation with $\log_{10}(T\sigma)$ versus $1/T$ is shown in Figure 4.22 (a).

The domain resolved Li ion conductivities in the crystalline region exhibit generally high agreement with bulk experimental values [47]. This is especially the case for elevated temperatures, where due to improved statistical sampling, the simulation results are more reliable as compared to ambient temperatures.

From experimental Electrochemical Impedance Spectroscopy (EIS) data [47], the contribution of interfacial Li ion conductivity to the overall performance is suggested to be orders of magnitude lower than for bulk LATP. The MD data presented in Figure 4.22 (a), however, does not support such a severe diffusion bottleneck across the interface, i.e. complexion and amorphous domain. Therefore, an observed lower interfacial diffusivity is not an intrin-

sic feature of the LATP grain boundary, but may be attributed to poor interfacial contacting or residual secondary phase with extremely poor Li ion conductivity [96, 165].

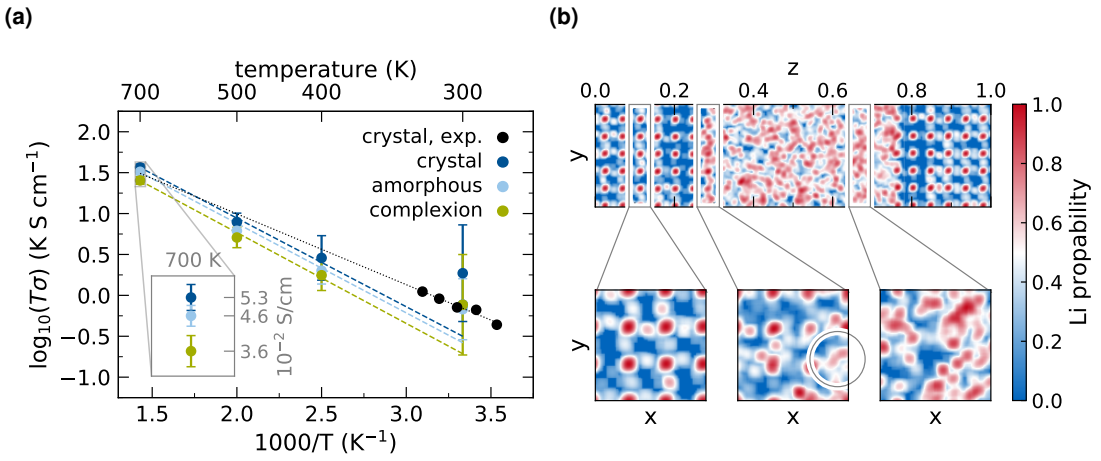

Figure 4.22: Domain resolved Li mobility in grain boundary model. **(a)** Arrhenius plot with the domain-resolved Li ion conductivities as determined from MD simulations. Experimental values from Mertens et al. [47] for crystalline LATP bulk are added for reference. **(b)** Mapped Li ion trajectory from 700 K NVT simulation to visualize Li ion pathways across the grain boundary (top) and respective 2-fold slabs in the xy-plane for the domains: grain (bottom-left), complexion (bottom-center) and amorphous bulk (bottom-right). Images adapted from Stegmaier et al. [1] under CC BY 4.0.

For a mechanistic understanding of diffusion pathways across the LATP grain boundary interface, Li ion trajectories of a 2 ns MD simulation at 700 K NVT are projected onto a 2D density plot as shown in Figure 4.22 (b). In the crystalline domain, the MD simulations confirm the experimentally reported presence of well-defined Li-ion channels [244]. These channels allow for fast Li ion migration through the highly symmetric LATP host.

While the amorphous domain is lacking such long-range structure, the Li ion conductivity obtained from MD simulation is in a similar regime as for the grains. Mechanistically, the diffusion of ions in the amorphous interphase are dominated by free volume hopping, facilitated by the lower atom density of this region [132].

The slightly impeded ion diffusion across the complexion, cf. Figure 4.22 (a), is likely caused by a change in diffusion mechanism from the two adjacent bulk phases. When approaching the complexion, the Li ion channels become more narrow and eventually rip. Such a vanishing channel position is indicated in the Li probability of the complexion. In addition to steric hindrance, the local Ti-depletion in the complexion leads to a deviation in stoichiometric Ti/Al content from an optimal $0.3 \leq x_{\mathrm{Al}} \leq 0.4$ [61, 122, 140].

Error calculation for ion diffusivity

At ambient temperature, few Li ions exhibit diffusive motion but the majority oscillates around their equilibrium position. Assuming the overall diffusion to be a superposition of Gaussian-like oscillatory noise and actual diffusive motion [245], the MSD can be described as

$$\mathrm{MSD}(t) = \mathrm{MSD}_{\mathrm{Gauss}}(t) + \mathrm{MSD}_{\mathrm{Diffusion}}(t). \tag{4.3}$$

For a separation of these motions, a critical distance d_{sep} is introduced, which the ions travel from t_i to t_{i+1} at a position dump frequency of 0.5 ps. Exemplary domain resolved distances travelled for all Li ions in a 1 ns trajectory at 300 K are shown in Figure 4.23 (a).

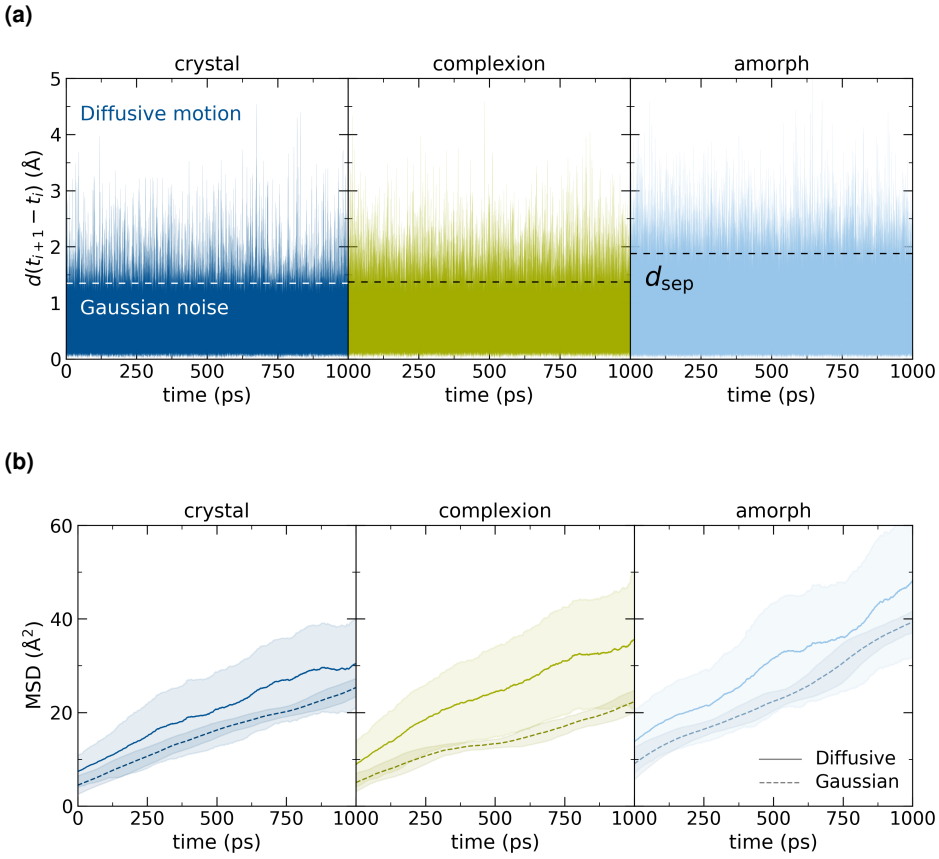

Figure 4.23: Error calculation for Li ion diffusion. **(a)** Exemplary visual assignment of critical distance d_{sep} to separate Gaussian noise from diffusive motion for all Li atoms at 300 K in the crystalline, complexion and amorphous domain. **(b)** Exemplary motion separated MSDs for three domains, i.e. crystalline bulk, complexion and amorphous interphase at 500 K for both, Gaussian noise (dashed) and diffusive motion (solid). Images adapted from Stegmaier et al. [1] under CC BY 4.0.

Since the density is lower in the amorphous domain, the ions can oscillate further from their equilibrium position leading to a larger value of d_{sep}. This separation of motion is conducted

for all domains at different temperatures. At elevated temperatures, the diffusive events become more frequent and the oscillation amplitude becomes larger.

By separating the motion based on a distance criterion, two individual MSDs can be computed as shown in Figure 4.23 (b). Since the atom positions are taken from the same MD trajectory, the overall distance travelled in the MSDs are similar. However, the poor statistical sampling for the diffusive MSD leads to larger deviation as compared to the Gaussian noise.

The obtained diffusive error is propagated to the macroscopic properties, i.e. diffusion coefficient and ionic conductivity, via Gaussian error propagation in Equations (3.23) and Equation (3.25). For the linear regression in the Arrhenius-like plots, the errors are taken as reciprocal weights, thus accounting for temperature dependent statistical confidence.

4.6 Electronic Structure Calculations[(4.7)]

The Li diffusion analysis from MD simulation has shown that the reported high dendrite suppression capability of LATP cannot be attributed to a low interfacial mobility in the grain boundary. Therefore, electronic structure calculations are performed to localize an introduces excess electron at the interface.

For a more stable convergence, the Density Mixing Ensemble-DFT (DM-EDFT) method is used for solving the Kohn-Sham equations [246]. The electronic structure is relaxed using the CASTEP [247] pseudo-potential plane wavecode with Ultrasoft Pseudo Potentials as provided in the GBRV library [248]. To approximate the exchange-correlation effects, the default GGA-level PBE functional [185] is employed. Simulation parameters are chosen as 750 eV for the cutoff energy and 0.07 Å for the k-point spacing. Convergence testing for these parameters is shown in Appendix E.

Due to the observed energetic preference and the distinct chemical composition in the complexion, the computationally demanding DM-EDFT calculations are concentrated on smaller atomistic structures of Al-terminated grains. The investigated slab geometries comprise a total of 1098 atoms are obtained from the protocol outlined in Section 4.4.1. The electronic system structure is relaxed for the neutral state and a formally negatively charged state after injection of an excess electron.

To compute the excess electron density profile along the z-axis, $\rho_{\text{excess}}(z)$, charge density differences are integrated via numerical binning in x and y direction according to

$$\begin{aligned} \rho_{\text{excess}}(z) &= \int_y \int_x \rho_{\text{excess}}(x, y, z)\, \mathrm{d}x\, \mathrm{d}y, \quad \text{with} \\ \rho_{\text{excess}} &= \rho_{\text{charged}} - \rho_{\text{neutral}}. \end{aligned} \tag{4.4}$$

Figure 4.24 (a) shows the excess electron density profile along the z-axis. The injected electron localizes in close proximity to a Ti^{4+} ion, which is in agreement with experimental

[(4.7)] Excess charge DFT calculations were performed by Dr. S. P. Rittmeyer, Chair of Theoretical Chemistry and Catalysis Research Center, Technical University of Munich.

reports of a favored reduction of Ti^{4+} during cycling of LATP [249]. This localization accounts for 35.7 % of the excess charge on a single Ti^{4+} center in the subsurface layer. Negative excess charge densities amounting to 4.3 % even suggest withdrawal of electronic density in the terminating layer toward the reducing transition metal center.

A residual excess charge of 51.9 % is smeared out across the remaining bulk Ti centers. This charge delocalization is known artifact of the underlying semi-local GGA-level functional. Two exemplary bulk Ti ions suggest an integral excess electron density of ≈6 %, cf. inset in Figure 4.24 (a). The shaded area at low values of z is neglected, as no significant charge accumulation is found.

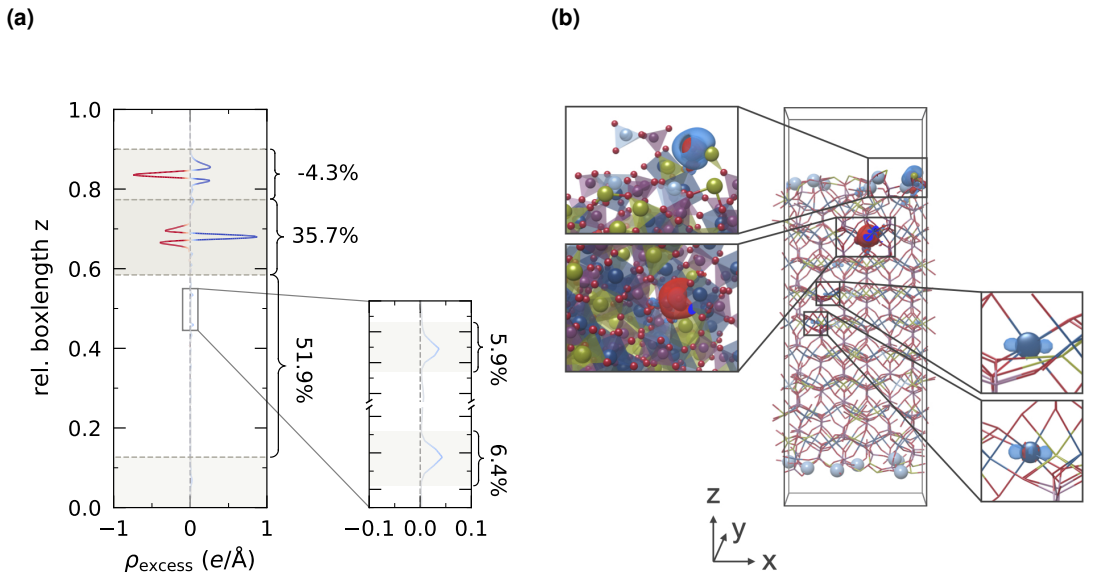

Figure 4.24: DFT calculations of localized electronic excess charge in the Ti-depleted complexion. **(a)** Electronic excess charge density ρ_{excess} over the simulation box length and averaged over planes parallel to the surface. Positive/negative values indicate electron accumulation/depletion. The excess electron is mainly located in sub-surface layers containing Ti^{4+} ions, as demonstrated by the integral of the excess density. A delocalization of excess electron density (≈52 %) among bulk Ti^{4+} ions (inset) is a known artifact in semi-local functionals such as generalized gradient approximation (GGA) [241, 250]. The rearrangement of electronic density even withdraws a small amount (4.3 %) of electron density from the surface layer. **(b)** Corresponding side view of the simulation box with superimposed isosurfaces of electron depletion (red, -0.805 e/Å^3) and electron accumulation (blue, +0.916 e/Å^3), confirming the Ti^{4+} ions as location of a generated small polaron. Images adapted from Stegmaier et al. [1] under CC BY 4.0.

A respective atomistic structure with superimposed electron density isosurfaces is shown in Figure 4.24 (b). Close-ups to the left show electron depletion for the surface Al^{3+} ion and respective electron accumulation for Ti^{4+} in subsurface layers. The close-ups to the right depict residual excess electron density located on two bulk Ti^{4+} centers.

Despite the known delocalization artefact of the electronic structure method used, the excess electron density accumulated predominantly in sub-surface layers. The resulting small polaron is thus also localized sub-surface and spatially separated from the amorphous interphase. Since the polaron hopping depends exponentially on the height and width of the barrier, this spatial separation presents a LATP intrinsic electronic barrier in the complexion. The characteristic chemical composition of the complexion thus effectively insulated the grain from electronic conduction.

4.7 Summary

Leveraging the structural information from HR-TEM images and chemical composition from APT measurements, a novel atomistic modeling approach is presented toward more realistic solid-solid interfaces. A complex multi-phase grain boundary of the LATP SSE is obtained from the introduced computational sintering protocol in this work. The atomistic resolution allows for the identification of a thin, nanometer-sized complexion forming between the crystalline LATP grain and a glass-amorphous interphase.

A thermodynamically self-limiting width and noticeably different structural and chemical built classify the interfacial region an actual complexion [43, 44]. In experimental TEM images, the gradual loss of structure across the complexion is recognizable from darkened stripes at the interface between LATP grain and grain boundary. To a lesser extent, this characteristic contrast profile across the interface is reproduced from combining elastic and auxiliary inelastic contributions in the TEM image simulations. Chemically, the established atomistic grain boundary models support APT findings of a local Al-enrichment and a concomitant Ti-depletion in the complexion, which are energetically favorable.

Li dynamic analyses from extensive MD simulations in the different domains and across the interface do not support severe ion diffusion blockage. On the contrary, the glass-amorphous nature in the grain boundary facilitates similarly high Li conductivity as obtained for the crystalline grain. Li iso-density studies confirm the high charge carrier mobility in the grain to be attributable to the experimentally postulated presence of well-defined channels [244]. In the amorphous domain, the observed Li mobility is driven by a larger free volume. Exactly this change in mechanism at the complexion leads to a slightly lower local ion conductivity. Grain boundaries in LATP thus do not present an inherent bottleneck to Li diffusion. Other local defects, such as poor contacting or residual secondary phases, largely contribute to the experimentally reported orders of magnitude lower interfacial conductivity [47].

The found nano-scale segregation of Ti and Al in the complexion provides a new facet toward understanding the surprisingly high dendrite suppression capability of LATP [146, 169]. While the bulk electronic conductivity measured in experiment exceeds a postulated critical threshold by orders of magnitude [40], the depletion of Ti and a resulting increase in Ti-Ti distances justify a sizable barrier for electron transport via polaron hopping. The bulk LATP grains are thus encapsulated by a protective, electronically insulating complexion.

Aging and degradation in SSEs crucially depend on charge carrier dynamics, i.e. Li ions and electrons. A purely macroscopic approach via bulk measures for both, ionic and electronic conductivity, does not sufficiently account for the underlying processes. Instead, as shown herein, a detailed understanding at the atomistic level is needed to resolve local phenomena, which complement the bulk material assessment. Within this picture, an extremely low residual electronic conductivity may not be needed for the deterioration of dendrite nucleation in LATP, as a nano-scale separation of charge carriers presents an insuperable electronic barrier. The otherwise thermodynamically redox unstable adjacent bulk phases may thus be kinetically stabilized.

5 Active Interfacial Engineering via Aliovalent Doping in LATP[5.1]

In this chapter, active interfacial engineering of the previously established LATP grain boundary model is explored computationally. Divalent Mg^{2+} is established as a viable candidate for aliovalent interface doping. To investigate the effect of the dopant and its concentration on overall SSE performance, different amounts of Mg^{2+} are introduced into the interphase region. Interdiffusion into adjacent grain domains, i.e. dopant bleeding, is modelled via a novel ion swapping protocol based on Monte-Carlo (MC) simulations. The Mg^{2+} ions mostly stay spatially confined and only minimal bleeding into the grains is observed. Ion dynamic analyses do not exhibit severe clogging of Li channels, thus not impairing overall bulk grain performance. By deliberately substituting Ti^{4+} for Mg^{2+} and excess Li^{+} in the grain boundary, the residual electronic conductivity via polaron hopping can be lowered. The concomitant local increase in Li^{+} charge carrier concentration yields a conductivity increase in the grain boundary. It is shown, how the protective nature of LATP inherent complexions can be exploited and grain boundary properties can be improved via interfacial doping with Mg^{2+}.

5.1 Motivation

In a consequent step of developing multi-component functional solid-state devices, efforts in material research are shifting from bulk material design towards the active engineering of solid-solid interfaces [27, 28]. While bulk properties play a crucial role in the overall performance, challenges in realizing ASSBs can be attributed to interfacial processes, see Section 2.3. Reactive electrochemical instabilities between phases in contact, as well as metallic dendrite nucleation and growth are processes which often result in cell failure [29, 31]. Even for theoretically compatible bulk materials, microstructural defects introduced during SSE processing often present an accessible route for dendrite penetration due to their mechanical properties [32–34].

The majority of engineering approaches is targeted at modifying the interface between electrode and electrolyte, e.g. by introducing buffer layers [251] or ultra smoothing of SSE surfaces for improved contacting [148]. Besides the exposed surface to the electrodes, buried

[5.1] Adapted in parts from Stegmaier et al. [2] under CC BY 4.0.

interfaces within the SSE are of great interest to suppress dendrite growth and residual electron transport through the network of grain boundaries. Recently, Xu et al. [252] have illustrated how a dendrite suppressing glassy phase distributes along the grain boundaries in $Li_{6.5}La_3Zr_{1.5}Ta_{0.5}O_{12}$ (LLZTO) by mixing with second phase additives.

Since the interfaces are buried and thus not easily accessible, modification and post synthesis analysis is challenging in experiment. Therefore, computational methods are not only crucial to understand the interfacial processes mechanistically, but also to predict promising engineering routes. Simulations, mostly at first-principles level, have been conducted on predicting electrolyte/electrode interfacial compatibility [9, 223, 253]. The premise of such computationally costly simulations is the mapping of a representative system into smaller idealized cells to arrive at manageable length and time scales. However, multiphase buried interfaces with their often low degree of crystallinity require much larger system sizes to represent a realistic model of an extended grain boundary.

Based on the atomistic model established in Chapter 4, a grain boundary in the ceramic LATP is considered for interfacial engineering. Experimental findings from TEM and APT [1] have entered the construction of the model, rendering it a realistic buried interface in LATP. A protective nano-scale complexion encapsulating the crystalline LATP grains has been identified, which mitigates reductive degradation and Li nucleation. Cationic doping of the interface is investigated to further exploit the advantageous nature of this grain boundary. From APT measurements, an observed local accumulation of Mg^{2+} in the amorphous grain boundary streak motivates this divalent cation as a potential interfacial dopant candidate. Classical force field simulations are employed to investigate the effect of different doping concentrations on critical local and overall SSE properties.

Three requirements are postulated as prerequisites for a successful engineering of buried interfaces:

1. The interfacial dopant must not penetrate severely into the adjacent crystalline bulk of the electrolyte grains, but stay spatially confined, to guarantee long-term stability.
2. The bulk electrolyte performance must not be significantly compromised by the interfacial doping.
3. Interface modifications should exploit and enhance desirable electrolyte features.

Mg^{2+} doping of an LATP grain boundary is screened to identify conditions that meet these requirements.

5.2 Mg^{2+} as Interfacial Dopant Candidate

APT measurements identify a local accumulation of cationic Na^+, K^+, and Mg^{2+} impurities in the LATP grain boundary sample, cf. Figure 4.3 (c). Both monovalent alkali metal ions, Na^+ and K^+, are disregarded as interfacial dopants. Due to their larger ionic radii as compared to Li^+ [254], they are expected to clog the Li-ion channels when incorporated into the LATP framework. The focus is thus on divalent Mg^{2+} as a promising interfacial dopant candidate.

Encouraging results from interfacial doping with Mg^{2+} into the $Na_{1+x}Zr_2Si_xP_{3-x}O_{12}$ NASICON SSE have recently been reported by Cheung et al. [255].

In general, Mg^{2+} is a suitable dopant candidate in Lithium Ion Batterys (LIBs) due to its high electrochemical stability against metallic Li [256, 257]. Increased steric demands of the dopant need to be considered for mechanical destabilization of the underlying SSE system. However, the similar ionic radius of Mg^{2+} as compared to all other LATP-constituting elements [258] does not hint towards severe structural disintegration or steric hindrance.

With a formal charge of $q_{Mg} = +2$, which is different from all other cations present in LATP, Mg^{2+} furthermore allows for aliovalent doping. In highly ordered materials, i.e. crystalline ceramics, aliovalent doping is a common engineering tool to introduce defects which may enhance ion mobility [259]. In amorphous materials, doping with ions of different valence opens a design route to modify the ionic composition. To maintain charge neutrality, a decrease in content of higher valent cations, such as Ti^{4+} and Al^{3+}, leads to an increase of lower valent cations, such as Li^+.

The Mg^{2+} atom map retrieved from APT is shown in Figure 5.1 (a), with an accumulation in the grain boundary streak; the Li^+ atom map is provided to visualize the full APT sample. A peak concentration well below 1 at% in the grain boundary, cf. Figure 5.1 (b), renders the Mg^{2+} accumulation as an unintentional impurity.

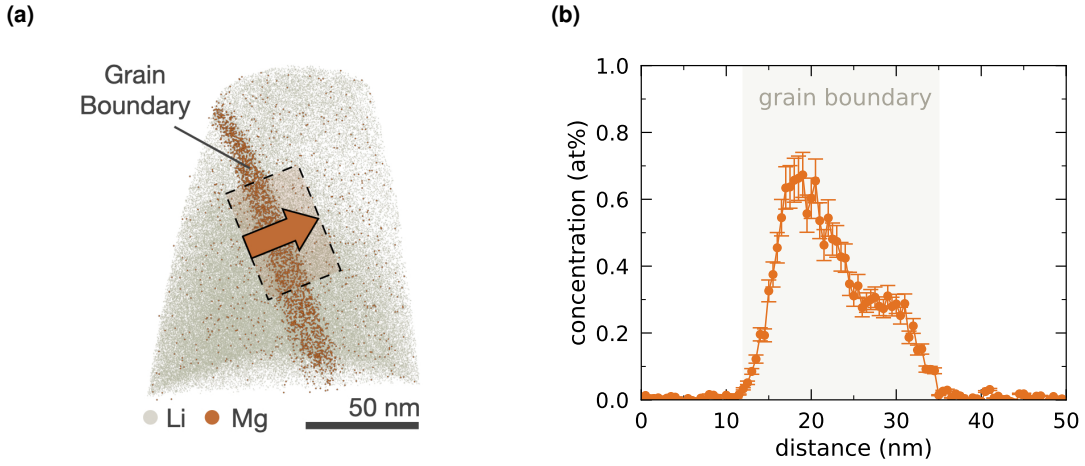

Figure 5.1: Local accumulation of Mg^{2+} in LATP grain boundary streak from APT findings. **(a)** Reconstructed Mg impurity atom map ● showing accumulation in the grain boundary and Li atom map ● as reference of the APT sample. **(b)** Corresponding elemental profile for Mg across the grain boundary ⁚¯⁚ from APT experiment. Images reproduced from Stegmaier et al. [2] under CC BY 4.0.

5.3 Computational Details

MD Simulations employed in this chapter are performed using the LAMMPS Molecular Dynamics Simulator [209]. The classical core-shell force field for the electrolyte material $Li_{1.3}Al_{0.3}Ti_{1.7}(PO_4)_3$ (LATP) introduced in Section 4.3.1 is extended by Mg^{2+} interaction parameters. The time step for numerical integration is chosen as 0.2 fs to account for high frequency core-shell vibrations. Relaxation times for canonical NVT and isothermal-isobaric NPT simulations are adopted with $T_{\mathrm{damp}} = 10^2 \Delta t$ and $p_{\mathrm{damp}} = 10^3 \Delta t$. Short-range interactions are considered up to a distance of 9 Å. Long-range Coulombic interactions are treated using a PPPM solver [193].

5.3.1 Force Field Extension by Mg^{2+} Parameters

The underlying $Li_{1.3}Al_{0.3}Ti_{1.7}(PO_4)_3$ classical force field introduced in Section 4.3.1 is used as a starting point. Herein, polarization of the phosphates is accounted for via a core-shell treatment of the oxygen. Parameters for the core-shell system are adopted from Kerisit et al. [234]. The Born model of solids, cf. Section 3.2.1, is applied and a Buckingham potential is used to describe long-range Coulombic and short-range van der Waals interactions. Parameters for the LATP system are listed in Table A.1. An extension of the LATP force field involves the parameterization of Mg^{2+} interactions only. All other parameters remain unchanged, as the force field has proven to reproduce key features of the LATP system and doping of Mg^{2+} is not expected to have a drastic effect on the overall behavior. Therefore, the formal charge is determined by twice the Li^+ charge with $q_{\mathrm{Mg}} = +1.098\, e$. The mass and effective ionic radius are given as $m_{\mathrm{Mg}} = 24.305$ u and $r_{\mathrm{Mg}} = 72.0$ pm [258]. The atom type specific parameters are provided in Table A.2.

Local optimization of Mg^{2+}-Phosphate parameters

To reduce complexity, Mg^{2+}-PO_4^{3-} interactions are first tested independently on the $Mg_3(PO_4)_2$ material. An orthorhombic supercell comprising 1404 atoms is cut from the reference database structure. The corresponding atomistic structure is depicted in Figure 5.2 (a). Initial values of the Mg-O, Mg-P and Mg-Mg Buckingham parameters B are chosen as an arithmetic mean of the respective Li^+ and Al^{3+} parameters according to

$$B_{\mathrm{Mg}^{2+},j} = \frac{B_{\mathrm{Li}^+,j} + B_{\mathrm{Al}^{3+},j}}{2}. \tag{5.1}$$

This initial parameter guess is based on the charge consideration $q_{\mathrm{Mg}^{2+}} = q_{\mathrm{Li}^+} + q_{\mathrm{Al}^{3+}}/2$. Relaxation of the $Mg_3(PO_4)_2$ geometry with these initial parameters yields a density of 3.16 g cm^{-3}, which is about 20 % higher than for the reference system [260]. Thus, the repulsive contribution to the Buckingham potential, i.e. the ρ_{ij} parameter, is optimized.

Local optimization is performed using a L-BFGS optimizer as implemented in the *SciPy* python library [207]. An optimum parameter set is obtained from varying the $\rho_{\text{Mg-ion}}$ values to minimize volume difference from the reference structure provided in Table A.3. The struc-

tures are equilibrated in NPT at 300 K and 1 bar for 20 ps to ensure volumetric relaxation in between optimization steps.

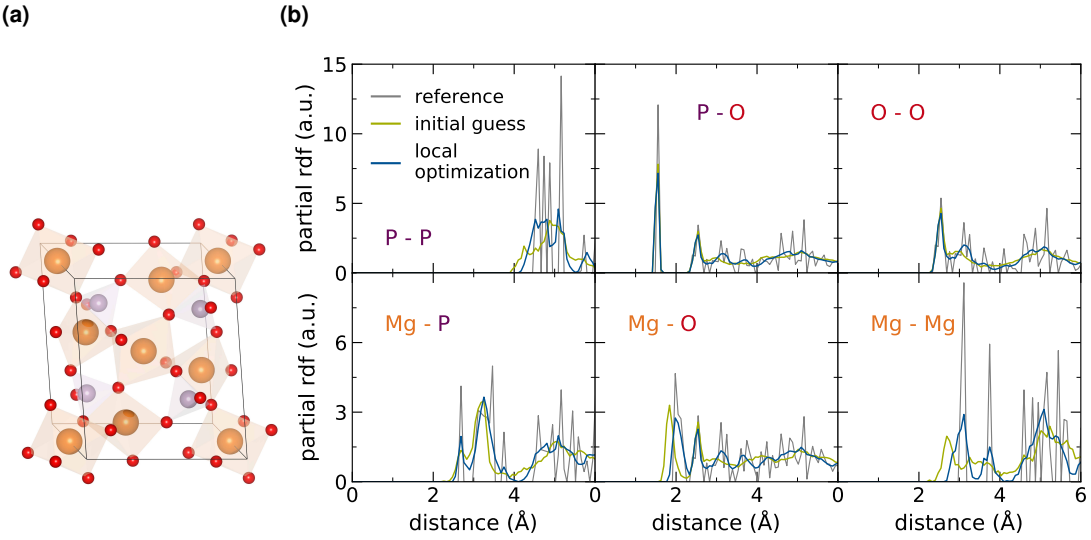

Figure 5.2: Local optimization of Mg^{2+}-Phosphate interaction parameters in $Mg_3(PO_4)_2$. **(a)** Atomistic structure of $Mg_3(PO_4)_2$ (ID: mp-14396 [260]). Elemental colors chosen as Mg ●, O ● and P ●. **(b)** Partial RDFs for reference structure, initial interaction parameters from arithmetic mean of Li^+ and Al^{3+} and locally optimized interaction parameters. Images reproduced from Stegmaier et al. [2] under CC BY 4.0.

Partial RDFs of the different ion pairs, as shown in Figure 5.2 (b), are obtained from a NPT MD simulation at 300 K and 1 bar for 50 ps for the initially guessed and locally optimized parameter sets. Due to thermal vibration, the RDFs recovered from MD simulations show a broadening of the RDF characteristic peaks as compared to the reference structure. Especially the Mg-O and Mg-Mg partial RDFs after local optimization, show better agreement with the reference structure as compared to the initial guess. A larger average nearest neighbor distance of Mg-O after optimization yields a density of 2.67 g cm^{-3}, which deviates below 1 % from the reference density. The resulting parameters from local optimization serve as input values for the subsequent fitting of all Mg^{2+} interaction parameters via global optimization.

Global optimization of Mg^{2+} doped LATP parameters

For a global optimization of the full Mg^{2+} parameter set, a fitting to first-principles DFT reference data is performed. Databases of three stoichiometries with different Mg doping concentrations are set up both, for small crystalline and amorphous slabs each comprising ≈220 atoms. The stoichiometries are chosen according to $Li_{1+x+2y}Al_xMg_yTi_{2-x-y}(PO_4)_3$ with $x + y < 0.5$. Crystalline slabs are cut from the ICSD database structure [261] and amorphous slabs are cut from the amorphous bulk of previously established grain boundary models [1].

With 25 crystalline and 25 amorphous stochastically doped structures for each stoichiometry, the database comprises a total of 150 structures.

Reference potential energies and atomic forces are computed from single point DFT calculations using the pseudo-potential plane wave code CASTEP [247], the GGA-level PBE functional [185], and ultrasoft pseudopotentials as provided by the GBRV library [248]. A plane wave cutoff energy of 750 eV and a Monkhorst-Pack grid density [236] of 0.07 $Å^{-1}$ are employed as previously tested for convergence, cf. Appendix E.

Global optimization is performed using a PSO, as implemented in the *inspyred* python module [206]. Settings for the optimization algorithm are chosen with a population size of 200 and 500 generations. The scoring function is comprised of energy and force contributions, cf. Equations (3.9) to (3.11). Elemental weights for ions other than Mg^{2+} are set to zero, as these are not reparameterized to maintain the original force field for LATP. Force matching is prioritized by one order of magnitude as compared to energy matching, i.e. $w_F = 10\, w_E$, since $3\, N_{\mathrm{Mg}}$ cartesian contributions to the force vector enter the optimization scheme. A subsequent local optimization using a L-BFGS algorithm is performed, which yields the final Mg^{2+} interaction parameters as listed in Table A.2.

5.3.2 Validation of Extended Force Field

Force field and DFT reference correlation of potential energy, with respect to the lowest energy of the same stoichiometry, and atomistically resolved force components for each stoichiometry is shown in Figure 5.3.

Two distinct clusters for the energetically lower crystalline and energetically higher amorphous structures can be differentiated for all stoichiometries. High energy values for amorphous structures are systematically overestimated. Energetic correlation for the classical force field of such a high order system is in agreement with DFT reference. The degrees of freedom for optimization of Mg^{2+} parameters in the fixed LATP host force field is limited as the majority of atom interactions does not contain the Mg^{2+} dopant. Considering the constraints from all other atom species, the force correlation is sufficient for this classical force-field type and is used to describe doping effects.

Doping with Mg^{2+} for the specific LATP SSE material has not been reported so far. Therefore, Li dynamic behavior of the extended force field is validated against *ab initio* data for Mg^{2+} doping of the structurally very similar $Li_{1+x+2y}Al_xMg_yGe_{2-x-y}(PO_4)_3$ (LAMGP) [262]. For this purpose, a crystalline LATP cell containing 893 atoms is constructed with 75 % Ti site occupation by Ti^{4+}, 20 % site occupation by Al^{3+} and 5 % occupation by Mg^{2+}. The doping contents are equal to the reference LAMGP structure with x = 0.4 and y = 0.1, respectively. Accounting for the stochastic nature of doping to full occupancy, five such LAMTP structures are constructed. MD simulations are conducted at 300 K, 400 K, 500 K, 700 K, and 1400 K. Each structure is equilibrated at 1 bar and the respective temperature for 50 ps and production runs are conducted in NVT at the respective temperature for 500 ps.

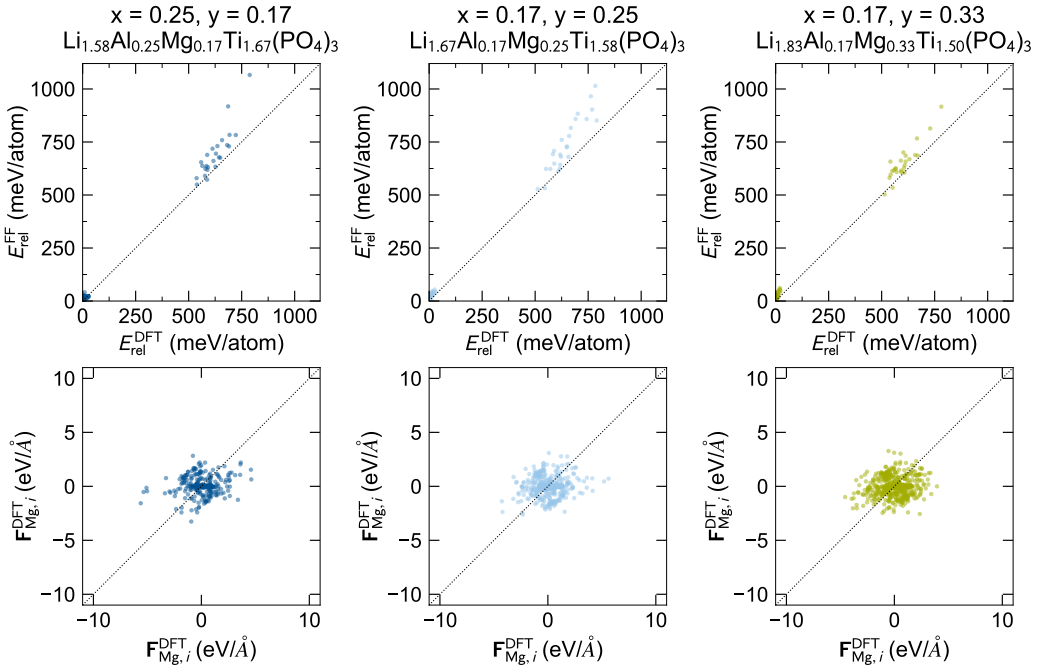

Figure 5.3: Energy (top) and force (bottom) correlation of $Li_{1+x+2y}Al_xMg_yTi_{2-x-y}(PO_4)_3$ structures computed with an extended classical force field and reference DFT data. Correlations are resolved for each stoichiometry. Images reproduced from Stegmaier et al. [2] under CC BY 4.0.

Elemental MSDs for a LAMTP structure at 700 K, as shown in Figure 5.4 (a), confirm Li to be the only mobile species and all other ions to be virtually immobile. The ionic trend with

$$Li^{+} \gg O^{2-} > Mg^{2+} > P^{5+} \simeq Al^{3+} \simeq Ti^{4+}/Ge^{4+},$$

qualitatively reproduces the trends reported by Nikodimos et al. [262].

Figure 5.4 (b) shows the Arrhenius-type plot for Li ion diffusion of LAMTP and LAMGP at different temperatures. Pristine bulk conductivities of the structurally similar NASICON-type SSEs LATP and LAGP with $3.0{\cdot}10^{-3}$ S cm^{-1} [122] and $3.38{\cdot}10^{-4}$ S cm^{-1} [263], respectively, differ by 1.42 orders of magnitude. The higher mobility of Mg^{2+} LAMTP by 1.44 orders of magnitude, as compared to the reported LAMGP diffusivity [262], reproduces this difference. The extended LATP core-shell force field by Mg^{2+} interaction parameters thus yields satisfactory agreement with the limited reference data available for the specific Mg^{2+} doping of LATP NASICON material class.

5.4 Atomistic Structures of Mg^{2+} Interfacially Doped LATP

To scrutinize the effect of interfacial doping of LATP with Mg^{2+}, a previously established atomistic grain boundary structure is used as reference. A comprehensive protocol on how

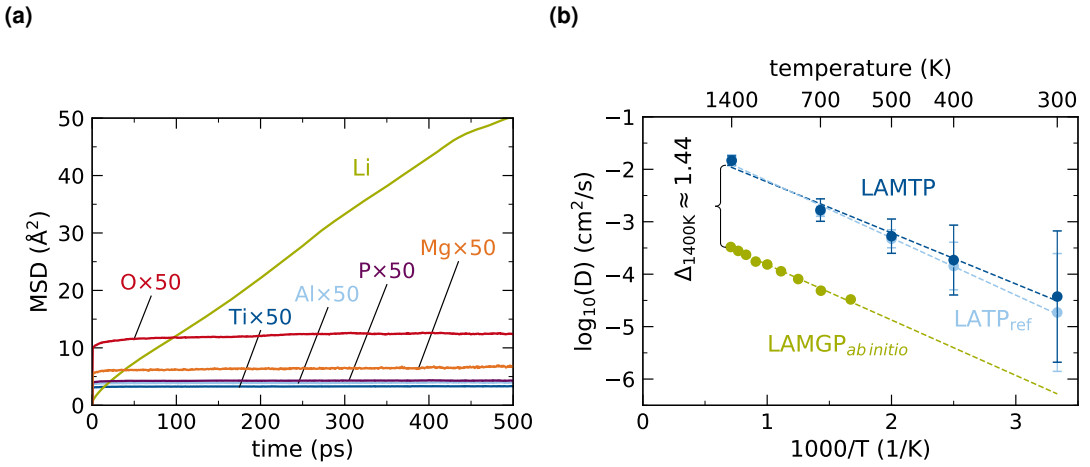

Figure 5.4: Ion dynamics in crystalline $Li_{1.6}Al_{0.4}Mg_{0.1}Ti_{1.5}(PO_4)_3$ (LAMTP). **(a)** Elemental MSDs for a representative LAMTP structure at 700 K. MSDs for immobile species are magnified by a factor of 50 to visualize ionic trends. **(b)** Arrhenius-type plot with Li diffusion coefficients as determined from MD simulations. Also shown are *ab initio* values from Nikodimos et al. [262] for doped $Li_{1.6}Al_{0.4}Mg_{0.1}Ge_{1.5}(PO_4)_3$ LAMGP bulk and respective LATP reference values of the undoped system. Images reproduced from Stegmaier et al. [2] under CC BY 4.0.

these models are constructed is given in Section 4.4. In brief, the protocol yields a multiphase model with crystalline grains, which are encapsuled by a nano-sized complexion, and an amorphous grain boundary bulk. These three structurally different domains can be differentiated from 2D Fourier analysis of the distortion within the Ti-Al submanifold. An atomistic structure of the resulting grain boundary GB_{ref} and the domains is shown in Figure 5.5.

Respective atomistic structures of crystalline C_{ref} and amorphous bulk A_{ref} reference cells are shown in the bottom row. The crystalline supercell is cut from the database LATP structure [261] and sampled to full occupancy. In order to obtain the bulk amorphous cell, a subcell is cut from respective region in the grain boundary model. During cutting, phosphate units are kept intact even if oxygen atoms extend through the cell, yielding a slightly larger volume. To maintain charge neutrality, the exact composition of cationic species Li^+, Al^{3+}, and Ti^{4+} is slightly modified.The final amorphous bulk cell is obtained by iteratively compressing and equilibrating the system to hit the target amorphous density of 2.49 g cm^{-3}, cf. Figure 4.13 (a), and relaxed in NPT at 1 bar and 300 K for 100 ps.

Following the profile from APT measurements, cf. Figure 5.1 (b), Mg^{2+} is initially doped into the amorphous bulk domain of the reference GB_{ref} only. In order to maintain system charge neutrality upon aliovalent doping, ionic substitutions are performed according to

$$1\,Ti^{4+} \longrightarrow 1\,Mg^{2+} + 2\,Li^+ \quad \text{or} \tag{5.2a}$$

$$1\,Al^{3+} \longrightarrow 1\,Mg^{2+} + 1\,Li^+. \tag{5.2b}$$

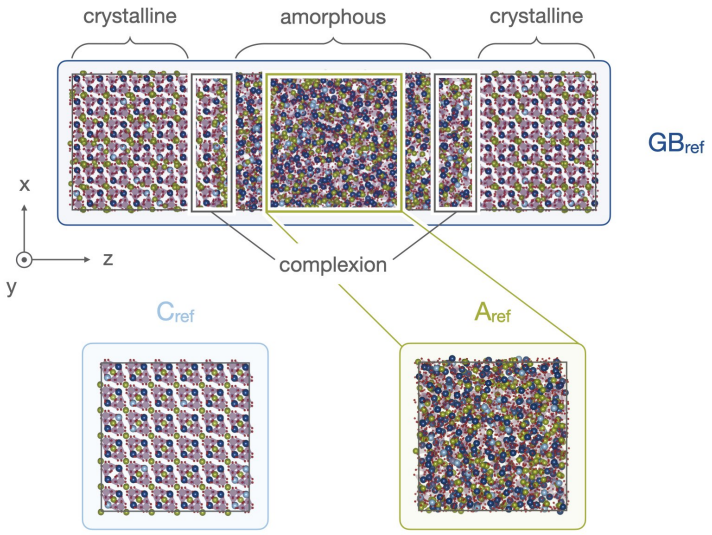

Figure 5.5: Atomistic reference structures of LATP grain boundary GB_{ref} and representative bulk structures for LATP crystalline slab C_{ref} and amorphous bulk slab A_{ref}. The grain boundary structure is differentiated into crystalline grains, amorphous bulk and nano-scale complexions encapsulating the grains. The amorphous bulk is cut from the respective bulk domain in the grain boundary structure. Elemental colors are chosen as Li ●, Al ●, Ti ●, O ●, and P ●. Images reproduced from Stegmaier et al. [2] under CC BY 4.0.

Despite other possible charge neutral substitutions, these two ion exchanges are chosen to first, deliberately reduce the Ti^{4+} content and second, to simultaneously increase the Li^{+} charge carrier content. The former leads to a decrease in TM centers, which are known to limit the material's stability towards metallic Li due to polaron hopping [242, 264]. The latter local increase Li^{+} is expected to favorably influence ion conductivity as recently suggested by Mertens et al. [47]. The substitution in Equation (5.2a) would in principle suffice to achieve a simultaneous TM reduction and local Li^{+} enrichment. However, though the substitution is charge balanced, the number of ions is increased from a single Ti^{4+} to three lower valent cations. This leads to a substantially higher particle count in the amorphous grain boundary, which may affect the structural integrity of the host system. Therefore, both Al^{3+} and Ti^{4+} are substituted according to Equations (5.2) to mitigate this risk of local overpopulation.

The effect of Mg^{2+} doping concentration is investigated by analyzing amorphous bulk models with dopant contents of 0.6 at% – 7.1 at% for $GB_1 - GB_7$, cf. Figure 5.6 (a). For all doped structures, the underlying reference structure GB_{ref} remains the same. The lower doping limit in GB_1 is chosen to reproduce the Mg^{2+} content found in the experimental LATP grain boundary, cf. Figure 5.1 (b). The upper respective limit in GB_7 is chosen to reduce the amorphous reference Ti^{4+} content to approximately half. Mg^{2+} concentration profiles across the grain boundary are shown for all realized dopings in Figure 5.6 (a). For each doping concentration, 12 realizations are initially sampled by ionic substitutions in the amorphous bulk to account for the stochastic nature of the doping process. After application of a MC

protocol, cf. Section 5.5.1, the initial structures are relaxed into energetically more favorable configurations. The lowest six energy structures for each concentration are taken as a compositional ensemble for further analysis.

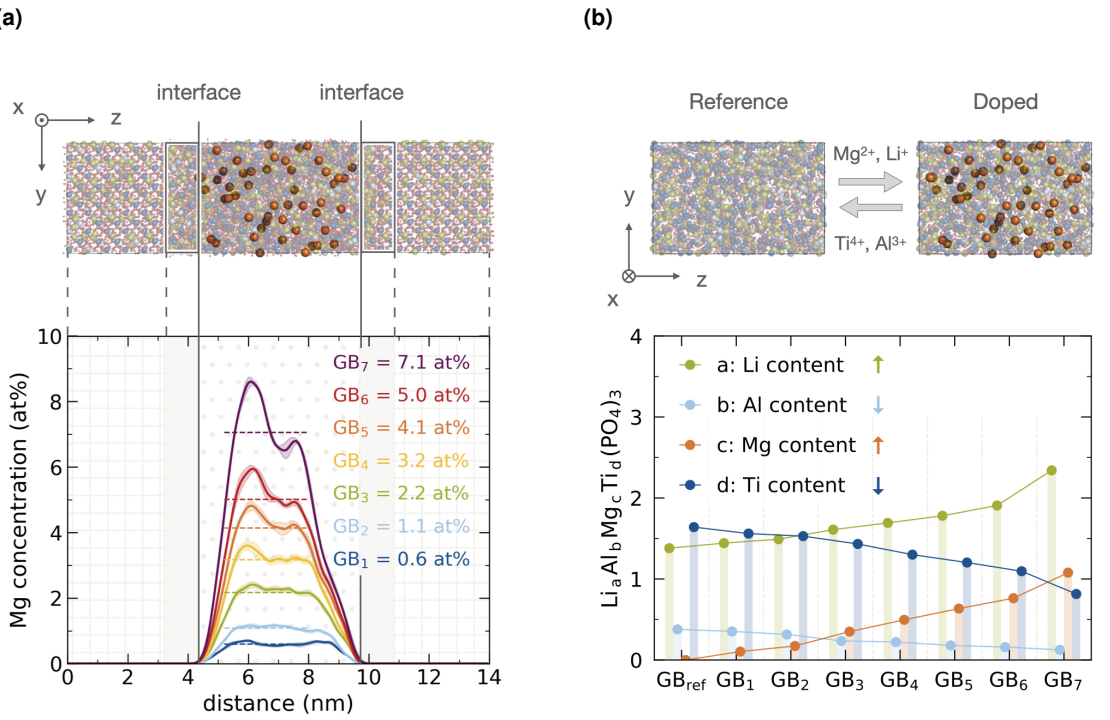

Figure 5.6: Initial Mg^{2+} interfacially doped LATP grain boundary structures. **(a)** Top: Atomistic structure with elemental colors chosen as Li ●, Mg ●, Al ●, Ti ●, O ●, and P ● (for emphasis Mg^{2+} is enlarged and other ions are transparent). Bottom: Corresponding Mg^{2+} profiles across the grain boundary for different doping concentrations $GB_1 - GB_7$. **(b)** Top: Amorphous bulk for the reference structure and an exemplary doped structure. Elemental colors, radii and opacity are adopted from **(a)**. Bottom: Cationic composition normalized to phosphate content according to $Li_aAl_bMg_cTi_d(PO_4)_3$ for $GB_1 - GB_7$. Images reproduced from Stegmaier et al. [2] under CC BY 4.0.

Substitution of Al^{3+} and Ti^{4+} ions for Mg^{2+} and Li^+ is performed following the reported APT profiles, cf. Figure 4.3 (c). The dopant profiles in Figure 5.6 (a) thus exhibit two local maxima like in the experimental data. The dopant concentration in the crystalline grain domains is set to zero to yield true interfacially doped initial structures.

Cationic compositions for the amorphous bulk in all doping models in $GB_1 - GB_7$ are shown in Figure 5.6 (b). A normalization to the amount of phosphate units ensures compositional comparability of the different doping concentrations with $Li_aAl_bMg_cTi_d(PO_4)_3$. The choice of a common reference structure GB_{ref} ensures consistent normalization. It follows from Equations (5.2) that both, the Mg^{2+} and Li^+ contents, are increased, while Ti^{4+} and Al^{3+} contents are decreased. By design, the highest doping concentration leads to a reduction

of higher valent ion content by a factor of two from $b_{GB_{ref}} = 0.4$ to $b_{GB_7} = 0.2$ for Al^{3+} and correspondingly $d_{GB_{ref}} = 1.6$ to $d_{GB_7} = 0.8$ for Ti^{4+}.

5.5 Dopant Bleeding into Grain Bulk Domain

Aging processes and ion diffusion lead to *bleeding* of the dopant into the crystalline grain domains. The initial spatial confinement of the dopant in the interphase may thus be lost over time, i.e. a fraction of the doping ions escape the intended interfacial engineering purpose.

Such dynamic processes take days, months and years of cycling in real time [265–267]. A direct simulation of these processes is therefore not possible since they exceed the computationally accessible time scales by multiple orders of magnitude. To assess possible interdiffusion processes across an interface via computational simulation, a sampling scheme based on MC statistics is employed.

5.5.1 Monte-Carlo Swapping Protocol

Türk et al. [173] have recently introduced a Monte-Carlo (MC) based swapping protocol to simulate interdiffusion of ions across an interface. This protocol is adopted and slightly adjusted to scrutinize bleeding of Mg^{2+} dopant from an amorphous grain boundary into adjacent LATP grains. The idea is to randomly swap Mg^{2+} with Ti^{4+}, Al^{3+}, or Li^{+} across an interface. A swap is accepted if the potential energy difference before and after swapping

$$\Delta E := E_{\text{after}} - E_{\text{before}} \tag{5.3}$$

is favorable, i.e. $\Delta E \leq 0$. If this is not the case, i.e. $\Delta E > 0$, a random number q is drawn from a normal distribution and the swap is accepted if $p > q$, where

$$p = \exp\left[-\frac{\Delta E}{k_{\mathrm{B}} T}\right]. \tag{5.4}$$

k_{B} is the Boltzmann constant and T is the system temperature. Since this is a stochastic process, multiple walkers with sampled doping structures are randomly initialized and run in parallel. In order to explore low and high energy configurations in a robust manner, configurations are exchanged at different temperatures as given by the replica exchange method [268, 269]. Swapping is performed layer-wise to mimic Fickian diffusion [173].

Figure 5.7 (a) schematically depicts an attempted swap of $Mg^{2+} \leftrightarrow Al^{3+}$ across the interface in the first swapping layer. A layer width of 3.5 Å is chosen, which corresponds to the z-distance between Ti/Al planes in the crystalline domain.

An NPT simulation is run after every 100 attempted swaps at 1000 K and 1 bar for 2 ps to ensure structural relaxation into local basins of the presumable shallow Potential Energy Surface (PES) and allow for the redistribution of Li^{+} to achieve local charge neutrality. A new swapping layer is added after 10 repetitions, i.e. a total of 1000 swaps per layer, to allow further penetration of Mg^{2+} into the grain. With a total of 15,000 attempted swaps, 15

swapping layers, and a total relaxation time of 300 ps, a region of ≈52.5 Å from the interface is explored. An exemplary energetic convergence of 12 randomly initialized walkers after applying the MC swapping protocol is shown in Figure 5.7 (b). The respective temperature profiles from the parallel tempering, i.e. replica exchange, is shown in Figure 5.7 (c). Walker simulations are initialized at equidistant temperatures in a regime between 1000 – 2000 K. Elevated temperatures are chosen to enhance dynamics, with an upper limit below the melting point of crystalline LATP. All walkers explore the full temperature regime in a robust manner.

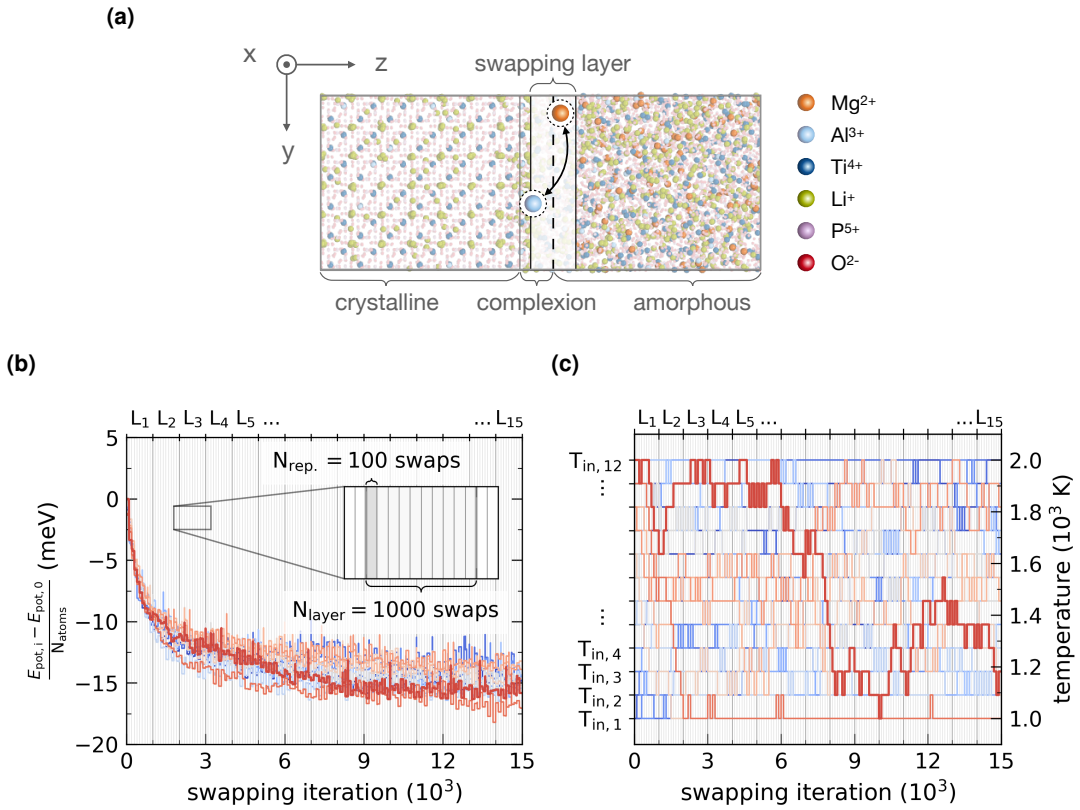

Figure 5.7: Schematic Monte-Carlo (MC) swapping protocol. **(a)** Interface structure with attempted swap of $Mg^{2+} \leftrightarrow Ti^{4+}$ across the interface in first swapping layer. **(b)** Exemplary energy profiles of 12 randomly initialized walkers. The potential energy of all walkers converges over the course of 15,000 attempted swaps. After $N_{\text{rep}} = 100$ swaps an NPT simulation is performed. After $N_{\text{layer}} = 1000$ swaps the swapping regime is extended by the next adjacent layer L_{i+1}. **(c)** Parallel tempering for the 12 exemplary walkers with different initial temperatures $T_{\text{in},i}$ in an equidistant range between 1000 – 2000 K. Images reproduced from Stegmaier et al. [2] under CC BY 4.0.

5.5.2 Mg^{2+} Penetration into LATP Grains

The normalized acceptance probabilities of a Mg swap for each cationic species Ti^{4+}, Al^{3+}, and Li^{+} averaged over the six lowest energy walkers from MC swapping is shown in Figure 5.8 (a). With an order of magnitude higher success rate, a preferential swapping of Mg^{2+} for Al^{3+}, as compared to Ti^{4+} and Li^{+} is observed. Acceptance probabilities of ≈6.41 – 9.36 % for Mg ↔ Al seem large, yet the absolute number of Mg^{2+} incorporated onto Al^{3+} sites in the crystal remains small due to the low Al^{3+} content in $Li_{1.3}Al_{0.3}Ti_{1.7}(PO_4)_3$. A decrease of Mg ↔ Al probabilities with increasing doping concentrations can be attributed to a normalization effect as the Al^{3+} content decreases. Only for higher doping concentrations, i.e. from GB_1 to GB_7, Mg^{2+} is swapped onto Ti^{4+} and Li^{+} sites with higher acceptance probability. From a thermodynamic perspective, the higher Mg ↔ Ti/Li success rates resemble an increased driving force due to a higher chemical potential of spatially confined Mg^{2+}.

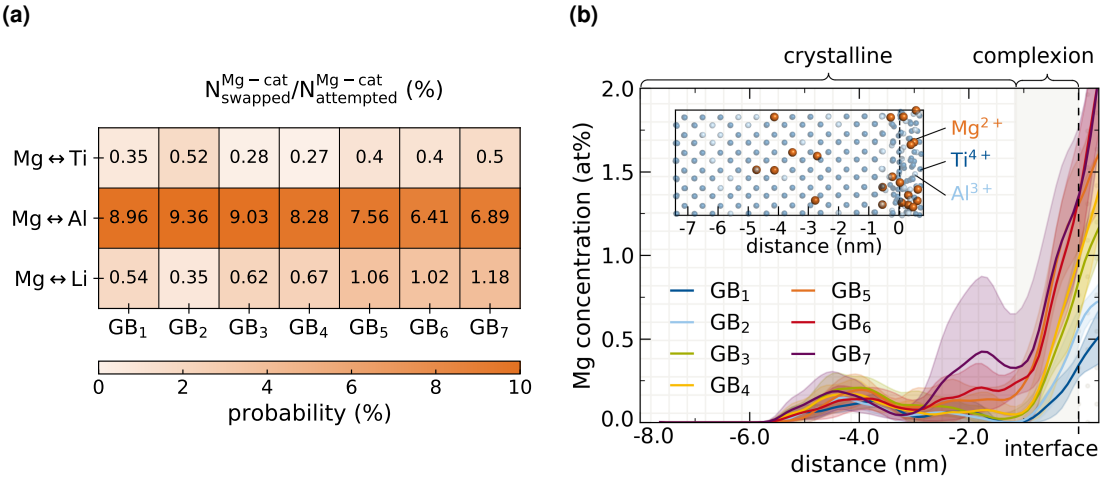

Figure 5.8: Penetration of Mg^{2+} into LATP grain from MC-protocol. **(a)** Normalized swapping acceptance probabilities for each Mg ↔ cation pair in all doping concentrations $GB_1 - GB_7$ according to $N^{Mg\text{-}cat}_{swapped}/N^{Mg\text{-}cat}_{attempted}$. **(b)** Mg^{2+} profiles across grain boundary after MC swapping averaged over the six lowest energy walkers of different doping concentrations. An exemplary atomistic substructure of crystalline Ti-Al framework with incorporated Mg^{2+} ions after swapping is added. Images reproduced from Stegmaier et al. [2] under CC BY 4.0.

The Mg-cation swapping acceptance probabilities are translated into quantifiable dopant bleeding from the Mg^{2+} concentration profiles across the studied interface as shown in Figure 5.8 (b). While the atomistic models feature two interfaces between the crystalline grain and the amorphous grain boundary, cf. Figure 5.6 (a), MC swapping is performed asymmetrically across only one interface. Since the crystalline bulk domain in the simulated system does not extend far enough, it is crucial to focus the bleeding analysis to one interface, in order to avoid overlapping of the Mg leakage from both sides. An extension of the system

size leads to significantly higher computational cost. For real systems, a symmetric dopant leakage at both interfaces is expected.

Figure 5.8 (b) shows a Mg^{2+} incorporation of ≈4 nm into the crystalline grain beyond the complexion. This nm-ranged penetration into the crystal lattice is considered a localized phenomenon, especially when compared to the cross section of physical LATP grains, which are typically in the µm-range [47, 270]. The Mg-profiles show a higher amount of Mg^{2+} bleeding into the crystal for higher doping concentrations. However, for each doping concentration $GB_1 - GB_7$, the amount of Mg^{2+} incorporated into the crystal is significantly lower than the amorphous bulk concentration. A relatively high success rate above 9 % for Mg ↔ Al in GB_1 does not necessarily result in higher Mg^{2+} concentration in the crystalline domain, as the MC protocol accounts for re-swapping into the amorphous bulk. As a result, the low atomic concentration translates into single Mg^{2+} ions swapped into the crystal lattice for $GB_1 - GB_4$. With values below 0.5 at% further into the crystal, the observed Mg^{2+} concentrations are within the impurity range as observed experimentally, cf. Figure 4.3 (c).

Mg-profiles retrieved from the MC swapping protocol consistently exhibit concentration minima around -3.1 nm and -1.1 nm from the swapping interface. These correspond to local concentration minima in the Al-profile of the underlying host reference system as shown in Figure 5.9. Since Mg^{2+} is preferentially swapped onto Al^{3+} sites, these characteristic features are adopted. An Al^{3+} depletion beyond the complexion is a result of local Ti-Al segregation, which is characteristic for the complexion, cf. Section 4.4.4.

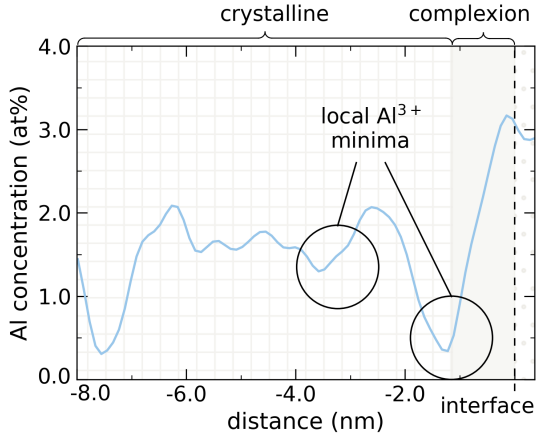

Figure 5.9: Al concentration profile of the undoped reference system with local concentration minima at -1.1 nm and -3.2 nm from the interface. These local minima are observed for the dopant bleeding in Figure 5.8 (b), as Mg^{2+} preferentially occupies former Al^{3+} sites. Images reproduced from Stegmaier et al. [2] under CC BY 4.0.

From the MC swapping protocol, minimal bleeding of Mg^{2+} into the crystalline LATP domain is observed. This holds even at high doping concentrations, thus meeting the first postulated requirement for successful interfacial engineering.

5.6 Doping Implications on Crystalline Bulk

Though the quantitative amount of Mg^{2+} bleeding into the LATP crystalline grain is low, the overall SSE performance may be drastically affected by a thin surfacial region with high ionic impedance. Therefore, the implications of dopant leakage into the LATP lattice is scrutinized in terms of structural integrity and diffusive behavior of the bulk LATP grain.

Two conceptually different aspects need to be differentiated when Mg^{2+} penetrates into the host framework. First, Mg^{2+} is substituted into the immobile host structure, i.e. the Ti/Al framework, which may affect the structural integrity. And second, Mg^{2+} penetrates into the Li charge carrier pathways, which leads to clogging of the LATP inherent channels.

Figure 5.10 (a) depicts a crystalline LATP structure with possible lattice sites for Mg^{2+} incorporation. A site analysis of the crystalline domain after MC swapping is shown in Figure 5.10 (b) for each doping concentration $GB_1 - GB_7$. The dopant predominantly occupies former Al^{3+} and Ti^{4+} sites and with rising doping concentration, i.e. $GB_3 - GB_7$, Li channels are starting to get infiltrated with $11 - 40\,\%$ of the total migrated Mg^{2+} in the crystal. In agreement with the normalized swapping acceptance probabilities, cf. Figure 5.8 (a), the dopant preferentially occupies former Al^{3+} sites, especially for low doping concentrations. Despite lower acceptance probabilities for Ti^{4+} and Li^{+}, their higher amount in stoichiometric LATP leads to an incorporation of Mg^{2+} into these sites.

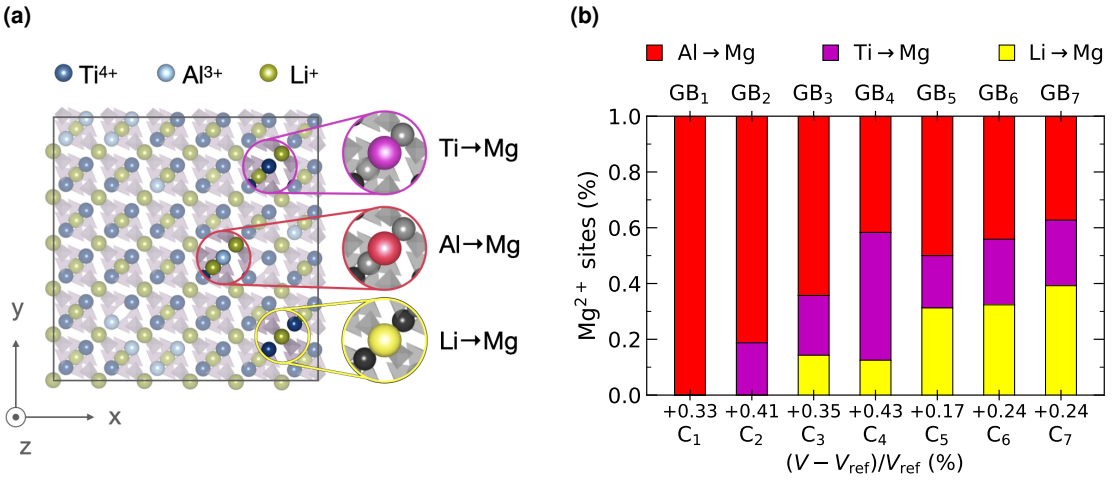

Figure 5.10: Crystalline LATP bulk with incorporated Mg^{2+} from dopant bleeding. **(a)** Atomistic structure of reference crystal LATP cell with possible Mg^{2+} swapping sites. **(b)** Composition of Mg^{2+} site occupancy in crystal lattice after MC swapping for different doping concentrations $GB_1 - GB_7$ in the grain boundary structures. Swapping colors are chosen as $Mg^{2+} \rightarrow Al^{3+}$ ■, $Mg^{2+} \rightarrow Ti^{4+}$ ■, and $Mg^{2+} \rightarrow Li^{+}$ ■. The relative volume change $(V_i - V_{\text{ref}})/V_{\text{ref}}$ in percent, for the correspondingly doped crystal structures $C_1 - C_7$ is shown on the abscissa. Images reproduced from Stegmaier et al. [2] under CC BY 4.0.

Structural destabilization of the host LATP framework upon insertion of Mg^{2+} is expected to be unlikely. This is due to a similar effective ionic radius of Mg^{2+} with 72.0 pm [258] and Ti^{4+} with 74.5 pm [258]. Additionally, the small amount of actual dopant bleeding does not support severe implications on the underlying LATP lattice framework.

In order to substantiate this hypothesis, a crystalline LATP cell is doped with Mg^{2+} and the volume change is monitored after structural relaxation. A reference crystalline cell C_{ref} is cut containing 3953 atoms. The absolute number of Mg^{2+} atoms doped into these cells is retrieved from summation over the concentration profile in the crystalline domain of the lowest six energy walkers for each doping concentration, cf. Figure 5.8 (b), according to $\sum x_{Mg} \cdot N_{C_{ref}}^{total} = N_{Mg}$. The Mg^{2+} atoms are distributed onto respective lattice sites following the composition as shown in Figure 5.10 (b). The resulting doped crystalline structures for each concentration $C_1 - C_7$ are equilibrated at 300 K and 1 bar for 100 ps. A maximum volume expansion of + 0.43 % is observed for C_4 as compared to the undoped reference LATP cell with $(V_i - V_{ref})/V_{ref}$. The observed volumetric changes when incorporating Mg^{2+} into the LATP host with values below 0.5 % support the hypothesized structural integrity. Other computational and experimental works corroborate that Mg^{2+} doping into NASICON-type electrolytes does not lead to structural destabilization [262, 271]. In fact, doping of even larger ions, such as In^{3+} with an ionic radius of 80.0 pm [258], into LATP has been suggested to stabilize the electrolyte [272].

Interconnected 3D diffusion pathways [120, 273] facilitate fast Li^+ conduction in bulk LATP [47]. When Mg^{2+} penetrates into these channels, the charge carrier migration routes may be clogged. To investigate the implications of dopant bleeding on charge carrier pathways, 2 ns MD simulations at 700 K are conducted of the doped crystalline LATP structures $C_1 - C_7$.

A qualitative assessment of the impact of doped Mg^{2+} on Li^+ migration is shown in Figure 5.11. The atomistic structure on the left illustrates the position of three Mg^{2+} in crystalline LATP, corresponding to a doping concentration C_4. The Li positions of the full 2 ns trajectory are collapsed into the same structure to retrieve the interconnected pathways from the Li^+ isosurface. The first Mg^{2+} is doped onto a former Li^+ site (● $Mg^{2+} \rightarrow Li^+$), the second on a former Al^{3+} site (● $Mg^{2+} \rightarrow Al^{3+}$) and the third on a former Ti^{4+} site (● $Mg^{2+} \rightarrow Ti^{4+}$).

Subtraction of the respective isodensity from MD simulation of the undoped reference system C_{ref} reveals local Li^+ depletion and enrichment. A negative change, i.e. depletion of Li^+ density, around Mg^{2+} inserted into a Li^+ channel suggests local clogging of the interconnected pathways. Intriguingly, a positive change, i.e. enrichment of Li^+ density, is observed around both, the Mg^{2+} doped onto a Ti^{4+} and Al^{3+} site. Local ion *trapping* of charge carriers around cationic constituents *X* doped onto the Ti framework of L*X*TP has been reported by experimental [274] and first-principle [275] studies. It is attributed to minor distortions of the LiO_6 octahedra arising from a difference in ionic radius of *X*. Another reason for local enrichment of Li^+ density is the electrostatic imbalance upon aliovalent doping. By doping higher valent Ti^{4+}/Al^{3+} with divalent Mg^{2+}, formally negatively charged defects of the host lattice, $\Delta q_{Mg^{2+} \leftrightarrow Ti^{4+}} = -2$ and $\Delta q_{Mg^{2+} \leftrightarrow Al^{3+}} = -1$, are compensated by the density of mobile charge

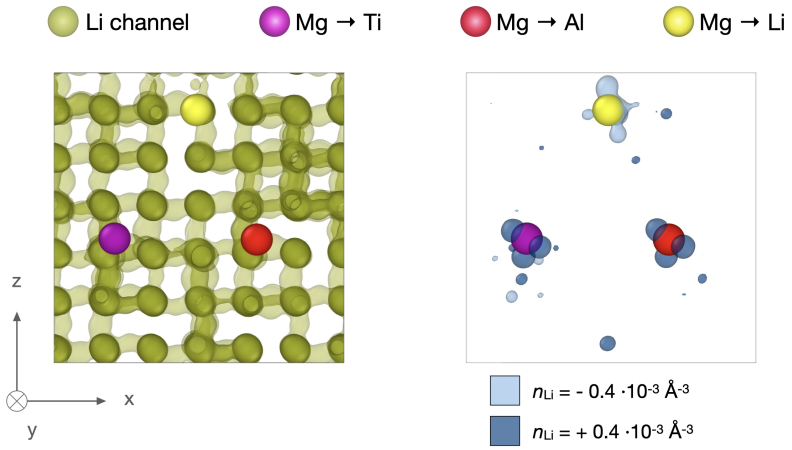

Figure 5.11: Qualitative implications of Mg^{2+} incorporation on Li^+ pathways. Left: C_4 atomistic structure showing doped Mg^{2+} ions on former Li^+ ●, Al^{3+} ●, and Ti^{4+} ● site. Li^+ ions of a 2 ns MD trajectory at 700 K are collapsed into the same structure to illustrate 3D interconnected pathways ●. Right: Li density difference of doped and undoped reference structure showing Li^+ avoiding the channel with doped Mg^{2+} at a number density of □ $n_{Li} = -0.4\,10^{-3}$Å^{-3} and Li^+ being trapped around Mg^{2+} on Ti/Al sites with a number density of ■ $n_{Li} = +0.4\,10^{-3}$Å^{-3}. Images reproduced from Stegmaier et al. [2] under CC BY 4.0.

carrier. The short NPT simulations in the MC swapping protocol, cf. Section 5.5.1, ensure Li^+ redistribution around these defects.

Qualitative analysis therefore suggests clogging of Li^+ diffusion pathways for $Mg^{2+} \leftrightarrow Li^+$ and ion trapping for $Mg^{2+} \leftrightarrow Ti^{4+}/Al^{3+}$. However, the effect on Li^+ density changes seems to be localized within the 3D ion channel network for both scenarios.

For a quantitative assessment of how such local trapping of charge carriers and clogging of the respective pathways affects the overall electrolyte performance, cationic Li^+, Mg^{2+}, Al^{3+}, and Ti^{4+} conductivities from the 2 ns MD trajectories are shown in Figure 5.12. Mg^{2+} conductivities are visualized separately for different site occupancies. Macroscopic conductivities are obtained from the Nernst-Einstein relation, cf. Section 3.4.

The mobility of Mg^{2+} inserted into the immobile Ti/Al framework (●) is by 6 – 7 orders of magnitude lower than Li^+ and in a similar regime as the respective Ti^{4+} (●) and Al^{3+} (●) conductivities on the same lattice site. While the Mg^{2+} ions doped into the Li-channels (●) are significantly more mobile than on the rigid host lattice, the computed conductivity is still 2 – 3 orders of magnitude lower as compared to the Li^+ conductivity. Thus, even at 700 K, Mg^{2+} is virtually immobile and not expected to penetrate further into the grain with electrolyte aging. As can be seen from the Li^+ conductivity (●), the electrolyte performance in terms of charge carrier mobility is not significantly affected. While generally bleeding of the dopant does lead to a decrease in Li^+ conductivity, the local effect on migration pathways leads to

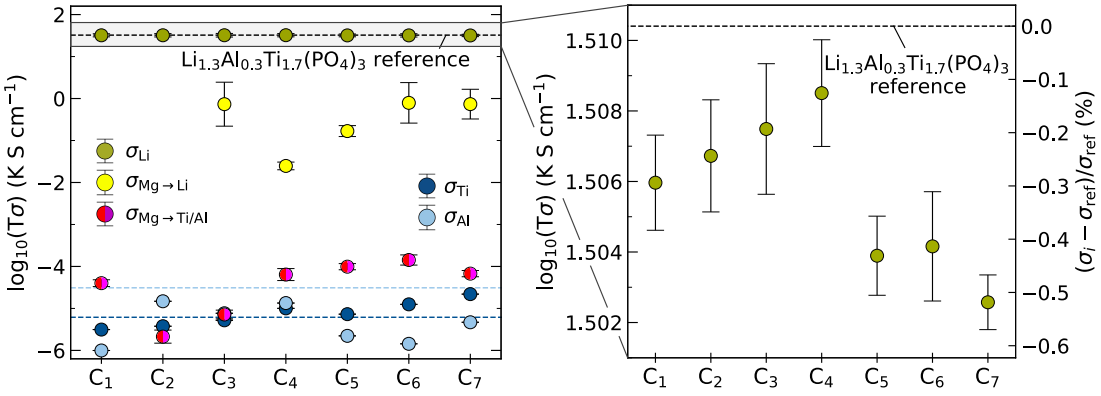

Figure 5.12: Quantitative implications of Mg^{2+} bleeding on ion diffusion. Li^+, Mg^{2+}, Al^{3+}, and Ti^{4+} conductivities as determined from MD simulations at 700 K for the doped $C_1 - C_7$ derived from MC swapping. Mg^{2+} conductivities are shown separately for different site occupancies. For the lowest two doping concentrations C_1 and C_2, no Mg^{2+} is incorporated onto Li^+ sites, hence there is no conductivity value for these configurations. Li^+ conductivities are compared to undoped bulk LATP reference C_{ref}. Images reproduced from Stegmaier et al. [2] under CC BY 4.0.

a decrease of -0.51 % as compared to the reference conductivity. The implications on Li^+ mobility do not follow a linear trend with higher bleeding concentrations, i.e. from C_1 to C_7.

5.7 Interphase Modifications via Aliovalent Doping

While the requirements of local dopant confinement and an intact electrolyte bulk render Mg^{2+} a suitable candidate, engineering efforts need to by justified by an improvement of desirable features. Therefore, the effect of interphase modifications on the bulk phase of a LATP grain boundary is scrutinized with respect to structural features and dynamic behavior.

Smaller, purely amorphous cells are cut from the multi-phase structures to arrive at manageable computational cost. The slabs are centered in the grain boundary region and slightly modified to yield charge neutral and 3D periodic structures. Figure 5.13 (a) depicts the corresponding atomistic structure of the reference amorphous bulk A_{ref} cut from GB_{ref}.

Analogous cutting of the amorphous domain of the six lowest energy walkers after MC swapping from $GB_1 - GB_7$ yields the amorphous cells $A_1 - A_7$ each comprising 3430 – 3900 atoms. To visualize the sampled design space of the six element LAMTP system, a relative composition is defined by normalizing to the heavier cations Ti^{4+}, Al^{3+}, and Mg^{2+} as

$$x_{el} = \frac{N_{el}}{\sum[N_{Ti}, N_{Al}, N_{Mg}]}. \tag{5.5}$$

The Li^+ content is dictated by these cations to maintain charge neutrality, as a common underlying reference is used. The resulting relative compositions for A_{ref} and $A_1 - A_7$ are

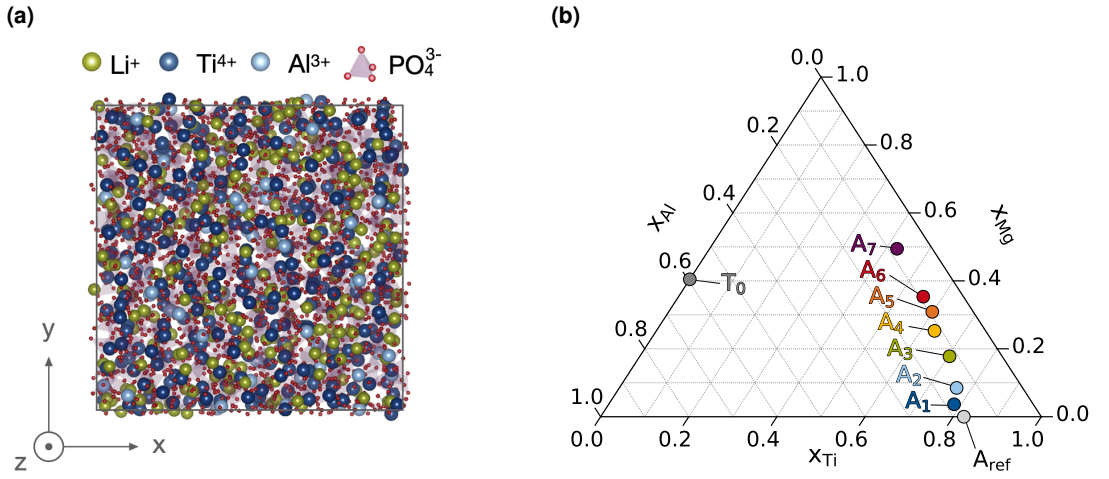

Figure 5.13: Reference amorphous structure and relative composition of doped cells. **(a)** Atomistic structure of the reference cell A_{ref}. Elemental colors are chosen as Li ●, Al ●, Ti ●, O ●, and P ●. **(b)** Ternary plot showing relative composition for A_{ref}, $A_1 - A_7$, and a completely Ti^{4+} depleted T_0 according to $x_{el} = N_{el} / \sum[N_{Ti}, N_{Al}, N_{Mg}]$. Images reproduced from Stegmaier et al. [2] under CC BY 4.0.

shown in Figure 5.13 (b). Following the cationic substitutions chosen in Equations (5.2), an increase in dopant concentration x_{Mg} leads to a decrease in x_{Al} and x_{Ti}. As an upper doping limit, the Ti^{4+} concentration is reduced to approximately half the reference amorphous content, i.e. from $x_{Ti}^{A_{ref}} = 0.82$ to $x_{Ti}^{A_7} = 0.42$.

Theoretically, a complete removal of Ti^{4+} from the interphase is desirable in order to minimize electronic conductivity via polaron hopping. Therefore, one further doping configuration T_0 is constructed, where the reference amorphous bulk is doped with Mg^{2+} to exchange all Ti^{4+} to test such an extreme case. Since Mg^{2+} generally shows a higher mobility, the amount of redox stable Al^{3+} is increased to maintain the solid nature of the amorphous phase.

5.7.1 Dopant Impact on Structural Features

The observed dendrite suppression capability of LATP can be ascribed to a local separation of TM centers in a nano-scale complexion forming at the interface between grain and grain boundary [1]. Dendrite growth and penetration through the grain boundary network can be associated with a high residual local electronic conductivity [29, 33, 276]. To suppress slow degradation processes, a minimization of residual electronic conductivity in the amorphous interphase is thus desirable. First-principles studies [1], as well as experimental reports [249] on LATP suggest a preferential localization of excess electrons in proximity of the Ti^{4+}. The formation of small polarons facilitates electronic conduction in this ceramic insulator [241–243]. Due to an exponential dependence on the width and height of the polaron hopping barrier, this mechanism is sensitive to Ti-Ti nearest-neighbor (NN) distances.

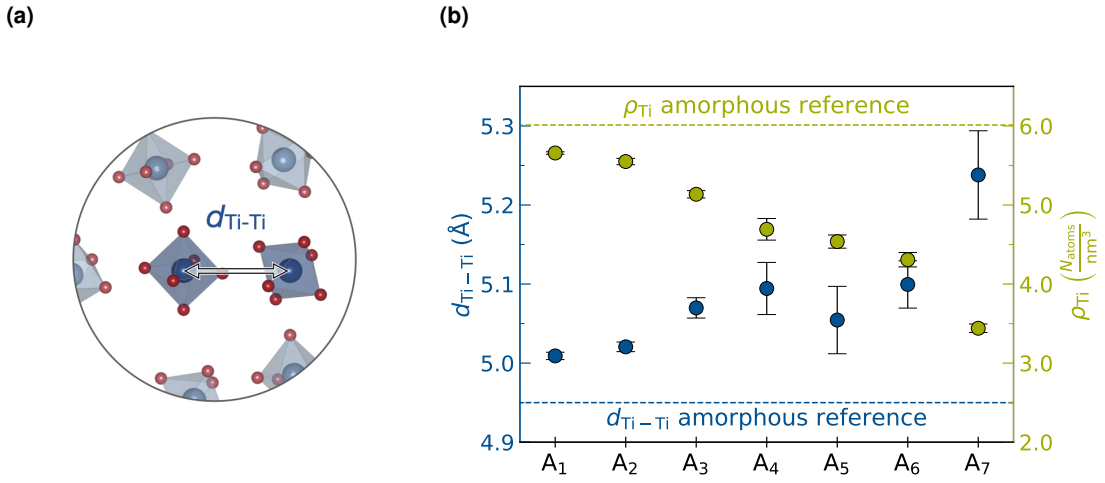

Figure 5.14: Effect of Mg^{2+} doping on Ti^{4+} distribution. **(a)** Schematic atomistic structure depicting Ti-Ti nearest-neighbor distance $d_{\text{Ti-Ti}}$. Elemental colors are chosen as Ti ● and O ●. **(b)** $d_{\text{Ti-Ti}}$ as a function of doping concentration $A_1 - A_7$ (darkblue) and respective Ti atom density ρ_{Ti} averaged over six lowest energy walkers defined as $N_{\text{Ti}}/V_{\text{cell}}$ (green). Images reproduced from Stegmaier et al. [2] under CC BY 4.0.

In Figure 5.14 (b) the Ti-Ti NN distance $d_{\text{Ti-Ti}}$ is shown to increase with higher doping concentration for $A_1 - A_7$. A Ti-Ti NN distance of 5.24 Å is observed for the highest doping concentration A_7, which is 0.3 Å larger than in the reference amorphous bulk with a distance of 4.95 Å [1]. Aliovalent doping with Mg^{2+} to deliberately reduce Ti^{4+} centers is expected to impose an anisotropic impedance that reduces electronic conduction via polaron hopping.

5.7.2 Non-trivial Effects with Doping Concentration

As depicted in Figure 5.14 (b), the increase in Ti-Ti NN distance is not strictly monotonous or linear with doping concentration. The dip for A_5 is reflected to a lesser extent in the Ti atom density ρ_{Ti}.

While the substitutions in Equations (5.2) lead to a steady increase of the total number of atoms with higher Mg^{2+} content, the equilibrated cell volumes of the underlying systems do not necessarily correlate linearly with this atom count. As a result, the total atom density shown in Figure 5.15 (b) exhibits a non-linear trend going from A_1 to A_7. In contrast, the mass density shown in Figure 5.15 (a) is monotonously decreasing since $m_{\text{Ti}} > m_{\text{Mg}} + 2m_{\text{Li}}$.

Due to a higher Al^{3+} content in T_0, which is needed to maintain structural integrity, the mass density is increased. For charge compensation, replacing tetravalent Ti^{4+} by Mg^{2+} and Al^{3+}, leads to the introduction of excess Li^+ and a concomitant increase of the T_0 atom density. In particular for highly amorphous phases, predictions based on extrapolation of trends alone require more detailed investigations.

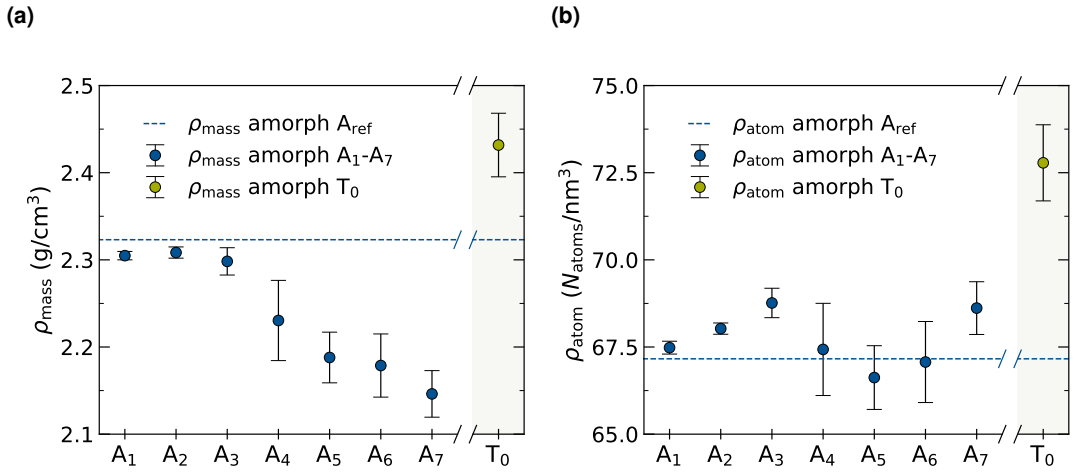

Figure 5.15: Non-linear density effects upon doping the amorphous phase with Mg^{2+}. **(a)** Mass density $\rho_{mass} = \frac{\sum_i^N m_i}{V_{cell}}$ obtained after NPT equilibration at 700 K and 1 bar for doped amorphous cells $A_1 - A_7$ and completely Ti^{4+} depleted T_0. **(b)** Respective total atom densities $\rho_{atom} = \frac{\sum_i^N \text{atoms}}{V_{cell}}$. Images reproduced from Stegmaier et al. [2] under CC BY 4.0.

5.7.3 Dopant Impact on Ion Dynamics

With a multiple orders of magnitude lower Li ionic conductivity Mertens et al. have identified the grain boundary as a bottleneck to charge carrier diffusion in LATP [47]. However, the reported conductivity is not necessarily inherent to the nature of the grain boundary phase itself. Instead, poor interfacial contacting from mechanical cracks or the formation of insulating secondary phases may severely impede ionic diffusion [96, 165]. Quantifying the contribution from such microstructural defects is experimentally difficult due to the inherently small length-scale. While MD simulations of the established grain boundary model in Chapter 4 do not support an orders of magnitude difference, cf. Figure 4.22 (a), even in these idealized models, the amorphous bulk phase exhibits lower Li ion conductivity [1].

To investigate the effect of aliovalent doping on the interphase ionic diffusion, MD simulations are conducted at 700 K for 2 ns for each amorphous bulk structure. Resulting Li^+, Mg^{2+}, Al^{3+}, and Ti^{4+} conductivities as obtained from conversion of atomistic MSDs via the Nernst-Einstein formalism, cf. Section 3.4, are shown in Figure 5.16 (a).

All Mg^{2+} doped amorphous bulk cells exhibit a higher Li^+ conductivity by 22 – 38 % as compared to the undoped reference system. As suggested by Mertens et al. [47], a higher local Li concentration in the amorphous interphase seems to be an effective measure to improve grain boundary charge carrier conductivity. Resembling the non-trivial effects of doping on structural features, the increase in Li^+ conductivity does not correlate linearly with the doping concentration.

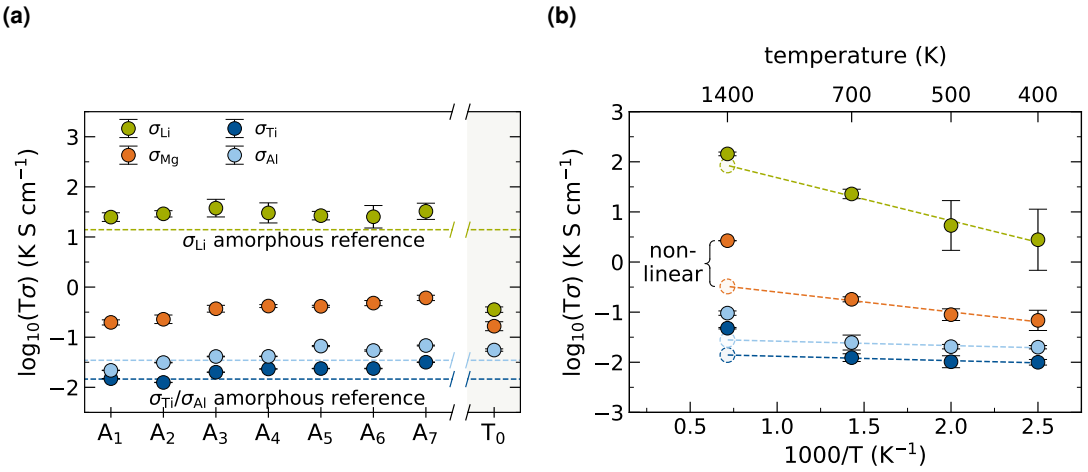

Figure 5.16: Ion conductivities of Mg^{2+} doped amorphous bulk cells. **(a)** Li^+, Mg^{2+}, Al^{3+}, and Ti^{4+} conductivities as determined from 2 ns MD simulations at 700 K for amorphous bulk model ensembles $A_1 - A_7$. The dashed lines indicate respective reference conductivities obtained from A_{ref}. Respective cationic conductivities of a doping realization T_0, i.e. completely depleted of Ti^{4+}, are shown in the right panel. **(b)** Arrhenius-type plot for cation conductivities in A_4 as determined from 2 ns MD simulations at 400 K, 500 K, 700 K, and 1400 K, respectively. Images reproduced from Stegmaier et al. [2] under CC BY 4.0.

The Mg^{2+} mobility is about two orders of magnitude lower than Li^+. While this is a significant difference, the trend suggests an increasing Mg^{2+} mobility with higher doping concentration. For interfacial engineering, however, the dopant needs to stay locally confined in the interphase regime. As it is not straight-forward to extrapolate such trends, dopant mobility at higher concentrations of Mg^{2+} needs to be monitored.

A complete depletion of Ti^{4+} ions in the T_0 configuration leads to a drastic decrease of Li^+ conductivity by two orders of magnitude. This no longer facilitates sufficient charge carrier diffusion required for a Li conducting bulk phase of an electrolyte. The overall effect on performance, however, also depends on the thickness of the interphase. The formation of secondary phases, i.e. Al-phosphates or Mg-phosphates, which virtually do not contribute to charge carrier conduction, may lead to such a drop in Li ion conductivity. It has been shown experimentally, that an $AlPO_4$ secondary phase in LATP significantly impairs overall performance [96]. Welsch et al. [277] have pointed out that Li^+ cation mobility in Li-Mg-phosphate glass networks is severely constraint. A complete depletion of Ti^{4+} in the amorphous interphase, as realized in the presented stoichiometry, is thus not a viable candidate for interfacial engineering. Other compositions of completely depleted Ti^{4+} in the multidimensional phase space may exhibit less drastic effects. Generally, a low Ti^{4+} content while maintaining a sufficient thin film Li^+ conductivity is highly desirable and should be explored in further detail.

The conductivity for both, Al^{3+} and Ti^{4+} increases marginally from the reference value with higher doping concentration and is about 3 orders of magnitude lower than the Li^{+} conductivity, cf. Figure 5.16 (a). The amorphous systems hence maintain a solid character even at 700 K. While this is generally required for a solid state electrolyte under operating conditions, during high temperature synthesis, i.e. sintering, the interphase is heated up just below the melting temperature. The quasi-liquid state ensures sufficient mobility to yield dense interphases and satisfying contacting between phases. To validate a higher ion mobility in the sintering temperature regime, cation conductivities of A_4 retrieved from 2 ns MD simulations at 400 K, 500 K, 700 K, and 1400 K are shown in Figure 5.16 (b). Mg^{2+}, Al^{3+}, and Ti^{4+} mobilities exhibit a non-linear behavior at 1400 K, suggesting sufficiently high ion dynamics of the otherwise immobile host system, which is needed for electrolyte processibility.

5.8 Summary

The realistic atomistic LATP model obtained from a combined simulation-experiment approach, cf. Chapter 4, hosts an extended grain boundary with structurally different phases. Adjacent crystalline bulk grains are encapsuled by a protective nano-scale complexion with distinct structural and chemical features. The extended bulk interphase is highly amorphous and differs from stoichiometric LATP, as confirmed from APT analysis.

Intrigued by an experimentally observed local accumulation of cationic impurities in the grain boundary bulk, active interfacial engineering via aliovalent doping is investigated from a computational perspective. Divalent Mg^{2+} is found to be a promising interfacial doping candidate, as it stays mostly locally confined in the interphase thus not impairing overall bulk LATP performance. A concomitant compositional change toward lower valent cations, i.e. local depletion of Ti^{4+} and enrichment of Li^{+}, improves interfacial conductivity while exploiting the protective nature characteristic to the grain boundary motifs [1].

Doped grain boundary structures are constructed by local charge neutral substitution of higher valent cations to enrich the amorphous bulk phase with Mg^{2+} and, in particular, deplete it of the problematic Ti^{4+}. Seven different doping concentrations are realized which enter a MC swapping protocol, as adopted from Türk et al. [173], based on replica exchange to enhance statistical sampling simulating dopant bleeding from cell aging. The resulting energetically most favorable six walkers for each doping concentration are further investigated.

From the MC analysis, it is found that Mg^{2+} does not bleed heavily into the adjacent crystalline grain domain. Even at high doping concentrations the penetration distance is limited to a few nanometers with dopant concentrations below 0.5 at% in the crystal lattice. Mg^{2+} preferentially swaps onto former Al^{3+} sites and is mostly incorporated into the Ti/Al host framework. Only at higher doping concentrations the defined Li channels are starting to get infiltrated with Mg^{2+}. Qualitatively, the dopant leakage leads to clogging of the charge carrier migration pathways, as well as trapping of Li^{+} in proximity to the doped Mg→Al/Ti sites. However, these effects are extremely local and MD simulations confirm the overall Li

ion conductivity in the crystal bulk to remain intact due to the LATP inherent interconnected 3D diffusion network.

Aliovalent doping of a LATP grain boundary with Mg^{2+} thus appears as a successful interfacial engineering route, as the interphase modifications lead to local improvement of interphase properties. Structural analyses on the doped amorphous bulk suggest the reduced Ti^{4+} content may lead to lower residual electronic conductivity, thus protecting the electrolyte from Li dendrite penetration through the grain boundary network. An increased Ti-Ti nearest-neighbor distance with higher doping concentration hampers electronic conduction via polaron hopping from one TM center to the next. Ion dynamics retrieved from MD simulations further suggest an improved local charge carrier conductivity which is attributed to a local enrichment of Li^{+} in the amorphous bulk.

A doping realization completely depleted of Ti^{4+} is studied to potentially maximize the advantageous effects of interfacial doping. However, this particular amorphous composition exhibits a drastic drop in charge carrier conductivity which no longer qualifies as a conducting phase for a Li^{+} based electrolyte. A possible explanation is the mixed formation of ionically insulating secondary phases of Al-phosphate and Mg-phosphate glasses, which requires further studies of the Li/Mg/Al/P/O phase diagram and glass-ceramic phases therein.

The analyzed interphase properties, e.g. Ti-Ti distances and conductivities, neither show a strictly linear nor monotonous behavior with increasing doping concentration. The effect of compositional changes when doping the complex quinary LATP system can thus not be predicted or extrapolated in a straight-forward fashion. Instead, non-trivial effects such as density changes and generally known formation of secondary phases [96] need to be taken into account.

6 Conclusion and Outlook

To progress in making ASSBs a technological reality, interfacial challenges need to be overcome which often result in cell failure or severe performance loss. Especially the formation of metallic dendrites at solid-solid interfaces and the penetration of the SSE grain boundary network needs to be controlled. While the exposed electrolyte/electrode interface is more easily amenable to engineering approaches, buried solid-solid interfaces within the SSE bulk are hardly accessible in experiment. Computer simulations are therefore crucial to resolve the structural and chemical nature of working interfaces in SSEs at an atomistic scale. Merely by gaining a deeper mechanistic understanding of the role of such interfaces, a targeted design can be actively engineered. The predictive power of computational analyses, however, largely depends on the validity of the underlying atomistic model to accurately represent the real system.

In this thesis, a joint experiment-theory approach is pursued yielding a complex multi-phase atomistic model of an extended grain boundary in the LATP SSE with hitherto unmatched precision. Structural information retrieved from TEM measurements and a cross-interface chemical composition obtained from APT experiments enter into a herein established computational sintering protocol. MD simulations are performed employing a classical force field, which has been parameterized and validated against higher level theory DFT data. Structurally, the resulting models exhibit two bulk domains, i.e. crystalline LATP grains and a glass-amorphous grain boundary phase. As indicated by experimental TEM images, the computational structures verify the formation of distinct complexions which encapsulate the LATP grains. With an introduced rolling 2D Fourier analysis of the underlying Ti-Al framework, the complexion widths are found to be self-limiting irrespective of the extent of adjacent bulk phases. Ion dynamic analyses suggest neither the amorphous grain boundary bulk, nor the complexion to present a material inherent diffusion bottleneck. An experimentally observed orders of magnitude impeded conductivity can thus be ascribed to microstructural defects such as poor contacting. Chemically, as suggested from APT profiles, an energetically favorable elemental separation leads to local enrichment of Al^{3+} at the grain surface and concomitant Ti^{4+} depletion in the complexion. Electronic structure calculations reveal a localization of residual electronic density mainly on subsurface Ti^{4+}. This spatial separation of mobile Li^{+} in the grain boundary and free electrons at the nanoscale suffices to effectively suppress dendrite nucleation. The herein acquired insights add to a simplified picture of electrolyte performance indication based on solely macroscopic bulk properties.

The established atomistic model serves as basis for active interfacial engineering via aliovalent doping. Encouraged by APT findings, Mg^{2+} is doped locally into the amorphous bulk domain to deliberately reduce Ti^{4+} content while locally increasing the charge carrier concentration. An adopted MC based protocol utilizing replica exchange of randomly initialized walkers is employed to simulate dopant interdiffusion into the crystalline bulk domain. Minimal bleeding into the adjacent grain is observed even at higher doping concentrations, leaving the LATP inherent 3D interconnected charge carrier migration pathways largely unaffected. With no severe compromising of the bulk crystalline LATP performance, interfacial aliovalent doping of Mg^{2+} can be used to engineer the LATP grain boundaries. Capitalizing on the protective nature of the previously found complexions, a local Ti^{4+} reduction in the amorphous phase further minimizes residual electronic conductivity from polaron hopping. Additionally, a local enrichment of Li ions improves the domain conductivity in the grain boundary bulk. A confident prediction of promising doping stoichiometries is however not straight-forwardly possible from theoretical considerations alone. Non-trivial effects with doping concentration require further experimental input. This accentuates the need for a combined approach from both, theory and experiment, to efficiently advance in the realization of high performance energy materials.

Conceptually, this work presents a generic approach for the construction of complex realistic grain boundaries in glass-ceramic energy materials. The established computational sintering protocol itself is universal and in principle transferable to other grain-grain interphases. However, the exact parameters for the simulation workflow of both, model construction and sintering, need to be reevaluated for each individual case. To characterize complex multiphase interfaces on an atomistic-scale, a novel measure to quantify the degree of amorphization based on Fourier transformation is presented. Such an analysis is applicable to any system with varying residual structure. A novel computational approach is adopted to actively engineer the interphase composition and assess the suitability of a specific dopant for the realistic grain boundary model. The introduced methods are not limited to the specific case of grain boundaries in LATP, but may help understand the nature of buried solid-solid interfaces and consequently engineer them also in other material classes.

For a future design of functional buried interfaces, current *ab initio* approaches need to be extended to include nano-sized motifs, which better represent realistic systems. Mapping of such motifs into computationally manageable cells may be achieved via inverse design using artificial neural networks [278]. A targeted design of solid-solid interfaces is especially promising in LATP due to its high chemical stability. Its chemical inertness against contact with water and air may facilitate the coating of LATP grains with predicted stoichiometries. Possible synthesis routes may be Atomic Layer Deposition (ALD) as established for electrolyte/electrode interfaces [279–281], or wet impregnation of mother powder as performed in the fabrication of electrodes in solid oxide fuel cells [282]. For an experimental realization, however, the vast design space of possible interphase compositions needs to be narrowed to a few confidently predicted candidates. Non-trivial effects upon doping render simple large-scale candidate screening ineffective. Instead, a multi-objective adaptive DOE or Bayesian optimization ansatz is needed as a powerful tool toward active interfacial engineering.

Acknowledgments / Danksagung

First and foremost I want to thank Prof. Dr. Karsten Reuter for all the support during my PhD. I am very thankful for your constant encouragement to participate in the international scientific community during conferences and especially for facilitating the research visit in Prof. Dr. Kozinsky's group at Harvard University. You have always fostered an environment for creative scientific discourse and preserved a strong team spirit even during socially challenging years. This is probably a good time to admit: yes, you told me so; I have missed the group dearly and enjoyed every visit to the gorgeous FHI estates.

Similarly, I want to thank Dr. Christoph Scheurer for his supervision and mentoring. You always provided guidance when needed and pointed me in the direction that led to this thesis – though it usually took me half a year to follow your lead. Beyond the scientific scope, I am grateful for your tireless efforts to build up my courage and figuratively "holding my scientific hand" when I was in self-doubt.

Additionally, I want to express my gratitude to Prof. Dr. Jennifer Rupp for taking the time and effort to co-examine my dissertation.

I further want to thank Prof. Dr. Boris Kozinsky and the entire MIR group at Harvard University for being so welcoming and hospitable during my research visit. Owing to the very collaborative atmosphere in Pierce Hall 305 I have learned incredibly much during my stay.

Moreover, I want to thank the IT-team for helping me with my limited technical capabilities. Thank you Simeon, Martin, Simon W., Matthias, xhristoph and David for your support and patience that extended beyond the Atlantic Ocean and the considerable time shift. Thank you also to Ruth for always helping me in my constant battle with German bureaucracy. Likewise, I highly appreciate the organizational help of Julia with my visits to the FHI.

I would have never made it this far without sharing this journey with such great colleagues who have become friends over the years. A special shout out goes to (little) Carsten, Hanna, Martin, Jakob, David, Simeon, Cristina, Thorben, and many others for all the laughs and open ears. Much appreciation further goes to Dr. Hendrik Heenen for the scientific and strategic advice especially during the last few months and Dr. Georg (Mitch) Michelitsch for his seemingly endless patience with my first steps in computational chemistry. Though never officially registered, I very much want to thank the "emotional support group" who always helped see the end of the road a little clearer. You know who you are.

Darüber hinaus möchte ich mich bei meinen wundervollen Freunden außerhalb des Lehrstuhls bedanken, die mich schon viele Jahre begleiten. Ob hier in München, Darmstadt oder über den Globus verstreut: Ihr macht das Leben bunter und es macht einfach mehr Spaß.

Ein ganz besonderer Dank gilt meinen Eltern, die mich immer unterstützt und meinen Weg nie in Frage gestellt haben. Ohne Euch beide wäre ich nicht hier. Gleiches gilt für meine Geschwister und Schwäger*innen; Ihr habt mir immer wieder aufgezeigt, dass das Leben doch nicht so ernst ist. Vielen Dank auch an meine Schwiegerfamilie für Euer ehrliches Interesse an meiner Arbeit und Eure bedingungslose Unterstützung.

Zu guter Letzt möchte ich mich von ganzem Herzen bei Dominic bedanken. Für alles.

München, Juli 2022 Sina Stegmaier

Bibliography

[1] S. Stegmaier, R. Schierholz, I. Povstugar, J. Barthel, S. P. Rittmeyer, S. Yu, S. Wengert, S. Rostami, H. Kungl, K. Reuter, R. A. Eichel, and C. Scheurer, Adv. Energy Mater. **11**, 2100707 (2021) (cit. on pp. i, 19, 34, 39, 41–44, 46, 47, 49–65, 67, 72, 75, 89–91, 93).

[2] S. Stegmaier, K. Reuter, and C. Scheurer, Nanomaterials **12**, 2912 (2022) (cit. on pp. i, 71, 73, 75, 77–80, 82–85, 87–92).

[3] K. J. Kim, M. Balaish, M. Wadaguchi, L. Kong, and J. L. Rupp, Adv. Energy Mater. **11**, 2002689 (2021) (cit. on p. 1).

[4] L. Xu, S. Tang, Y. Cheng, K. Wang, J. Liang, C. Liu, Y. C. Cao, F. Wei, and L. Mai, Joule **2**, 1991 (2018) (cit. on p. 1).

[5] K. Takada, Acta Mater. **61**, 759 (2013) (cit. on p. 1).

[6] J. Nanda, C. Wang, and P. Liu, MRS Bull. **43**, 752 (2018) (cit. on p. 1).

[7] X. B. Cheng, R. Zhang, C. Z. Zhao, and Q. Zhang, Chem. Rev. **117**, 10403 (2017) (cit. on pp. 1, 17).

[8] J. Liu, Z. Bao, Y. Cui, E. J. Dufek, J. B. Goodenough, P. Khalifah, Q. Li, B. Y. Liaw, P. Liu, A. Manthiram, Y. S. Meng, V. R. Subramanian, M. F. Toney, V. V. Viswanathan, M. S. Whittingham, J. Xiao, W. Xu, J. Yang, X. Q. Yang, and J. G. Zhang, Nat. Energy **4**, 180 (2019) (cit. on pp. 1, 17).

[9] X. Han, Y. Gong, K. Fu, X. He, G. T. Hitz, J. Dai, A. Pearse, B. Liu, H. Wang, G. Rubloff, Y. Mo, V. Thangadurai, E. D. Wachsman, and L. Hu, Nat. Mater. **16**, 572 (2017) (cit. on pp. 1, 72).

[10] H. Yuan, J. Nai, H. Tian, Z. Ju, W. Zhang, Y. Liu, X. Tao, and X. W. Lou, Sci. Adv. **6**, 1 (2020) (cit. on p. 2).

[11] B. Ederer, *BMW Group Strengthens Leadership Position in Battery Technology with Investment in Solid-State Innovator Solid Power*, May 2021 (cit. on p. 2).

[12] E. Beltz and J. Kulawik, *Volkswagen increases stake in QuantumScape | Volkswagen Newsroom*, 2020 (cit. on p. 2).

[13] C. Bauer, S. Burkhardt, N. P. Dasgupta, L. A. W. Ellingsen, L. L. Gaines, H. Hao, R. Hischier, L. Hu, Y. Huang, J. Janek, C. Liang, H. Li, J. Li, Y. Li, Y. C. Lu, W. Luo, L. F. Nazar, E. A. Olivetti, J. F. Peters, J. L. Rupp, M. Weil, J. F. Whitacre, and S. Xu, Nat. Sustain. **5**, 176 (2022) (cit. on p. 2).

[14] J. C. Bachman, S. Muy, A. Grimaud, H. H. Chang, N. Pour, S. F. Lux, O. Paschos, F. Maglia, S. Lupart, P. Lamp, L. Giordano, and Y. Shao-Horn, Chem. Rev. **116**, 140 (2016) (cit. on p. 2).
[15] L. Wang, J. Li, G. Lu, W. Li, Q. Tao, C. Shi, H. Jin, G. Chen, and S. Wang, Front. Mater. **7**, 111 (2020) (cit. on p. 2).
[16] J. Janek and W. G. Zeier, Nat. Energy **1**, 16141 (2016) (cit. on p. 2).
[17] A. C. Luntz, J. Voss, and K. Reuter, J. Phys. Chem. Lett. **6**, 4599 (2015) (cit. on p. 2).
[18] Y. Xiao, Y. Wang, S. H. Bo, J. C. Kim, L. J. Miara, and G. Ceder, Nat. Rev. Mater. **5**, 105 (2020) (cit. on p. 2).
[19] Z. Zhang, Y. Shao, B. Lotsch, Y. S. Hu, H. Li, J. Janek, L. F. Nazar, C. W. Nan, J. Maier, M. Armand, and L. Chen, Energy Environ. Sci. **11**, 1945 (2018) (cit. on p. 2).
[20] Y. Zhu, X. He, and Y. Mo, J. Mater. Chem. A **4**, 3253 (2016) (cit. on p. 2).
[21] C. Chen, M. Jiang, T. Zhou, L. Raijmakers, E. Vezhlev, B. Wu, T. U. Schülli, D. L. Danilov, Y. Wei, R.-A. Eichel, and P. H. L. Notten, Adv. Energy Mater., 2003939 (2021) (cit. on p. 2).
[22] E. Glynos, C. Pantazidis, and G. Sakellariou, ACS Omega **5**, 2531 (2020) (cit. on p. 2).
[23] V. A. Nguyen and C. Kuss, J. Electrochem. Soc. **167**, 065501 (2020) (cit. on p. 2).
[24] H. Chen, M. Ling, L. Hencz, H. Y. Ling, G. Li, Z. Lin, G. Liu, and S. Zhang, Chem. Rev. **118**, 8936 (2018) (cit. on p. 2).
[25] M. Liu, Z. Cheng, S. Ganapathy, C. Wang, L. A. Haverkate, M. Tułodziecki, S. Unnikrishnan, and M. Wagemaker, ACS Energy Lett. **4**, 2336 (2019) (cit. on p. 2).
[26] R. Koerver, W. Zhang, L. De Biasi, S. Schweidler, A. O. Kondrakov, S. Kolling, T. Brezesinski, P. Hartmann, W. G. Zeier, and J. Janek, Energy Environ. Sci. **11**, 2142 (2018) (cit. on pp. 2, 16).
[27] X. Miao, H. Wang, R. Sun, C. Wang, Z. Zhang, Z. Li, and L. Yin, Energy Environ. Sci. **13**, 3780 (2020) (cit. on pp. 2, 16, 17, 71).
[28] Z. Ding, J. Li, J. Li, and C. An, J. Electrochem. Soc. **167**, 070541 (2020) (cit. on pp. 2, 16, 71).
[29] D. Cao, X. Sun, Q. Li, A. Natan, P. Xiang, and H. Zhu, Matter **3**, 57 (2020) (cit. on pp. 2, 18, 39, 40, 71, 89).
[30] P. Albertus, S. Babinec, S. Litzelman, and A. Newman, Nat. Energy **3**, 16 (2018) (cit. on pp. 2, 39).
[31] Y.-W. Byeon and H. Kim, Electrochem **2**, 452 (2021) (cit. on pp. 2, 71).
[32] H. Liu, X. B. Cheng, J. Q. Huang, H. Yuan, Y. Lu, C. Yan, G. L. Zhu, R. Xu, C. Z. Zhao, L. P. Hou, C. He, S. Kaskel, and Q. Zhang, ACS Energy Lett. **5**, 833 (2020) (cit. on pp. 2, 16, 19, 71).
[33] S. Yu, A. Mertens, H. Tempel, R. Schierholz, H. Kungl, and R. A. Eichel, ACS Appl. Mater. Interfaces **10**, 22264 (2018) (cit. on pp. 2, 19, 40, 41, 71, 89).
[34] E. J. Cheng, A. Sharafi, and J. Sakamoto, Electrochim. Acta **223**, 85 (2017) (cit. on pp. 2, 19, 71).
[35] F. Aguesse, W. Manalastas, L. Buannic, J. M. L. Del Amo, G. Singh, A. Llordés, and J. Kilner, ACS Appl. Mater. Interfaces **9**, 3808 (2017) (cit. on pp. 2, 18, 40).

[36] H. K. Tian, B. Xu, and Y. Qi, J. Power Sources **392**, 79 (2018) (cit. on pp. 2, 18, 40).
[37] Y. Song, L. Yang, W. Zhao, Z. Wang, Y. Zhao, Z. Wang, Q. Zhao, H. Liu, and F. Pan, Adv. Energy Mater. **9**, 1900671 (2019) (cit. on pp. 2, 18, 40).
[38] Y. Dong, Z. Zhang, A. Alvarez, and I. W. Chen, Acta Mater. **199**, 264 (2020) (cit. on pp. 2, 18, 19, 40).
[39] T. Krauskopf, F. H. Richter, W. G. Zeier, and J. Janek, Chem. Rev. **120**, 7745 (2020) (cit. on pp. 2, 18, 19, 40).
[40] F. Han, A. S. Westover, J. Yue, X. Fan, F. Wang, M. Chi, D. N. Leonard, N. J. Dudney, H. Wang, and C. Wang, Nat. Energy **4**, 187 (2019) (cit. on pp. 2, 18, 40, 41, 68).
[41] Y. Zhu, X. He, and Y. Mo, ACS Appl. Mater. Interfaces **7**, 23685 (2015) (cit. on pp. 2, 3, 11, 39).
[42] A. Urban, D. H. Seo, and G. Ceder, npj Comput. Mater. **2**, 16002 (2016) (cit. on pp. 2, 3, 39).
[43] J. Luo, J. Mater. **1**, 22 (2015) (cit. on pp. 2, 19, 40, 68).
[44] J. Luo, Energy Storage Mater. **21**, 50 (2019) (cit. on pp. 2, 19, 40, 48, 60, 68).
[45] P. R. Cantwell, T. Frolov, T. J. Rupert, A. R. Krause, C. J. Marvel, G. S. Rohrer, J. M. Rickman, and M. P. Harmer, Annu. Rev. Mater. Res. **50**, 465 (2020) (cit. on pp. 2, 19, 40).
[46] S. J. Dillon and M. P. Harmer, J. Eur. Ceram. Soc. **28**, 1485 (2008) (cit. on pp. 2, 19, 40).
[47] A. Mertens, S. Yu, N. Schön, D. C. Gunduz, H. Tempel, R. Schierholz, F. Hausen, H. Kungl, J. Granwehr, and R. A. Eichel, Solid State Ionics **309**, 180 (2017) (cit. on pp. 2, 19, 42, 44, 47, 48, 63, 64, 68, 79, 84, 86, 91).
[48] M. B. Dixit, J. S. Park, P. Kenesei, J. Almer, and K. B. Hatzell, Energy Environ. Sci. **14**, 4672 (2021) (cit. on pp. 2, 19).
[49] G. Gourdin and V. Doan-Nguyen, Cell Reports Phys. Sci. **2**, 100660 (2021) (cit. on pp. 2, 19).
[50] A. M. Nolan, Y. Zhu, X. He, Q. Bai, and Y. Mo, Joule **2**, 2016 (2018) (cit. on p. 3).
[51] Q. Zhao, S. Stalin, C. Z. Zhao, and L. A. Archer, Nat. Rev. Mater. **5**, 229 (2020) (cit. on pp. 5, 7, 9, 10, 12, 17).
[52] F. Zheng, M. Kotobuki, S. Song, M. O. Lai, and L. Lu, J. Power Sources **389**, 198 (2018) (cit. on pp. 5, 8–10).
[53] D. Karabelli, K. P. Birke, and M. Weeber, Batteries **7**, 18 (2021) (cit. on pp. 5, 7, 9).
[54] N. Wu, P. H. Chien, Y. Qian, Y. Li, H. Xu, N. S. Grundish, B. Xu, H. Jin, Y. Y. Hu, G. Yu, and J. B. Goodenough, Angew. Chem. Int. Ed. **59**, 4131 (2020) (cit. on p. 5).
[55] S. Li, S. Q. Zhang, L. Shen, Q. Liu, J. B. Ma, W. Lv, Y. B. He, and Q. H. Yang, Adv. Sci. **7**, 1903088 (2020) (cit. on pp. 5, 9).
[56] M. B. Dixit, W. Zaman, N. Hortance, S. Vujic, B. Harkey, F. Shen, W. Y. Tsai, V. De Andrade, X. C. Chen, N. Balke, and K. B. Hatzell, Joule **4**, 207 (2020) (cit. on p. 5).
[57] D. Mazumdar, D. N. Bose, and M. L. Mukherjee, Solid State Ionics **14**, 143 (1984) (cit. on pp. 7, 11).
[58] Y.-W. Hu, I. D. Raistrick, and R. A. Huggins, J. Electrochem. Soc. **124**, 1240 (1977) (cit. on pp. 7, 11).

[59] J. Kuwano and A. R. West, Mater. Res. Bull. **15**, 1661 (1980) (cit. on pp. 7, 11).
[60] S. Song, J. Lu, F. Zheng, H. M. Duong, and L. Lu, RSC Adv. **5**, 6588 (2015) (cit. on pp. 7, 11).
[61] H. Aono, E. Sugimoto, Y. Sadaoka, N. Imanaka, and G.-y. Adachi, Solid State Ionics **40-41**, 38 (1990) (cit. on pp. 7, 11, 13, 14, 64).
[62] J. E. Iglesias and C. Pecharromán, Solid State Ionics **112**, 309 (1998) (cit. on p. 7).
[63] Tech Vision Group, *Innovations in Solid State Batteries: Need for Safer Alternatives Drives Innovations in Solid State Batteries* (Frost & Sullivan, Santa Clara, 2018) (cit. on p. 7).
[64] M. Illbeigi, A. Fazlali, M. Kazazi, and A. H. Mohammadi, Solid State Ionics **289**, 180 (2016) (cit. on pp. 7, 11).
[65] C. H. Chen and K. Amine, Solid State Ionics **144**, 51 (2001) (cit. on pp. 7, 11, 12).
[66] Y. Zheng, Y. Yao, J. Ou, M. Li, D. Luo, H. Dou, Z. Li, K. Amine, A. Yu, and Z. Chen, Chem. Soc. Rev. **49**, 8790 (2020) (cit. on pp. 7–9).
[67] Y. Zhao and L. L. Daemen, J. Am. Chem. Soc. **134**, 15042 (2012) (cit. on pp. 7, 11).
[68] J. Awaka, N. Kijima, H. Hayakawa, and J. Akimoto, J. Solid State Chem. **182**, 2046 (2009) (cit. on p. 7).
[69] V. Thangadurai, S. Narayanan, and D. Pinzaru, Chem. Soc. Rev. **43**, 4714 (2014) (cit. on p. 7).
[70] R. Murugan, V. Thangadurai, and W. Weppner, Phys. Inorg. Chem. **38**, 1 (2007) (cit. on pp. 7, 11).
[71] G. Larraz, A. Orera, and M. L. Sanjuán, J. Mater. Chem. A **1**, 11419 (2013) (cit. on p. 8).
[72] W. Xia, B. Xu, H. Duan, X. Tang, Y. Guo, H. Kang, H. Li, and H. Liu, J. Am. Ceram. Soc. **100**, 2832 (2017) (cit. on p. 8).
[73] N. Kamaya, K. Homma, Y. Yamakawa, M. Hirayama, R. Kanno, M. Yonemura, T. Kamiyama, Y. Kato, S. Hama, K. Kawamoto, and A. Mitsui, Nat. Mater. **10**, 682 (2011) (cit. on pp. 8, 11).
[74] Y. Mo, S. P. Ong, and G. Ceder, Chem. Mater. **24**, 15 (2012) (cit. on p. 8).
[75] A. Hayashi, S. Hama, H. Morimoto, M. Tatsumisago, and T. Minami, J. Am. Ceram. Soc. **84**, 477 (2001) (cit. on pp. 8, 11).
[76] P. R. Rayavarapu, N. Sharma, V. K. Peterson, and S. Adams, J. Solid State Electrochem. **16**, 1807 (2012) (cit. on p. 8).
[77] X. Li, J. Liang, X. Yang, K. R. Adair, C. Wang, F. Zhao, and X. Sun, Energy Environ. Sci. **13**, 1429 (2020) (cit. on p. 8).
[78] H. Zhang, C. Li, M. Piszcz, E. Coya, T. Rojo, L. M. Rodriguez-Martinez, M. Armand, and Z. Zhou, Chem. Soc. Rev. **46**, 797 (2017) (cit. on p. 9).
[79] D. Golodnitsky, E. Strauss, E. Peled, and S. Greenbaum, J. Electrochem. Soc. **162**, A2551 (2015) (cit. on p. 9).
[80] G. Homann, L. Stolz, J. Nair, I. C. Laskovic, M. Winter, and J. Kasnatscheew, Sci. Rep. **10**, 4390 (2020) (cit. on p. 9).

[81] R. Bouchet, S. Maria, R. Meziane, A. Aboulaich, L. Lienafa, J.-p. Bonnet, T. Phan, D. Bertin, D. Gigmes, D. Devaux, R. Denoyel, and M. Armand, Nat. Mater. **12**, 452 (2013) (cit. on p. 9).
[82] R. Khurana, J. L. Schaefer, L. A. Archer, and G. W. Coates, J. Am. Chem. Soc. **136**, 7395 (2014) (cit. on p. 9).
[83] M. Uitz, V. Epp, P. Bottke, and M. Wilkening, J. Electroceram **38**, 142 (2017) (cit. on p. 10).
[84] C. Wang, B. B. Xu, X. Zhang, W. Sun, J. Chen, H. Pan, M. Yan, and Y. Jiang, Small, 2107064 (2022) (cit. on p. 10).
[85] W. Jost, J. Chem. Phys. **1**, 466 (1933) (cit. on p. 10).
[86] B. Kozinsky, S. A. Akhade, P. Hirel, A. Hashibon, C. Elsässer, P. Mehta, A. Logeat, and U. Eisele, Phys. Rev. Lett. **116**, 055901 (2016) (cit. on p. 10).
[87] S. Stegmaier, J. Voss, K. Reuter, and A. C. Luntz, Chem. Mater. **29**, 4330 (2017) (cit. on p. 10).
[88] P. Gorai, H. Long, E. Jones, S. Santhanagopalan, and V. Stevanović, J. Mater. Chem. A **8**, 3851 (2020) (cit. on p. 10).
[89] H. Yang and N. Wu, Energy Sci. Eng. **10**, 1643 (2022) (cit. on p. 10).
[90] R. Kanno and M. Murayama, J. Electrochem. Soc. **148**, A742 (2001) (cit. on pp. 11, 12).
[91] F. Mizuno, A. Hayashi, K. Tadanaga, and M. Tatsumisago, Adv. Mater. **17**, 918 (2005) (cit. on p. 11).
[92] A. Hayashi, S. Hama, H. Morimoto, M. Tatsumisago, and T. Minami, Chem. Lett. **30**, 872 (2001) (cit. on p. 11).
[93] A. Hayashi, S. Hama, T. Minami, and M. Tatsumisago, Electrochem. Commun. **5**, 111 (2003) (cit. on p. 11).
[94] J. Fu, Solid State Ionics **96**, 195 (1997) (cit. on pp. 11, 15).
[95] V. Thangadurai, A. Shukla, and J. Gopalakrishnan, Chem. Mater. **11**, 835 (1999) (cit. on p. 11).
[96] S. Yu, A. Mertens, X. Gao, D. C. Gunduz, R. Schierholz, S. Benning, F. Hausen, J. Mertens, H. Kungl, H. Tempel, and R. A. Eichel, Funct. Mater. Lett. **9**, 1650066 (2016) (cit. on pp. 11, 15, 43, 52, 53, 64, 91, 92, 94).
[97] X. Lü, J. W. Howard, A. Chen, J. Zhu, S. Li, G. Wu, P. Dowden, H. Xu, Y. Zhao, and Q. Jia, Adv. Sci. **3**, 1500359 (2016) (cit. on p. 11).
[98] V. Thangadurai, D. Pinzaru, S. Narayanan, and A. K. Baral, J. Phys. Chem. Lett. **6**, 292 (2015) (cit. on p. 11).
[99] Y. Li, J. T. Han, C. A. Wang, H. Xie, and J. B. Goodenough, J. Mater. Chem. **22**, 15357 (2012) (cit. on p. 11).
[100] J. F. Wu, E. Y. Chen, Y. Yu, L. Liu, Y. Wu, W. K. Pang, V. K. Peterson, and X. Guo, ACS Appl. Mater. Interfaces **9**, 1542 (2017) (cit. on p. 11).
[101] O. Pecher, S. T. Kong, T. Goebel, V. Nickel, K. Weichert, C. Reiner, H. J. Deiseroth, J. Maier, F. Haarmann, and D. Zahn, Chem. Eur. J. **16**, 8347 (2010) (cit. on p. 11).
[102] R. P. Rao and S. Adams, Phys. Status Solidi A **208**, 1804 (2011) (cit. on p. 11).

[103] S. Boulineau, M. Courty, J. M. Tarascon, and V. Viallet, Solid State Ionics **221**, 1 (2012) (cit. on pp. 11, 12).
[104] F. Bai, K. Kakimoto, X. Shang, D. Mori, S. Taminato, M. Matsumoto, Y. Takeda, O. Yamamoto, H. Izumi, H. Minami, and N. Imanishi, Front. Energy Res. **8**, 187 (2020) (cit. on p. 10).
[105] C. F. Marchiori, R. P. Carvalho, M. Ebadi, D. Brandell, and C. M. Araujo, Chem. Mater. **32**, 7237 (2020) (cit. on p. 11).
[106] T. K. Schwietert, A. Vasileiadis, and M. Wagemaker, JACS Au **1**, 1488 (2021) (cit. on pp. 11, 12).
[107] B. Feng, T. Yokoi, A. Kumamoto, M. Yoshiya, Y. Ikuhara, and N. Shibata, Nat. Commun. **7**, 11079 (2016) (cit. on p. 12).
[108] Y. Benabed, M. Rioux, S. Rousselot, G. Hautier, and M. Dollé, Front. Energy Res. **9**, 682008 (2021) (cit. on p. 12).
[109] S. Yan, C. H. Yim, V. Pankov, M. Bauer, E. Baranova, A. Weck, A. Merati, and Y. Abu-Lebdeh, Batteries **7**, 75 (2021) (cit. on p. 12).
[110] W. Xiao, J. Wang, L. Fan, J. Zhang, and X. Li, Energy Storage Mater. **19**, 379 (2019) (cit. on pp. 12–14).
[111] R. Dewees and H. Wang, Chem. Sustain. Energy Mater. **12**, 3713 (2019) (cit. on pp. 12, 15, 16, 18).
[112] R. Höll, M. Kling, and E. Schroll, Ore Geol. Rev. **30**, 145 (2007) (cit. on p. 13).
[113] C. A. Hampel, *The Encyclopedia of the Chemical Elements* (Reinhold Book Corporation, New York, 1968) (cit. on p. 13).
[114] L. O. Hagman and P. Kierkegaard, Acta Chem. Scand. **22**, 1822 (1968) (cit. on p. 13).
[115] D. H. Kothari and D. K. Kanchan, Phys. B Condens. Matter **494**, 20 (2016) (cit. on p. 13).
[116] B. Zhang, R. Tan, L. Yang, J. Zheng, K. Zhang, S. Mo, Z. Lin, and F. Pan, Energy Storage Mater. **10**, 139 (2018) (cit. on p. 13).
[117] B. Key, D. J. Schroeder, B. J. Ingram, and J. T. Vaughey, Chem. Mater. **24**, 287 (2012) (cit. on p. 13).
[118] D. Pfalzgraf, D. Mutter, and D. F. Urban, Solid State Ionics **359**, 115521 (2021) (cit. on p. 13).
[119] K. Arbi, M. Hoelzel, A. Kuhn, F. García-Alvarado, and J. Sanz, Phys. Chem. Chem. Phys. **16**, 18397 (2014) (cit. on p. 13).
[120] M. Monchak, T. Hupfer, A. Senyshyn, H. Boysen, D. Chernyshov, T. Hansen, K. G. Schell, E. C. Bucharsky, M. J. Hoffmann, and H. Ehrenberg, Inorg. Chem. **55**, 2941 (2016) (cit. on pp. 13, 14, 86).
[121] H. Aono, E. Sugimoto, Y. Sadaoka, N. Imanaka, and G.-y. Adachi, J. Electrochem. Soc. **136**, 590 (1989) (cit. on p. 13).
[122] H. Aono, E. Sugimoto, Y. Sadaoka, N. Imanaka, and G.-y. Adachi, J. Electrochem. Soc. **137**, 1023 (1990) (cit. on pp. 13, 14, 64, 77).
[123] C. M. Chang, Y. Lee, S. H. Hong, and H. M. Park, J. Am. Ceram. Soc. **88**, 1803 (2005) (cit. on pp. 13, 15).

[124] K. Arbi, W. Bucheli, R. Jiménez, and J. Sanz, J. Eur. Ceram. Soc. **35**, 1477 (2015) (cit. on p. 13).
[125] Y. K. Shin, M. Y. Sengul, A. S. Jonayat, W. Lee, E. D. Gomez, C. A. Randall, and A. C. Van Duin, Phys. Chem. Chem. Phys. **20**, 22134 (2018) (cit. on pp. 13, 14).
[126] D. Qui, S. Hamdoune, J. L. Soubeyroux, and E. Prince, J. Solid State Chem. **72**, 309 (1988) (cit. on p. 13).
[127] D. Rettenwander, A. Welzl, S. Pristat, F. Tietz, S. Taibl, G. J. Redhammer, and J. Fleig, J. Mater. Chem. A **4**, 1506 (2016) (cit. on pp. 14, 15).
[128] K. Waetzig, A. Rost, C. Heubner, M. Coeler, K. Nikolowski, M. Wolter, and J. Schilm, J. Alloys Compd. **818**, 153237 (2020) (cit. on p. 15).
[129] Y. Yoon, J. Kim, C. Park, and D. Shin, J. Ceram. Process. Res. **14**, 563 (2013) (cit. on pp. 15, 43).
[130] M. Kotobuki and M. Koishi, Ceram. Int. **39**, 4645 (2013) (cit. on p. 15).
[131] Q. Ma, Q. Xu, C. L. Tsai, F. Tietz, and O. Guillon, J. Am. Ceram. Soc. **99**, 410 (2016) (cit. on p. 15).
[132] T. Hupfer, *Herstellung von LATP für den Einsatz als Festkörperelektrolyt und dessen Eigenschaften* (KIT Scientific Publishing, Karlsruhe, 2017) (cit. on pp. 15, 43, 46, 47, 53, 59, 64).
[133] L. Hallopeau, D. Bregiroux, G. Rousse, D. Portehault, P. Stevens, G. Taussant, and C. Laberty-Robert, J. Power Sources **378**, 48 (2018) (cit. on p. 15).
[134] C. Davis and J. C. Nino, J. Am. Ceram. Soc. **98**, 2422 (2015) (cit. on p. 15).
[135] S. Duluard, A. Paillassa, P. Lenormand, P. L. Taberna, P. Simon, P. Rozier, F. Ansart, and J. Ihlefeld, J. Am. Ceram. Soc. **100**, 141 (2017) (cit. on p. 15).
[136] H. Morimoto, H. Awano, J. Terashima, Y. Shindo, S. Nakanishi, N. Ito, K. Ishikawa, and S. I. Tobishima, J. Power Sources **240**, 636 (2013) (cit. on p. 15).
[137] K. M. Kim, D. O. Shin, and Y. G. Lee, Electrochim. Acta **176**, 1364 (2015) (cit. on p. 15).
[138] L. Huang, Z. Wen, M. Wu, X. Wu, Y. Liu, and X. Wang, J. Power Sources **196**, 6943 (2011) (cit. on p. 15).
[139] M. Weiss, D. A. Weber, A. Senyshyn, J. Janek, and W. G. Zeier, ACS Appl. Mater. Interfaces **10**, 10935 (2018) (cit. on p. 14).
[140] G. J. Redhammer, D. Rettenwander, S. Pristat, E. Dashjav, C. M. Kumar, D. Topa, and F. Tietz, Solid State Sci. **60**, 99 (2016) (cit. on pp. 14, 64).
[141] H. Morimoto, M. Hirukawa, A. Matsumoto, T. Kurahayashi, N. Ito, and S. I. Tobishima, Electrochemistry **82**, 870 (2014) (cit. on p. 14).
[142] J. Xie, N. Imanishi, T. Zhang, A. Hirano, Y. Takeda, and O. Yamamoto, J. Power Sources **189**, 365 (2009) (cit. on p. 15).
[143] H. S. Kim, Y. Oh, K. H. Kang, J. H. Kim, J. Kim, and C. S. Yoon, ACS Appl. Mater. Interfaces **9**, 16063 (2017) (cit. on p. 15).
[144] J. Liu, T. Liu, Y. Pu, M. Guan, Z. Tang, F. Ding, Z. Xu, and Y. Li, RSC Adv. **7**, 46545 (2017) (cit. on p. 15).

[145] Y. Liu, Q. Sun, Y. Zhao, B. Wang, P. Kaghazchi, K. R. Adair, R. Li, C. Zhang, J. Liu, L. Y. Kuo, Y. Hu, T. K. Sham, L. Zhang, R. Yang, S. Lu, X. Song, and X. Sun, ACS Appl. Mater. Interfaces **10**, 31240 (2018) (cit. on p. 15).
[146] S. Yu, S. Schmohl, Z. Liu, M. Hoffmeyer, N. Schön, F. Hausen, H. Tempel, H. Kungl, H. D. Wiemhöfer, and R. A. Eichel, J. Mater. Chem. A **7**, 3882 (2019) (cit. on pp. 16, 40, 41, 68).
[147] L. Li, Z. Zhang, L. Luo, J. Jiao, W. Huang, J. Wang, C. Li, X. Han, and S. Chen, Ionics **26**, 3815 (2020) (cit. on p. 16).
[148] S. Wang, J. Wang, J. Liu, H. Song, Y. Liu, P. Wang, P. He, J. Xu, and H. Zhou, J. Mater. Chem. A **6**, 21248 (2018) (cit. on pp. 16, 71).
[149] J. A. Lewis, F. J. Q. Cortes, Y. Liu, J. C. Miers, A. Verma, B. S. Vishnugopi, J. Tippens, D. Prakash, T. S. Marchese, S. Y. Han, C. Lee, P. P. Shetty, H. W. Lee, P. Shevchenko, F. De Carlo, C. Saldana, P. P. Mukherjee, and M. T. McDowell, Nat. Mater. **20**, 503 (2021) (cit. on p. 16).
[150] C. Monroe and J. Newman, J. Electrochem. Soc. **152**, A396 (2005) (cit. on p. 16).
[151] L. Porz, T. Swamy, B. W. Sheldon, D. Rettenwander, T. Frömling, H. L. Thaman, S. Berendts, R. Uecker, W. C. Carter, and Y. M. Chiang, Adv. Energy Mater. **7**, 1701003 (2017) (cit. on pp. 16, 18).
[152] X. Ke, Y. Wang, G. Ren, and C. Yuan, Energy Storage Mater. **26**, 313 (2020) (cit. on p. 16).
[153] S. Wenzel, T. Leichtweiss, D. Krüger, J. Sann, and J. Janek, Solid State Ionics **278**, 98 (2015) (cit. on p. 17).
[154] P. Hartmann, T. Leichtweiss, M. R. Busche, M. Schneider, M. Reich, J. Sann, P. Adelhelm, and J. Janek, J. Phys. Chem. C **117**, 21064 (2013) (cit. on p. 17).
[155] K. H. Kim, Y. Iriyama, K. Yamamoto, S. Kumazaki, T. Asaka, K. Tanabe, C. A. Fisher, T. Hirayama, R. Murugan, and Z. Ogumi, J. Power Sources **196**, 764 (2011) (cit. on p. 17).
[156] J. Haruyama, K. Sodeyama, L. Han, K. Takada, and Y. Tateyama, Chem. Mater. **26**, 4248 (2014) (cit. on p. 17).
[157] K. Yamamoto, Y. Iriyama, T. Asaka, T. Hirayama, H. Fujita, C. A. Fisher, K. Nonaka, Y. Sugita, and Z. Ogumi, Angew. Chem. Int. Ed. **49**, 4414 (2010) (cit. on p. 17).
[158] J. Zhang, C. Zheng, L. Li, Y. Xia, H. Huang, Y. Gan, C. Liang, X. He, X. Tao, and W. Zhang, Adv. Energy Mater. **10**, 1903311 (2020) (cit. on p. 17).
[159] J. B. Goodenough and Y. Kim, Chem. Mater. **22**, 587 (2010) (cit. on p. 18).
[160] C. L. Tsai, V. Roddatis, C. V. Chandran, Q. Ma, S. Uhlenbruck, M. Bram, P. Heitjans, and O. Guillon, ACS Appl. Mater. Interfaces **8**, 10617 (2016) (cit. on p. 18).
[161] F. Shen, M. B. Dixit, X. Xiao, and K. B. Hatzell, ACS Energy Lett. **3**, 1056 (2018) (cit. on p. 18).
[162] W. E. Tenhaeff, E. Rangasamy, Y. Wang, A. P. Sokolov, J. Wolfenstine, J. Sakamoto, and N. J. Dudney, ChemElectroChem **1**, 375 (2014) (cit. on p. 19).
[163] T. W. Heo, A. Grieder, B. Wang, M. Wood, T. Hsu, S. A. Akhade, L. F. Wan, L. Q. Chen, N. Adelstein, and B. C. Wood, npj Comput. Mater. **7**, 214 (2021) (cit. on p. 19).

[164] N. Schön, D. C. Gunduz, S. Yu, H. Tempel, R. Schierholz, and F. Hausen, Beilstein J. Nanotechnol. **9**, 1564 (2018) (cit. on p. 19).
[165] D. C. Gündüz, R. Schierholz, S. Yu, H. Tempel, H. Kungl, and R. A. Eichel, J. Adv. Ceram. **9**, 149 (2020) (cit. on pp. 19, 43, 64, 91).
[166] J. A. Dawson, P. Canepa, T. Famprikis, C. Masquelier, and M. S. Islam, J. Am. Chem. Soc. **140**, 362 (2018) (cit. on pp. 19, 20).
[167] C. Wang, Z. Sun, Y. Zhao, B. Wang, C. Shao, C. Sun, Y. Zhao, J. Li, H. Jin, and L. Qu, Small **17**, 2103819 (2021) (cit. on p. 19).
[168] C. Zheng, Y. Ruan, J. Su, Z. Song, T. Xiu, J. Jin, M. E. Badding, and Z. Wen, Chem. Eng. J. **411**, 128508 (2021) (cit. on p. 19).
[169] S. Yu and D. J. Siegel, ACS Appl. Mater. Interfaces **10**, 38151 (2018) (cit. on pp. 19, 20, 40, 68).
[170] J. S. Kim, W. D. Jung, J. W. Son, J. H. Lee, B. K. Kim, K. Y. Chung, H. G. Jung, and H. Kim, ACS Appl. Mater. Interfaces **11**, 13 (2019) (cit. on pp. 19, 20).
[171] L. Priester, "Atomic Order of Grain Boundaries," in *Grain boundaries* (Springer, Dordrecht, 2013), pp. 49–92 (cit. on p. 20).
[172] A. K. Ivanov-Schitz and G. N. Mazo, Crystallogr. Reports **63**, 1 (2018) (cit. on p. 20).
[173] H. Türk, F. P. Schmidt, T. Götsch, F. Girgsdies, A. Hammud, D. Ivanov, I. C. Vinke, L. G. de Haart, R. A. Eichel, K. Reuter, R. Schlögl, A. Knop-Gericke, C. Scheurer, and T. Lunkenbein, Adv. Mater. Interfaces **8**, 2100967 (2021) (cit. on pp. 20, 81, 93).
[174] M. Ceriotti, C. Clementi, and O. Anatole von Lilienfeld, J. Chem. Phys. **154**, 160401 (2021) (cit. on pp. 21, 24).
[175] V. L. Deringer, A. P. Bartók, N. Bernstein, D. M. Wilkins, M. Ceriotti, and G. Csányi, Chem. Rev. **121**, 10073 (2021) (cit. on pp. 21, 24).
[176] F. Jensen, *Introduction to Computational Chemistry*, 2nd ed. (John Wiley & Sons, Odense, 2007) (cit. on pp. 21, 23, 24).
[177] P. Hohenberg and W. Kohn, Phys. Rev. **136**, B864 (1964) (cit. on pp. 21, 22).
[178] R. Stowasser and R. Hoffmann, J. Am. Chem. Soc. **121**, 3414 (1999) (cit. on p. 22).
[179] D. P. Chong, O. V. Gritsenko, and E. J. Baerends, J. Chem. Phys. **116**, 1760 (2002) (cit. on p. 22).
[180] R. van Meer, O. V. Gritsenko, and E. J. Baerends, J. Chem. Theory Comput. **10**, 4432 (2014) (cit. on p. 22).
[181] A. D. Becke, J. Chem. Phys. **140**, 18A301 (2014) (cit. on p. 23).
[182] J. P. Perdew, J. A. Chevary, S. H. Vosko, K. A. Jackson, M. R. Pederson, D. J. Singh, and C. Fiolhais, Phys. Rev. B **46**, 6671 (1992) (cit. on p. 23).
[183] J. L. Da Silva, C. Stampfl, and M. Scheffler, Surf. Sci. **600**, 703 (2006) (cit. on p. 23).
[184] P. J. Hasnip, K. Refson, M. I. Probert, J. R. Yates, S. J. Clark, and C. J. Pickard, Philos. Trans. R. Soc. A **372**, 20130270 (2014) (cit. on p. 23).
[185] J. P. Perdew, K. Burke, and M. Ernzerhof, Phys. Rev. Lett. **77**, 3865 (1996) (cit. on pp. 23, 45, 66, 76).
[186] N. Mardirossian and M. Head-Gordon, Mol. Phys. **115**, 2315 (2017) (cit. on p. 23).

[187] P. Gao, X. Duan, T. Zhang, M. Zhang, B. Schmidt, X. Zhang, H. Sun, W. Zhang, L. Gan, W. Xue, H. Fu, W. Liu, and G. Yang, IEEE Trans. Parallel Distrib. Syst. **31**, 2954 (2020) (cit. on p. 24).
[188] D. van der Spoel, Curr. Opin. Struct. Biol. **67**, 18 (2021) (cit. on p. 24).
[189] J. Hill, C. Freeman, and L. Subramanain, "Use of Force Fields in Materials Modeling," in *Rev. comput. chem.* (Wiley-VCH, New York City, 2000), pp. 141–216 (cit. on pp. 24, 25).
[190] A. C. T. van Duin, S. Dasgupta, F. Lorant, and W. A. Goddard, J. Phys. Chem. A **105**, 9396 (2001) (cit. on p. 24).
[191] M. Born and K. Huang, Am. J. Phys. **23**, 474 (1955) (cit. on pp. 24, 25).
[192] A. Y. Toukmaji and J. A. Board, Comput. Phys. Commun. **95**, 73 (1996) (cit. on p. 24).
[193] R. W. Hockney and J. W. Eastwood, *Computer Simulation Using Particles*, 1st ed. (Taylor & Francis, New York City, 1988) (cit. on pp. 24, 45, 74).
[194] M. S. Islam and C. A. Fisher, Chem. Soc. Rev. **43**, 185 (2014) (cit. on p. 25).
[195] C. R. A. Catlow, *Computer Modelling in Inorganic Crystallography*, 1st ed. (Academic Press, San Diego, 1997) (cit. on p. 25).
[196] A. Sokol and C. R. A. Catlow, *Computational Approaches to Energy Materials* (John Wiley & Sons, Chichester, 2013) (cit. on p. 25).
[197] B. Szigeti, Proc. R. Soc. A **204**, 51 (1950) (cit. on p. 25).
[198] P. J. Mitchell and D. Fincham, J. Phys. Condens. Matter **5**, 1031 (1993) (cit. on pp. 25, 30, 31).
[199] B. G. Dick and A. W. Overhauser, Phys. Rev. **112**, 90 (1958) (cit. on pp. 25, 26).
[200] R. M. Sternheimer, Phys. Rev. **96**, 951 (1954) (cit. on p. 25).
[201] R. M. Sternheimer, Phys. Rev. **107**, 1565 (1957) (cit. on p. 25).
[202] P. Brommer, A. Kiselev, D. Schopf, P. Beck, J. Roth, and H. R. Trebin, Model. Simul. Mater. Sci. Eng. **23**, 074002 (2015) (cit. on p. 27).
[203] P. Tangney and S. Scandolo, J. Chem. Phys. **117**, 8898 (2002) (cit. on p. 27).
[204] A. K. Hartmann and H. Rieger, *Optimization Algorithms in Physics*, 1st ed. (Wiley-VCH, Berlin, 2001) (cit. on p. 28).
[205] J. D. Gale and A. L. Rohl, Mol. Simul. **29**, 291 (2003) (cit. on pp. 28, 45).
[206] A. Tonda, Genet. Program. Evolvable Mach. **21**, 269 (2020) (cit. on pp. 28, 76).
[207] C. Zhu, R. H. Byrd, P. Lu, and J. Nocedal, ACM Trans. Math. Softw. **23**, 550 (1997) (cit. on pp. 29, 74).
[208] D. Frenkel and B. Smit, *Understanding molecular simulations*, 2nd ed. (Academic Press, Cambridge, 2002) (cit. on pp. 29, 30).
[209] S. Plimpton, J. Comput. Phys. **117**, 1 (1995) (cit. on pp. 29, 45, 74).
[210] H. H. Heenen, C. Scheurer, and K. Reuter, Nano Lett. **17**, 3884 (2017) (cit. on p. 30).
[211] M. Allen and D. Tildesley, *Computer simulations of Liquids*, 2nd ed. (Oxford University Press, Oxford, 2017) (cit. on p. 31).
[212] D. Fincham, W. C. MacKrodt, and P. J. Mitchell, J. Phys. Condens. Matter **6**, 393 (1994) (cit. on p. 31).
[213] H. Mehrer, *Diffusion in Solids*, 1st ed. (Springer, Berlin, 2007) (cit. on pp. 31, 32, 34).
[214] H. Flyvbjerg and H. G. Petersen, J. Chem. Phys. **91**, 461 (1989) (cit. on p. 32).

[215] X. He, Y. Zhu, A. Epstein, and Y. Mo, npj Comput. Mater. **4**, 18 (2018) (cit. on pp. 32, 33).
[216] J. Kärger, D. M. Ruthven, and D. N. Throdorou, *Diffusion in nanoporous materials*, 1st ed. (Wiley-VCH, Weinheim, 2012) (cit. on p. 32).
[217] L. Reimer and H. Kohl, *Transmission Electron Microscopy*, 5th ed. (Springer, New York City, 2008) (cit. on pp. 34, 36).
[218] J. Barthel, Ultramicroscopy **193**, 1 (2018) (cit. on pp. 34, 35, 56).
[219] D. B. Williams and C. B. Carter, *Transmission Electron Microscopy*, 2nd ed. (Springer, New York City, 2009) (cit. on p. 35).
[220] J. M. Cowley and A. F. Moodie, Acta Crystallogr. **10**, 609 (1957) (cit. on p. 36).
[221] K. Ishizuka and N. Uyeda, Acta Crystallogr. **A33**, 740 (1977) (cit. on p. 37).
[222] R. F. Loane, P. Xu, and J. Silcox, Acta Crystallogr. **A47**, 267 (1991) (cit. on p. 38).
[223] W. D. Richards, L. J. Miara, Y. Wang, J. C. Kim, and G. Ceder, Chem. Mater. **28**, 266 (2016) (cit. on pp. 39, 72).
[224] X. Shan, Y. Zhong, L. Zhang, Y. Zhang, X. Xia, X. Wang, and J. Tu, J. Phys. Chem. C **125**, 19060 (2021) (cit. on p. 39).
[225] S. Kasap and P. Capper, eds., *Springer Handbook of Electronic and Photonic Materials*, 2nd ed. (Springer, Cham, 2017) (cit. on p. 40).
[226] J. Maier, Mater. Sustain. Energy **4**, 160 (2010) (cit. on p. 40).
[227] J. Maier, Chem. Mater. **26**, 348 (2014) (cit. on p. 40).
[228] A. S. Best, M. Forsyth, and D. R. MacFarlane, Solid State Ionics **136-137**, 339 (2000) (cit. on p. 43).
[229] J. Maier, B. Pfeiffer, C. A. Volkert, and C. Nowak, Energy Technol. **4**, 1565 (2016) (cit. on p. 44).
[230] A. Devaraj, M. Gu, R. Colby, P. Yan, C. M. Wang, J. M. Zheng, J. Xiao, A. Genc, J. G. Zhang, I. Belharouak, D. Wang, K. Amine, and S. Thevuthasan, Nat. Commun. **6**, 8014 (2015) (cit. on p. 44).
[231] A. Devaraj, R. Colby, W. P. Hess, D. E. Perea, and S. Thevuthasan, J. Phys. Chem. Lett. **4**, 993 (2013) (cit. on p. 44).
[232] W. Shinoda, M. Shiga, and M. Mikami, Phys. Rev. B **69**, 134103 (2004) (cit. on p. 45).
[233] M. Vijayakumar, S. Kerisit, K. M. Rosso, S. D. Burton, J. A. Sears, Z. Yang, G. L. Graff, J. Liu, and J. Hu, J. Power Sources **196**, 2211 (2011) (cit. on p. 45).
[234] S. Kerisit, N. Aaron Deskins, K. M. Rosso, and M. Dupais, J. Phys. Chem. C **112**, 7678 (2008) (cit. on pp. 45, 74).
[235] V. Blum, R. Gehrke, F. Hanke, P. Havu, V. Havu, X. Ren, K. Reuter, and M. Scheffler, Comput. Phys. Commun. **180**, 2175 (2009) (cit. on p. 45).
[236] H. J. Monkhorst and J. D. Pack, Phys. Rev. B **13**, 5188 (1976) (cit. on pp. 45, 76).
[237] M. Luysbger, M. Heggen, and K. Tillmann, J. large-scale Res. Facil. **2**, A77 (2016) (cit. on p. 56).
[238] A. Thust, Phys. Rev. Lett. **102**, 220801 (2009) (cit. on p. 56).
[239] S. Bals, W. Tirry, R. Geurts, Y. Zhiqing, and D. Schryvers, Microsc. Microanal. **13**, 80 (2007) (cit. on p. 59).

[240] F. Pérez-Willard, D. Wolde-Giorgis, T. Al-Kassab, G. A. López, E. J. Mittemeijer, R. Kirchheim, and D. Gerthsen, Micron **39**, 45 (2008) (cit. on p. 59).
[241] M. Kick, C. Scheurer, and H. Oberhofer, J. Chem. Phys. **153**, 144701 (2020) (cit. on pp. 62, 67, 89).
[242] M. Kick, C. Grosu, M. Schuderer, C. Scheurer, and H. Oberhofer, J. Phys. Chem. Lett. **11**, 2535 (2020) (cit. on pp. 62, 79, 89).
[243] H. Oberhofer, K. Reuter, and J. Blumberger, Chem. Rev. **117**, 10319 (2017) (cit. on pp. 62, 89).
[244] M. Monchak, O. Dolotko, M. J. Mühlbauer, V. Baran, A. Senyshyn, and H. Ehrenberg, Solid State Sci. **61**, 161 (2016) (cit. on pp. 64, 68).
[245] J. H. Jeon, E. Barkai, and R. Metzler, J. Chem. Phys. **139**, 121916 (2013) (cit. on p. 65).
[246] J. Meyer, "Ab initio Modeling of Energy Dissipation during Chemical Reactions at Transition Metal Surfaces," PhD thesis (Freie Universität Berlin, 2011) (cit. on p. 66).
[247] S. J. Clark, M. D. Segall, C. J. Pickard, P. J. Hasnip, M. I. Probert, K. Refson, and M. C. Payne, Z. Kristallogr. **220**, 567 (2005) (cit. on pp. 66, 76).
[248] K. F. Garrity, J. W. Bennett, K. M. Rabe, and D. Vanderbilt, Comput. Mater. Sci. **81**, 446 (2014) (cit. on pp. 66, 76).
[249] B. Wu, S. Wang, J. Lochala, D. Desrochers, B. Liu, W. Zhang, J. Yang, and J. Xiao, Energy Environ. Sci. **11**, 1803 (2018) (cit. on pp. 67, 89).
[250] A. J. Cohen, P. Mori-Sánchez, and W. Yang, Science **321**, 792 (2008) (cit. on p. 67).
[251] M. Du, K. Liao, Q. Lu, and Z. Shao, Energy Environ. Sci. **12**, 1780 (2019) (cit. on p. 71).
[252] B. Xu, W. Li, H. Duan, H. Wang, Y. Guo, H. Li, and H. Liu, J. Power Sources **354**, 68 (2017) (cit. on p. 72).
[253] L. E. Camacho-Forero and P. B. Balbuena, Chem. Mater. **32**, 360 (2020) (cit. on p. 72).
[254] P. Hartman and H. K. Chan, Pharm. Res. **10**, 1052 (1993) (cit. on p. 72).
[255] E. A. Cheung, H. Nguyen, M. Avdeev, N. R. De Souza, Y. S. Meng, and N. Sharma, Chem. Mater. **33**, 8768 (2021) (cit. on p. 73).
[256] S. H. Choi, S. J. Lee, D. J. Yoo, J. H. Park, J. H. Park, Y. N. Ko, J. Park, Y. E. Sung, S. Y. Chung, H. Kim, and J. W. Choi, Adv. Energy Mater. **9**, 1902278 (2019) (cit. on p. 73).
[257] P. Gao, H. Wu, X. Zhang, H. Jia, J. M. Kim, M. H. Engelhard, C. Niu, Z. Xu, J. G. Zhang, and W. Xu, Angew. Chem. Int. Ed. **60**, 16506 (2021) (cit. on p. 73).
[258] R. D. Shannon, Acta Crystallogr. **A32**, 751 (1976) (cit. on pp. 73, 74, 86).
[259] A. Squires, J. M. Dean, and B. J. Morgan, ChemRxiv, 10.26434/chemrxiv-2021-hzrls (2021) (cit. on p. 73).
[260] A. Jain, S. P. Ong, G. Hautier, W. Chen, W. D. Richards, S. Dacek, S. Cholia, D. Gunter, D. Skinner, G. Ceder, and K. A. Persson, APL Mater. **1**, 011002 (2013) (cit. on pp. 74, 75).
[261] F. H. Allen, Acta Crystallogr. **A54**, 758 (1998) (cit. on pp. 75, 78).

[262] Y. Nikodimos, L. H. Abrha, H. H. Weldeyohannes, K. N. Shitaw, N. T. Temesgen, B. W. Olbasa, C. J. Huang, S. K. Jiang, C. H. Wang, H. S. Sheu, S. H. Wu, W. N. Su, C. C. Yang, and B. J. Hwang, J. Mater. Chem. A **8**, 26055 (2020) (cit. on pp. 76–78, 86).
[263] M. Zhang, Z. Huang, J. Cheng, O. Yamamoto, N. Imanishi, B. Chi, J. Pu, and J. Li, J. Alloys Compd. **590**, 147 (2014) (cit. on p. 77).
[264] J. Yu, M. L. Sushko, S. Kerisit, K. M. Rosso, and J. Liu, J. Phys. Chem. Lett. **3**, 2076 (2012) (cit. on p. 79).
[265] N. Grillon, É. Bouyssou, S. Jacques, and G. Gautier, Microelectron. Reliab. **93**, 102 (2019) (cit. on p. 81).
[266] X. Fang, Y. He, X. Fan, D. Zhang, and H. Hu, Polymers **13**, 1206 (2021) (cit. on p. 81).
[267] J. Guo, Y. Li, K. Pedersen, and D.-i. Stroe, Energies **14**, 5220 (2021) (cit. on p. 81).
[268] C. J. Geyer and E. A. Thompson, J. Am. Stat. Assoc. **90**, 909 (1995) (cit. on p. 81).
[269] D. J. Earl and M. W. Deem, Phys. Chem. Chem. Phys. **7**, 3910 (2005) (cit. on p. 81).
[270] K. Waetzig, C. Heubner, and M. Kusnezoff, Crystals **10**, 408 (2020) (cit. on p. 84).
[271] A. Castillo, S. Yagoubi, O. Rapaud, N. Pradeilles, T. Charpentier, E. Foy, and H. Khodja, in 1st int. symp. solid state batter. (2018) (cit. on p. 86).
[272] J. Li, C. Liu, C. Miao, Z. Kou, and W. Xiao, Ionics **28**, 63 (2022) (cit. on p. 86).
[273] V. Epp, Q. Ma, E. M. Hammer, F. Tietz, and M. Wilkening, Phys. Chem. Chem. Phys. **17**, 32115 (2015) (cit. on p. 86).
[274] B. E. Francisco, C. R. Stoldt, and J. C. M'Peko, Chem. Mater. **26**, 4741 (2014) (cit. on p. 86).
[275] B. Lang, B. Ziebarth, and C. Elsässer, Chem. Mater. **27**, 5040 (2015) (cit. on p. 86).
[276] Q. Lv, Y. Jiang, B. Wang, Y. Chen, F. Jin, B. Wu, H. Ren, N. Zhang, R. Xu, Y. Li, T. Zhang, Y. Zhou, D. Wang, H. Liu, and S. Dou, Cell Reports Phys. Sci. **3**, 100706 (2022) (cit. on p. 89).
[277] A. M. Welsch, H. Behrens, D. Murawski, and I. Horn, Z. Phys. Chem. **231**, 1303 (2017) (cit. on p. 92).
[278] B. Kim, S. Lee, and J. Kim, Sci. Adv. **6**, 1 (2020) (cit. on p. 96).
[279] D. Wang, J. Yang, J. Liu, X. Li, R. Li, M. Cai, T. K. Sham, and X. Sun, J. Mater. Chem. A **2**, 2306 (2014) (cit. on p. 96).
[280] X. Li, J. Liu, M. N. Banis, A. Lushington, R. Li, M. Cai, and X. Sun, Energy Environ. Sci. **7**, 768 (2014) (cit. on p. 96).
[281] L. Han, C. T. Hsieh, B. Chandra Mallick, J. Li, and Y. Ashraf Gandomi, Nanoscale Adv. **3**, 2728 (2021) (cit. on p. 96).
[282] S. P. Jiang, Mater. Sci. Eng. A **418**, 199 (2006) (cit. on p. 96).

Appendix

A Force Field Parameters

A.1 Core-shell Force Field for $Li_{1+x}Al_xTi_{2-x}(PO_4)_3$

Table A.1: Optimum parameter set obtained for the core-shell $Li_{1.3}Al_{0.3}Ti_{1.7}(PO_4)_3$ force field, cf. Section 4.3.1. Table adapted from Stegmaier et al. [1] under CC BY 4.0.

Atom types			
species	**mass (u)**	**charge (e)**	
Ti [A.1]	47.867	+2.196	
Al	26.982	+1.647	
Li [A.2]	6.940	+0.549	
P	30.974	+2.745	
O_{core} [A.1]	15.698	+0.500	
O_{shell} [A.1]	0.301	-1.598	
Buckingham Parameters			
species ij	**A_{ij} (eV)**	**ρ_{ij} (Å)**	**C_{ij} (eVÅ^6)**
Li-Li [A.2]	38533.955	0.100	0.000
Ti-Li [A.2]	33089.570	0.127	0.000
Ti-Ti [A.1]	31120.528	0.154	5.250
Li-O [A.2]	15465.549	0.167	0.000
O-O [A.1]	11782.885	0.234	30.220
Ti-O	18448.156	0.194	12.590
P-P	53210.800	0.284	0.000
P-O	32397.875	0.155	7.831
P-Li	30393.156	0.131	0.000
P-Ti	10469.346	0.139	136.835
Al-Al	42700.844	0.197	0.000
Al-Li	32315.936	0.127	0.000
Al-Ti	10489.082	0.131	6.862
Al-O	17491.787	0.179	7.920
Al-P	10580.062	0.137	114.906
Core-Shell Force Constants[A.3]			
species ij		**k_{ij} (eVÅ^{-2})**	
O_{core}-O_{shell}		88.6	

[A.1] Parameters adopted from TiO force field [2].
[A.2] Parameters adopted from LTO force field [3].
[A.3] Interaction potential form: $V_{ij} = 1/2\, k_{ij} r_{ij}$

A.2 Force Field Extension by Mg^{2+}

Table A.2: Optimum parameter set obtained for the core-shell $Li_{1+x+2y}Al_xMg_yTi_{2-x-y}(PO_4)_3$ force field, cf. Section 5.3.1.

Atom types			
species	**mass (u)**	**charge (e)**	
Mg	24.305	+1.098	
Buckingham Parameters			
species ij	$\mathbf{A}_{ij}$ **(eV)**	ρ_{ij} **(Å)**	$\mathbf{C}_{ij}$ **(eVÅ^6)**
Mg-Mg	20671.120	0.148	0.000
Mg-Li	24050.700	0.138	0.000
Mg-Ti	12947.270	0.117	6.200
Mg-O	55835.770	0.179	12.620
Mg-P	56162.410	0.130	120.000
Mg-Al	21485.920	0.230	0.580

Table A.3: Buckingham $\rho_{\text{Mg-ion}}$ parameters from local optimization of the $Mg_3(PO_4)_2$ volume to a reference structure, cf. Section 5.3.1.

species ij	ρ_{ij} **(Å)**
Mg-Mg	0.152
Mg-O	0.187
Mg-P	0.133

B Fullfactorial Design for Design of Experiment

Table B.1: Fullfactorial design for a three factor (ρ_{comp}, T_{max}, t_{equil}), two level ($+$, $-$) system as employed in the computational sintering protocol, cf. Section 4.4.2. Table adapted from Stegmaier et al. [1] under CC BY 4.0.

Fullfactorial Design			
ρ_{comp}	T_{max}	t_{equil}	y
$+$	$+$	$+$	y_1
$-$	$+$	$+$	y_2
$+$	$-$	$+$	y_3
$-$	$-$	$+$	y_4
$+$	$+$	$-$	y_5
$-$	$+$	$-$	y_6
$+$	$-$	$-$	y_7
$-$	$-$	$-$	y_8

C TEM Simulation Parameters

Table C.1: Microscope Parameters used for TEM simulation with the Dr. Probe software [4] and determined specimen specific parameters, cf. Section 4.4.3. Table adapted from Stegmaier et al. [1] under CC BY 4.0.

Microscope Parameters	**Value**
Accelerating voltage	200 keV
Probe forming aperture	25 mrad
Semi angle of Fourier-Space detector	80 – 220 mrad
Partial temporal coherence	8.6 nm
Partial spatial coherence	0.4 mrad
Spherical aberration	1.2 mm
Specimen Parameters	**Value**
Defocus	63.3 nm
Thickness	49 nm

Table C.2: Bulk domain resolved B_{iso} values for each ion species in LATP averaged over five representative grain boundary structures, cf. Section 4.4.3. Table adapted from Stegmaier et al. [1] under CC BY 4.0.

Species	**Grain (Å^2)**	**Grain Boundary (Å^2)**
Ti^{4+}	0.00305 ± 0.00048	0.00563 ± 0.00129
Al^{3+}	0.00395 ± 0.00111	0.00764 ± 0.00252
P^{5+}	0.00363 ± 0.00073	0.00640 ± 0.00258
O^{2-}	0.00785 ± 0.00410	0.01137 ± 0.00833
Li^{+}	0.09974 ± 0.20489	0.13470 ± 0.23860

D Complexion Width for Different Size Grain Boundaries

Table D.1: Determining the complexion width of five different size grain boundary models, cf. Section 4.4.4. Listed below are total number of atoms N_{atoms}^{tot}, number of stochastically sampled atoms N_{atoms}^{stoch} in the amorphous domain, and the corresponding elemental distributions (each PO_4 unit contributes five atoms), length in z-direction of the total simulation box L_z^{tot}, the amorphous domain L_z^{amorph}, and both complexions L_z^{comp}. Table adapted from Stegmaier et al. [1] under CC BY 4.0.

Model	$\mathbf{N}_{atoms}^{tot}$	$\mathbf{N}_{atoms}^{stoch}$			L_z^{tot} (Å)	L_z^{amorph} (Å)	L_z^{comp} (Å)
L_1	14030	6124	PO_4: Ti: Al: Li:	1000 548 116 460	139.28	55.71	15.47 13.98
L_2	14625	6719	PO_4: Ti: Al: Li:	1097 601 127 506	145.09	61.01	15.67 14.70
L_3	15223	7317	PO_4: Ti: Al: Li:	1195 655 139 548	150.91	66.25	14.46 13.11
L_4	15818	7912	PO_4: Ti: Al: Li:	1292 708 150 594	157.17	72.96	15.12 14.22
L_5	16070	8507	PO_4: Ti: Al: Li:	1389 761 161 640	159.18	75.90	15.23 14.29

E Convergence for DFT Calculations[E.1]

Converged settings for the cutoff energy and the k-point grid density when performing DFT calculations on LATP using the CASTEP [5] software are found from the energy, force, and stress scoring functions with

$$\Delta E = (E^{\mathrm{DFT}}_{\mathrm{displ.}} - E^{\mathrm{DFT}}_{\mathrm{base}}), \tag{E.1}$$

$$S_{\mathrm{force}} = \frac{\sqrt{\sum_{\alpha,\beta} |F^{\mathrm{DFT}}_{\mathrm{displ.},\alpha,\beta} - F^{\mathrm{DFT}}_{\mathrm{base},\alpha,\beta}|^2}}{\sqrt{\sum_{\alpha,\beta} |F^{\mathrm{DFT}}_{\mathrm{base},\alpha,\beta}|^2}}, \tag{E.2}$$

and

$$S_{\mathrm{stress}} = \frac{\sqrt{\sum_{\alpha,\beta} |\sigma^{\mathrm{DFT}}_{\mathrm{displ.},\alpha,\beta} - \sigma^{\mathrm{DFT}}_{\mathrm{base},\alpha,\beta}|^2}}{\sqrt{\sum_{\alpha,\beta} |\sigma^{\mathrm{DFT}}_{\mathrm{base},\alpha,\beta}|^2}}. \tag{E.3}$$

The sums run over all atoms α and all property components β. These scoring functions are further reduced by the respective values from simulations with the tightest settings, i.e. largest cutoff energy or lowest k-point spacing.

Randomly displaced atomic configurations are referenced against the DFT properties of the crystalline LATP structure. A normal distribution with standard deviation of 0.1 Å is used for atomic displacements. A convergence criterion was defined by deviation of $\pm$10 meV for reduced energy and respective $\pm$10 % deviation for reduced force and stress scoring functions. The reduced scoring properties are shown in Figure E.1 (a) for the cutoff energy and Figure E.1 (b) for the k-point spacing, respectively. Values of 750 eV for the cutoff energy and 0.07 Å for the k-point spacing are found to show satisfactory convergence and employed in DFT calculations in Section 4.6.

[E.1] DFT convergence tests were conducted by S. Wengert, Theory Department, Fritz-Haber-Institut der Max-Planck-Gesellschaft.

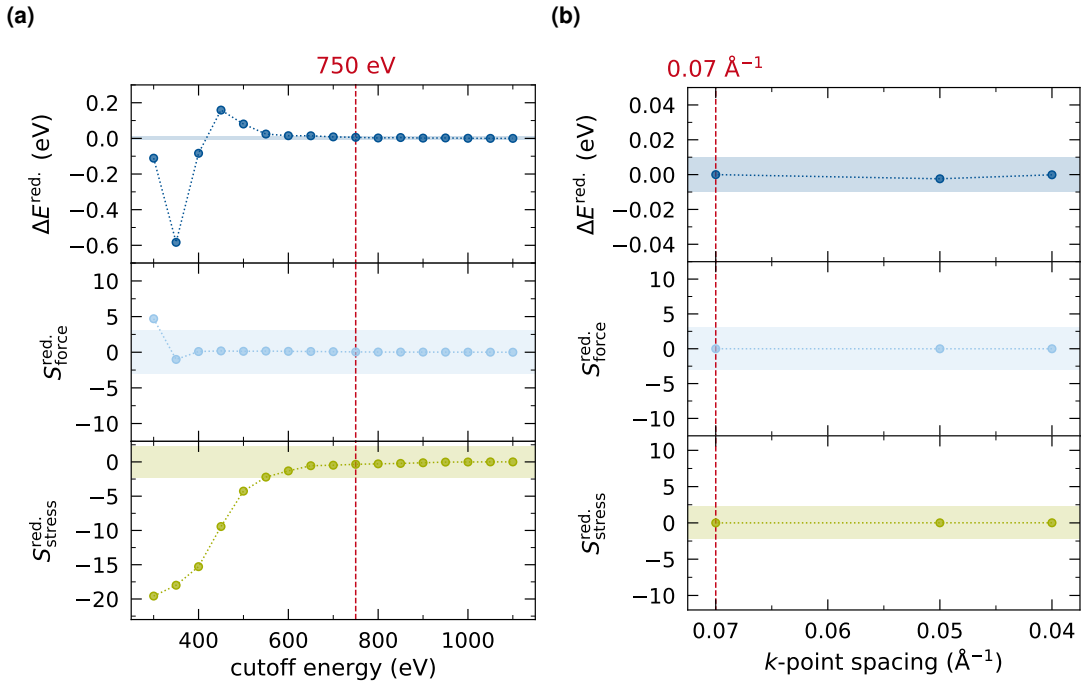

Figure E.1: Convergence testing of CASTEP DFT settings. Reduced scoring properties according to Equations (E.1) – (E.3) for **(a)** cutoff energy and **(b)** k-point spacing. Images adapted from Stegmaier et al. [1] under CC BY 4.0.

Appendix Bibliography

[1] S. Stegmaier, R. Schierholz, I. Povstugar, J. Barthel, S. P. Rittmeyer, S. Yu, S. Wengert, S. Rostami, H. Kungl, K. Reuter, R. A. Eichel, and C. Scheurer, Adv. Energy Mater. **11**, 2100707 (2021) (cit. on pp. 114, 116–118, 120).

[2] S. Kerisit, N. Aaron Deskins, K. M. Rosso, and M. Dupais, J. Phys. Chem. C **112**, 7678 (2008) (cit. on p. 114).

[3] M. Vijayakumar, S. Kerisit, K. M. Rosso, S. D. Burton, J. A. Sears, Z. Yang, G. L. Graff, J. Liu, and J. Hu, J. Power Sources **196**, 2211 (2011) (cit. on p. 114).

[4] J. Barthel, Ultramicroscopy **193**, 1 (2018) (cit. on p. 117).

[5] S. J. Clark, M. D. Segall, C. J. Pickard, P. J. Hasnip, M. I. Probert, K. Refson, and M. C. Payne, Z. Kristallogr. **220**, 567 (2005) (cit. on p. 119).